2015-8

Integration of Antennas and Solar cells for Low Power Wireless Systems

Oisin O'Conchubhair
Technological University Dublin, oisin.oconchubhair@mydit.ie

Integration of Antennas and Solar Cells for Low Power Wireless Systems

Oisin O'Conchubhair
Master of Engineering

Doctor of Philosophy

Supervisors:
Professor Max J. Ammann
Dr. Patrick McEvoy

Dublin Institute of Technology
School of Electrical & Electronic Engineering

August 2015

Abstract

This thesis reports on design methods for enhanced integration of low-profile antennas for short-range wireless communications with solar voltaic systems. The need to transform to more sustainable energy sources arises from the excessive production of harmful carbon emissions from fossil fuels. The Internet of Things and the proliferation of battery powered devices makes energy harvesting from the environment more desirable in order to reduce dependency on the power grid and running costs.

While photovoltaic powering is opportune due to immense levels of available solar power, the separate area requirements for the antenna and the photovoltaic surfaces presents an opportunity to significantly minimize the unit volume and to enable portable deployment.

The focus is on issues of integrating antennas and transmission lines above crystalline silicon solar cells, in particular, the relative orientations are complicated by a-symmetric lattice of the solar cell. A solution to minimise orientation sensitivity was provided and utilised to successfully isolate a microstrip transmission line from the solar lattice, thereby allowing four antenna configurations to be demonstrated. Further work on crystalline solar cells demonstrated their use alongside circularly polarised antennas for aerial vehicles. Wireless energy harvesting over a wide frequency range was demonstrated with an a-Si solar Vivaldi antenna. A dye-sensitised solar dipole antenna was developed for low power indoor applications.

The approaches established the engineering capacity to reduce the device size and weight through integration of the radio and the solar cell technologies. In addition, the use of different solar cell technologies demonstrated the importance of selecting the cell type most suited to the intended application.

Declaration

I certify that this thesis which I now submit for examination for the award of PhD, is entirely my own work and has not been taken from the work of others, save and to the extent that such work has been cited and acknowledged within the text of my work.

This thesis was prepared according to the regulations for postgraduate study by research of the Dublin Institute of Technology and has not been submitted in whole or in part for another award in any other third level institution.

The work reported on in this thesis conforms to the principles and requirements of the DIT's guidelines for ethics in research.

DIT has permission to keep, lend or copy this thesis in whole or in part, on condition that any such use of the material of the thesis be duly acknowledged.

Signature _____ Date _____

Oisin O'Conchubhair

Acknowledgements

I would like to thank my supervisors Professor Max Ammann and Dr Pádraig McEvoy for the opportunity to join the research group in the Antenna & High Frequency Research Centre (AHFR) and for all the advice and support they have given me over the past four years.

I would like to thank all my colleagues in the AHFR, Giuseppe, Matthias, Afshin and Abraham for their help and friendship over the years. In particular, Antoine, Vit and Domenico for being my closest sources of knowledge and for always being willing to answer my questions. Adam and Xiulong for their advice regarding circularly-polarized antennas and phase-shifting power splitter design and Kansheng for his help designing energy harvesting circuitry.

I would like to thank my parents, Eugene and Siobhan, my sister Niamh-Erin and my girlfriend Lisa for their support and encouragement throughout this journey (even though they still can't explain what I do).

Finally I would like to thank the Telecommunication Graduate Initiative which organised the financial support and provided invaluable courses to expand my knowledge of the field as I progressed through my studies.

Nomenclature

ε_r	Relative dielectric constant of a dielectric material
σ	Conductivity of a material
Ω	Electrical Resistance
V	Voltage
A	Amperage
W	Wattage
K	Kelvin
F	Farad (Capacitance)
H	Henry (Inductance)
S_{11}	Input Reflection Coefficient in the Scattering Matrix
S_{21}	Transmission Coefficient in the Scattering Matrix
Hz	Hertz
dB	Decibels
dBi	dB Isotropic

Abbreviations

RF	Radio Frequency
UWB	Ultra-Wideband
IFA	Inverted-F Antenna
PIFA	Planar Inverted-F Antenna
PV	Photovoltaic
a-Si	Amorphous Silicon
a-Si:h	Hydrogenated Amorphous Silicon
c-Si	Crystalline Silicon
DSS	Dye Sensitised Solar
ITO	Indium Tin Oxide
TiO_2	Titanium Dioxide
CP	Circularly-Polarized
V_{oc}	Open Circuit Voltage
I_{sc}	Short Circuit Current
PCB	Printed Circuit Board
MCU	Microcontroller Unit
UAV	Unmanned Aerial Vehicle
GSM	Global System for Mobile Communications
WLAN	Wireless Local Area Network
GPS	Global Positioning System
CST	Computer Simulation Technology GmbH
IEEE	Institute of Electrical and Electronics Engineers

CONTENTS

List of Figures

List of Tables

1 INTRODUCTION

Exhaustion of fossil fuels and rising concerns over harmful emissions are resulting in a shift away from carbon based fuels to more sustainable energy sources. In terms of global power generation there has been increasing investment in large scale wind, solar and hydro generation however fossil fuel consumption and production are important elements of many economies globally [1]. As a result, it will take a long time for electricity generated from fossil fuels to disappear.

Development in renewable technologies is more apparent in transportation with advancements such as the first flight around the planet by a solar powered aircraft [2]. Commercial flights using fully electric aircraft will take much more development, the first step, replacing mechanical, hydraulic and pneumatic systems with electric alternatives, is being investigated with the aim to improve efficiency [3]. There is a growing interest in unmanned aerial vehicles (UAVs), reduced maintenance costs and greater range is resulting in research into solar power UAVs [4]. Energy recovery is a common method of reducing vehicle running costs, the Komatsu PC200-8 hybrid excavator uses inertial energy recovery to charge a capacitor with energy that would otherwise be wasted [5].

On a smaller scale there is increased interest in low power wireless devices for the Internet of Things concept and on body devices. In many wireless communication applications access to a power grid may not be feasible due to remote location or the need for mobility in a product. It is therefore desirable to design devices which can harvest energy from their environment reducing load on the power grid and reducing running costs. It is shown in [6] that many sources of energy have been investigated such as ambient light, ambient airflow, thermoelectric and mechanical recovery methods. Consumer oriented products have a relatively short lifespan which means there is a greater possibility for

sustainable technology to enter this market quickly. Additionally longer battery lives would make a product more attractive in the current market which is also an incentive for development.

Our sun is a G-type main-sequence star which is capable of producing temperatures in the region of 5,300 to 6,000 K [7]. The immense temperature coupled with the huge pressure at the core results in the fusion of approximately 600 million tons of hydrogen atoms into helium atoms every second. The fusion of 4 hydrogen protons to create 1 helium proton produces 3.846×10^{26} W of power making the sun the largest source of energy in our solar system [8].

Hence the use of wireless communications powered from photovoltaic sources is attractive. The disadvantage of this concept is the greater demand for the surface area required to mount both conventional photovoltaic systems and antenna systems separately. The focus of this thesis is to integrate these systems to minimize the unit volume and to enable portable deployment.

The first section of this chapter will introduce the solar cell technologies which will be integrated with the antennas in this thesis. The second section will discuss some of the important aspects of solar antenna design. The third section will discuss works which optimised the use of solar cells alongside wireless systems. The third section will discuss previous attempts at integrating antennas with solar cells. The fourth section will discuss possible applications for solar integrated antennas. The final section will give an outline of the thesis.

1.1 Background in Solar Cell Technology

Since the creation of the first functional crystalline silicon solar cell by researchers at Bell labs in 1954 there has been much advancement in solar technology to improve

efficiency, cost or environmental resistance [9]. This section will discuss the manufacture and function of the solar cell types which are integrated with antennas in this thesis.

1.1.1 Monocrystalline and Polycrystalline Silicon Solar Cells

Crystalline silicon solar cells are the most common type of solar cell, regularly used in high power generation application such as home solar power generation. These cells are made from thin brittle semiconductor wafers which require a strong frame and protective glass to protect them from the environment.

Mono and Poly or Multicrystalline silicon solar cells originate from the same polycrystalline silicon material however the production process for polycrystalline cells is cheaper resulting in more impurities and lower efficiency. The differences in the production process are shown in Fig. 1.1.

Crystalline silicon solar cells consist of the silicon wafer sandwiched between an anode front contact and a cathode rear contact. In most cases the cathode is a solid sheet of conductive material and the anode is made up of a number of electrodes designed to maximise the level of insolation into the semiconductor material while maximising the generated power output of the solar cell.

The semiconductor material usual consists of multiple doped regions of semiconductor material which have been positively or negatively doped. When combined the electrons in these layers adjust to a state equilibrium until photons from sunlight entering the material distort the equilibrium causing the electrons to flow through the external circuit to equalise the layers once more. In this way electricity is produced by the solar cell. In the event that a photon is not absorbed by the material it will be released in the form of heat, this rise in temperature changes the properties of the semiconductor material which usually reduces the efficiency of the solar cell.

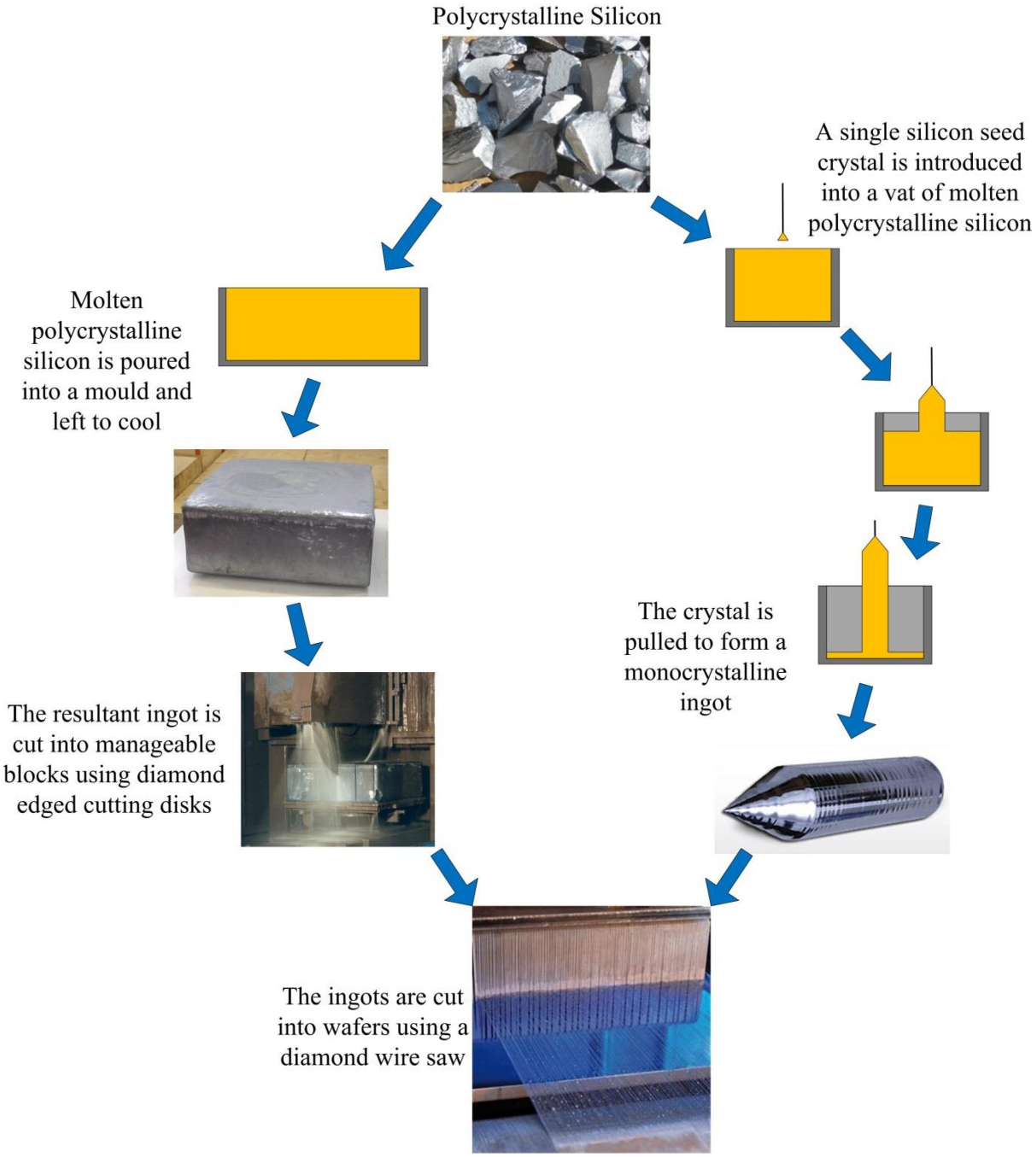

Fig. 1.1 Mono and Polycrystalline Silicon Solar Cell Production

Power outputs are usually greater than 3 W for a single c-Si cell however output voltages between 0.5 and 0.8 V require additional voltage boosting circuitry for applications requiring a small device size.

1.1.2 Amorphous Silicon Solar Cells

A-Si cells are a lower cost, flexible alternative to crystalline silicon solar cells due the layering technique used in their production, shown in Fig. 1.2.

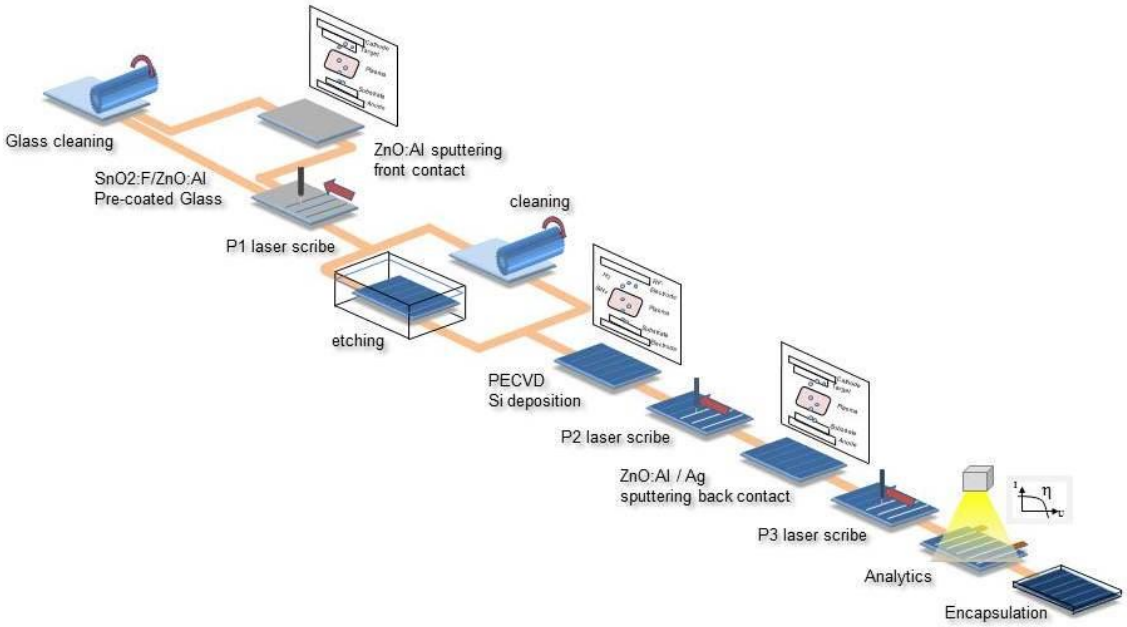

Fig. 1.2 Amorphous Silicon Solar Cell Production Process [10]

The metallic surfaces are sputtered and then laser etched to form the front electrodes and rear contacts. Vapour deposition is used to create the semiconductor layer. Impurities absorbed during deposition reduce the solar cell efficiency [11]. The lower temperatures required for deposition means that the a-Si can be layered on a wider range of substrates including glass.

It is common for thin film a-Si solar cells to be configured as solar panels and sealed in a flexible plastic encapsulant. The panels are designed to be cut along the intersection between cells to achieve the required power output and as a result can easily be trimmed to fit a desired shape.

Outputs of 3 V (~ 66 mW) or greater simplifies design of the associated circuitry but solar efficiencies are typically limited to ~10%.

1.1.3 Dye-Sensitised Solar Cells

Dye-sensitised solar cells are usually manufactured between two layers of transparent conductive substrate allowing light absorption from both sides of the cell. A carbon cathode is deposited on one substrate, a layer of TiO_2 is deposited on the opposite substrate and an

electrolyte fills the gap between the substrates to enable charge transport. In order for the TiO_2 to absorb photons it must first be sensitised to part of the solar spectrum using a dye, the colour of the dye determines the wavelength absorbed. This feature of DS-cells has given them a place in architectural design, despite having considerably lower efficiencies than c-Si, the DSSCs are more aesthetically pleasing as shown in Fig. 1.3.

Fig. 1.3 Architectural use of Dye-Sensitised Solar Cells [12]

Wider acceptance angles and better absorption capacity for diffuse sunlight and fluorescent light make DSSCs better suited to indoor use than the c-Si alternatives [13].

1.1.4 Efficiencies

Solar cells are regularly compared based on their measured efficiency calculated using a directed light source producing 1000 W/m^2, located at 90° to the solar cell. The standardised irradiance distribution used to test terrestrial solar cells simulates a 1.5 air mass spectrum to represent a yearly average for mid-latitudes. Improvements in solar cell efficiencies are shown in Fig. 1.4, triple junction cells employing multiple layers of semiconductor to absorb a wider range of the solar spectrum top the list followed by monocrystalline cells and polycrystalline cells.

Solar cell efficiency records are broken regularly, independently verified efficiency values for different solar cell types have been recorded every 6 months in *Progress in Photovoltaics* since 1993 [14]. Current efficiency values published on the 16th of June 2015 are shown in Table 1.1.

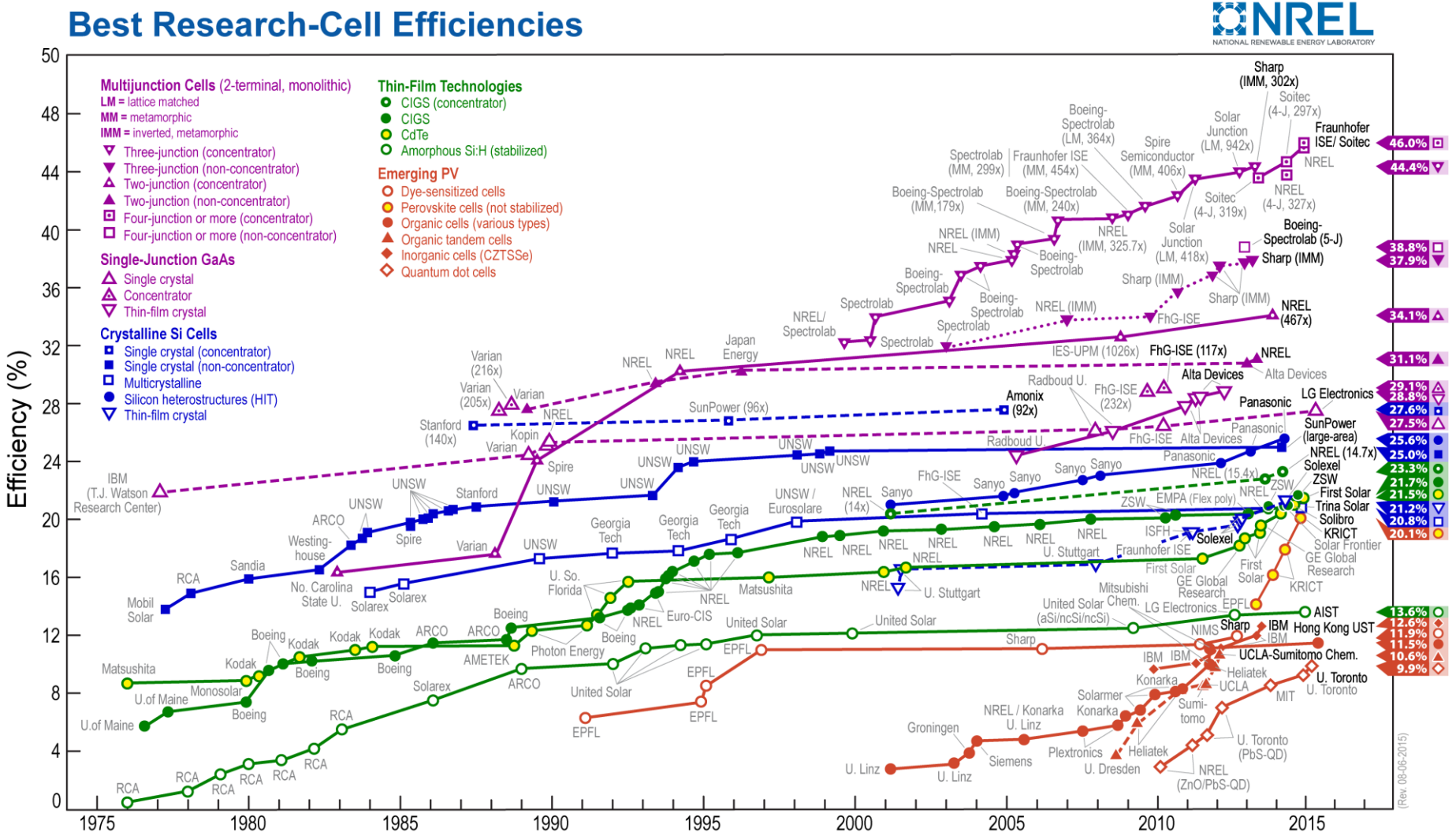

Fig. 1.4 Improvements in Solar Cell Efficiencies [15]

Table 1.1 Solar Cell Efficiency Records [14]

Solar Cell Type	Efficiency	V_{oc} (V)	I_{sc} (mA/cm^2)
Five Junction	38.8%	4.77	9.6
Monocrystalline Si	25.6%	0.74	41.8
Polycrystalline Si	20.8%	0.66	39.0
Amorphous Si	10.2%	0.90	16.4
Dye Sensitised	11.9%	0.74	22.5

It is clear that there is a sizeable efficiency gap between a-Si and c-Si solar cells however standard test conditions use a directed light source representing AM 1.5. In reality the average annual power generated by each technology covering the same surface area and oriented at the same angle could be much closer due to the lower sensitivity to spectrum and temperature change of a-Si cells [16].

1.2 Antenna Fundamentals

The antenna structures used in this thesis were either chosen to minimise solar shadowing while improving performance compared to previous antenna integrations from the literature or to form a simple platform to analyse the use of novel solar cell material. The antennas and feed networks were designed to be printed on copper clad substrate using an LPKF ProtoMat C60 CNC milling machine. Nonplanar structures must be soldered together by hand which can lead to slight variation from the simulation model.

1.2.1 Impedance Matching

In order to maximise power transfer to a load, in this case the antenna, it is important to ensure that the load impedance Z_i matches the source impedance Z_o. All antennas in this thesis are designed to have a characteristic impedance of 50 Ω to match the Rhode & Schwarz Vector Network Analysers used in the AHFR.

Energy will be reflected when the load impedance doesn't match the source impedance. The reflection coefficient Γ is equal to the S_{11} parameter which describes the ratio between the power received at port 1 and power sent from port 1.

$$\Gamma = S_{11} = \frac{Z_i - Z_o}{Z_i + Z_o}$$

When a perfect match is achieved, no power is reflected and the S_{11} = 0. The S_{11} is usually represented in decibels on a 2D plotted against frequency. Antenna bandwidth is usually taken as the frequency range over which the S_{11} is lower than -10 dB i.e. more than 90% of the power is transferred to the load. It is important that solar antennas are tuned so that their bandwidth covers to the desired frequencies of operation to ensure efficient use of stored energy.

1.2.2 Importance of Wide Beamwidths

The electromagnetic field generated by an antenna is graphically represented in the antennas radiation pattern [17]. In this thesis the radiation pattern is expressed in term of gain relative to an isotropic antenna. The half-power beamwidth describes the angle between two points in plane cut through the radiation pattern main lobe which are 3 dB below the peak gain.

Achieving a wide beamwidth is an important design goal for solar antennas because placement of a solar powered wireless device is restricted to angles which enable efficient solar generation. The cells need to face due south for locations in the northern hemisphere and vice versa for optimum generation, wide beamwidths enable wider RF coverage as shown in Fig. 1.5.

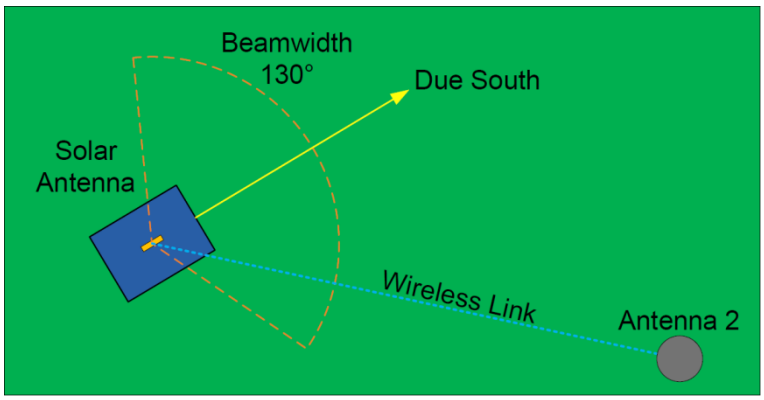

Fig. 1.5 Solar Antenna Orientation

The tilt angle is dependent on latitude, a rule of thumb for fixed solar tilt angles is to set the tilt angle to the latitude plus 15°. A panel in Dublin should be set to a tilt angle of 68°, wide beamwidths again improve RF coverage as shown in Fig. 1.6.

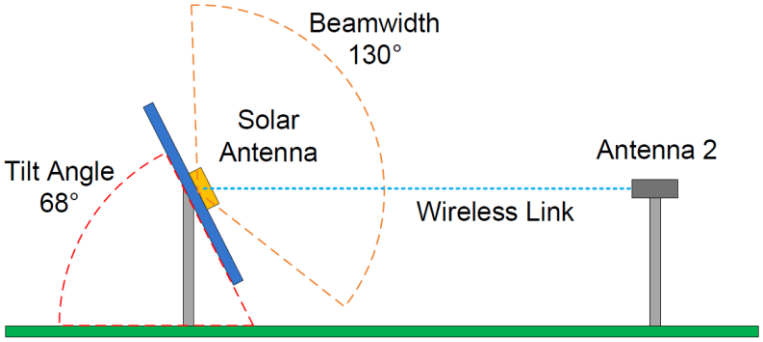

Fig. 1.6 Solar Antenna Tilt Angle

1.3 Wireless Devices and Solar Cells

Wireless sensors where the solar cells are separate from the wireless system have been widely used to date and much work has been carried out on optimising power generation and intelligently using stored energy. In [18] a photovoltaic power supply is developed to power a separate wireless light intensity sensor node. A power management system was developed to track the maximum power point of a small solar panel ensuring smooth charging of a super capacitor during varying light intensity conditions.

Fast charging super capacitors are an essential component in small scale solar power generation in order to fully utilise the high currents produce by mono and polycrystalline silicon solar cells. While voltage boosting and battery charging circuitry has limited current handling capabilities, a super capacitor can quickly store as much power as possible during short periods of insolation.

In [19] a system is developed to choose the most efficient route to transmit data between two nodes in a network. The system tracks the stored energy of each node which will vary depending on light intensity at each node location. It uses this data to select a route

through the nodes which have the most power ensuring that the entire system is active for longer.

Most wireless systems currently rely on batteries for storage however these have substantial drawback in terms of charging losses, low charge/discharge cycle life, potential for overheat failure and substantial maintenance costs [20]. Intelligent power management coupled with reductions in MCU power requirements and super capacitor costs could remove the need for batteries in low power applications in the future.

1.4 Previous Approaches to Solar Integrated Antennas

Many attempts have been made to couple antennas and solar cells, integrations of antennas with solar cells usually take one of five forms,

1. The solar cell is simply positioned above a radiating element or ground plane with adequate space around the antenna to allow the antenna to radiate leaving unutilised surface space.
2. The solar cell provides ancillary support to a metallic antenna, for example used as a parabolic reflector.
3. The solar cell is used as the radiating element of an antenna and a metallic ground plane is provided to achieve radiation.
4. The solar cell is used as an RF ground for a metallic antenna.
5. Fully solar integrated antenna whereby the solar cell forms the radiating element and does not require additional metallisation to achieve radiation.

1.4.1 Co-Siting of Antennas and Solar Cells

The simplest form of solar integration co-locates the antenna and solar cell in an effort to minimise space i.e. the antenna is fully metallic with solar cells arranged in its vicinity. This minimises interaction by ensuring the two systems are functionally separate however

additional real estate is required as well as the additional cost of metallisation for the antenna and ground plane.

The co-siting of a 920 MHz coplanar waveguide inverted-F antenna (IFA) with a-Si solar cells [21] demonstrated the isolation of the antenna and solar functions to avoid mutual interference. The antenna occupied 25% of the available solar footprint.

Circularly-polarized antennas have been used alongside solar cells in space applications [22]. In this case circularly-polarized microstrip patch antennas operating at 2.4 GHz were positioned in different locations on a mini spacecraft to determine the best configuration to ensure ground communication is maintained. These designs require separate surface areas for antennas and solar cells meaning that the satellite needs to be large.

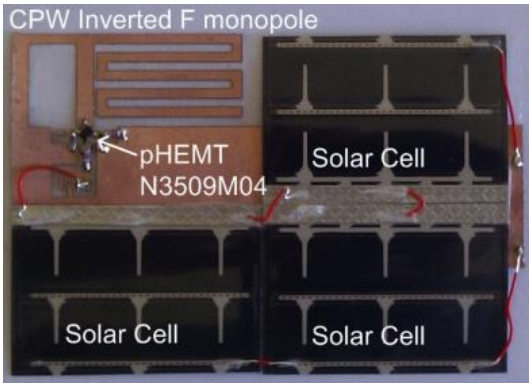

Fig. 1.7 CPW IFA with a-Si Panel [21]


Fig. 1.8 CP Patch Antenna [22]

To avoid additional footprint extensions, it becomes preferable to vertically integrate the antenna while minimizing any solar shadowing. A panel of cells was configured above a metallic slot antenna [23] which radiated through apertures that reduced the solar area by 6.5% however this antenna had a 25 mm height. Similarly a solar cell was located above an 11.5 mm high quad slot antenna achieving omnidirectional coverage with adequate spacing provided to allow radiation [24].

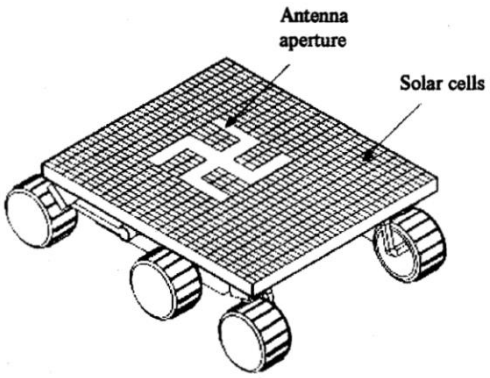

Fig. 1.9 Slot Antenna for Space Applications [23]

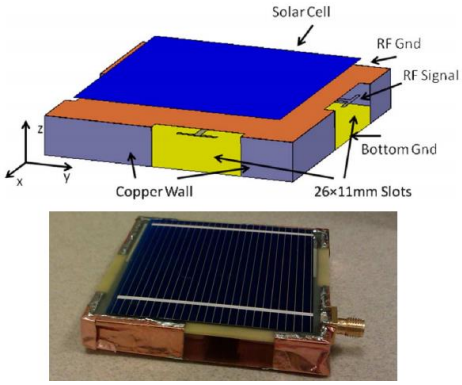

Fig. 1.10 Quad Slot Antenna [24]

1.4.2 Solar Cells Providing Ancillary Support to Antennas

Similar to co-locating the antenna and solar cell, providing ancillary support again minimises the interaction between the systems by functionally isolating the systems. In this configuration the antenna is metallic and would function without the solar cells, the cells are instead used to complement the antenna function e.g. a solar cell reflector focusing an antenna beam.

A polycrystalline silicon solar cell has provided a ground plane for a microstrip transmission line and acted as a reflector for a copper dipole antenna [25]. It was found that the solar cell produced the same radiation pattern as a perfect electric conductor with only 0.24 dBi gain decrease.

A simulated parabolic reflector laminated with an unspecified solar cell type focused the beam of a 12 GHz horn antenna with only a 2.8 dB decrease in gain compared to a conventional reflector [26]. The antenna achieved a gain of 31.7 dB but a narrow 3° beamwidth would make it difficult to achieve an RF link while optimising for solar generation.

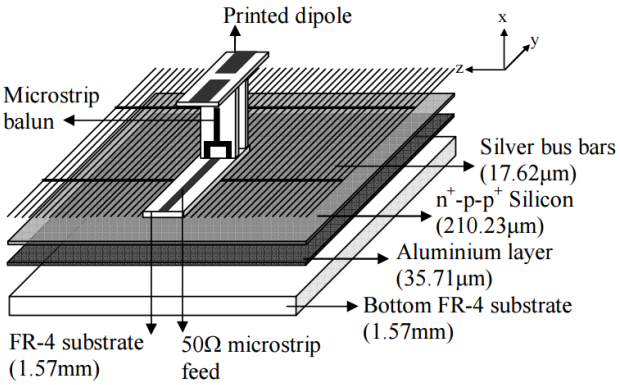

Fig. 1.11 c-Si Reflector [25]

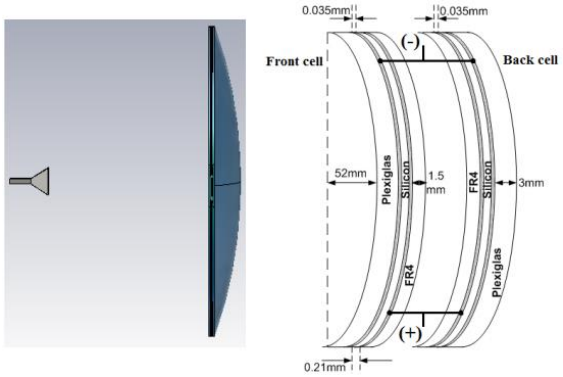

Fig. 1.12 a-Si Parabolic Reflector [26]

Two linearly-polarized meshed patch antennas, with a 90º phase difference, sharing a single microstrip feed line used a solar panel as a substrate between the antenna and the conductive shielding of the satellite acting as a ground plane [27]. The patch antennas achieve circular-polarization with 5.15 dBi of gain at 2.47 GHz and a 70% mesh transparency.

A solution with an 8 mm device height used a polycrystalline solar cell as a parasitic element above a PIFA [28] to achieve resonance in four bands with gain values from 2 – 4 dBi. This ensured irradiation of the entire surface of the solar cell but requires considerable space for the metallic antenna and ground plane.

Fig. 1.13 Meshed Patch Antennas [27]

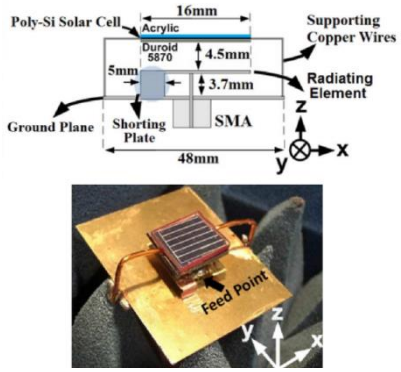

Fig. 1.14 Solar Parasitic Element [28]

1.4.3 Solar Cells Functioning as Radiating Elements

In this method the solar cell forms the radiating element of the antenna reducing the overall device weight and removing the antenna metallisation cost. However a metallic ground plane is still required to achieve radiation.

A GPS antenna envisaged for vehicular applications utilised four cells in a monocrystalline solar panel excited by an aperture coupled feed to achieve resonance without interfering with its DC operation [29]. This approach overcomes solar loss due to apertures and shadowing however the device had a total integrated height of 12 mm and required a large metallic ground plane.

In [30], a Hydrogenated Amorphous Silicon (a-Si:H) solar cell constituted an ultra-wideband monopole antenna with a bevelled copper feed for use as a wireless sensor. Simulated results showed the 2 - 10 GHz antenna had 0 - 3 dBi gain. The average power consumption by the sensor was 29 μW, which could be supported for more than 48 hours using a 500 mF storage capacitor. The sensor circuitry and feed network are designed into the RF ground minimising unnecessary metallisation.

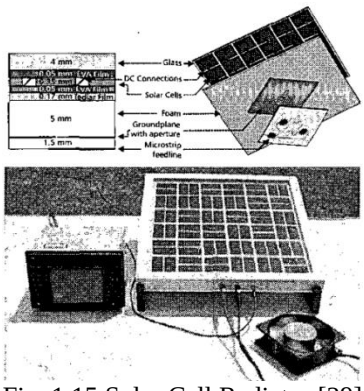

Fig. 1.15 Solar Cell Radiator [29]

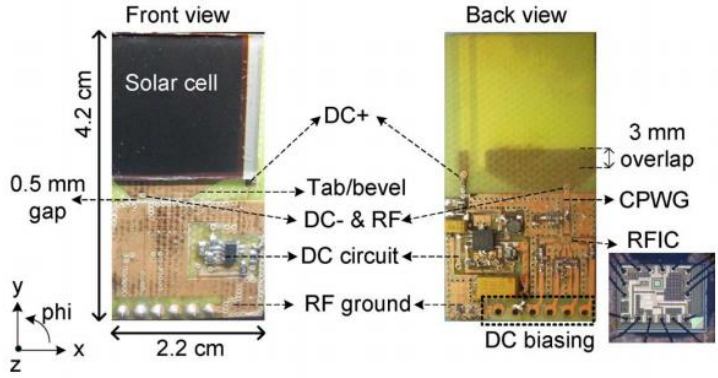

Fig. 1.16 a-Si Monopole Antenna [30]

1.4.4 Solar Cells Functioning as a Ground Plane

Further reduction in manufacturing costs can be achieved by using the solar cell as a ground plane and integrating a metallic radiating element at much lower expense. However antenna shadowing on the solar cell will negatively impact solar power output and the solar cell structure can make impedance matching difficult.

A solution with a 2 mm integrated height used a patch antenna over a polycrystalline cell [31]. Interaction with the solar lattice resulted in weaker electric fields when the transmission line was oriented in parallel to the electrodes which demonstrates the antennas

dependence on solar cell properties. The antenna area shadow is a significant 13% of the solar cell area.

In [32] solar cells were connected to an aluminium plate using conductive epoxy to form the ground plane for a meshed patch antenna on transparent substrate. It was found that impedance matching the antenna with the feed traversing the solar cell connected the ground plane was difficult resulting in a poor radiator.

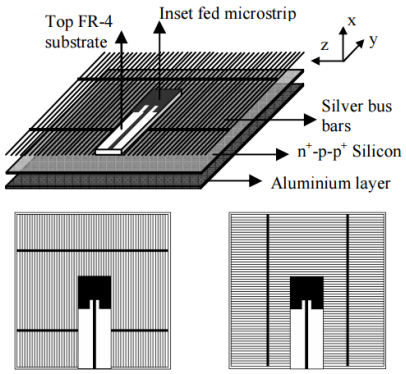

Fig. 1.17 Solar Patch Antenna [31]

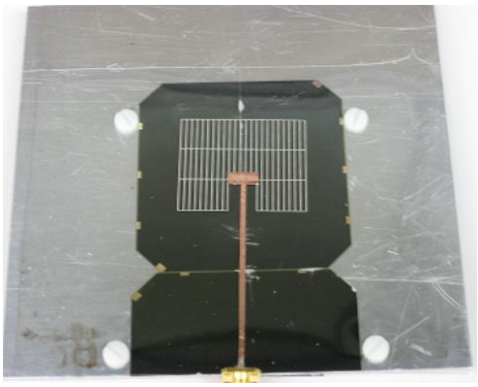
Fig. 1.18 Meshed Patch Antenna [32]

1.4.5 Fully Solar Integrated Antenna

An idealised case would be to manufacture the antenna and solar cell as one compact light weight system, considerably reducing production costs. This is easier to achieve with less efficient solar cell types which are cheaper to manipulate into a desirable shape for radiation. There is a trade-off with the removal of photosensitive material to achieve radiation however weight and cost reductions make this the most desirable solution.

A solar concentrator was used as a parabolic reflector to enhance the antenna gain and the solar power output by focusing the light on four in-series emitter-wrap-through (EWT) solar cells to create a 1.5 GHz dipole antenna [33]. While the 2.2 V (73.8 mW) could support a low powered sensor, the design is comparatively large for its output power.

In [34] a pair of hydrogenated a-Si solar cells are fed with copper bevels to create an ultra-wideband dipole antenna. This antenna operates from 3 – 10 GHz with a peak gain of

3 dBi. This sensor consumed an average of 55 μW and could last for 95 minutes on a 70 mF storage capacitor. Replacing the copper bevel with a solar cell alternative would better utilise the real estate available but may impact the antenna performance.

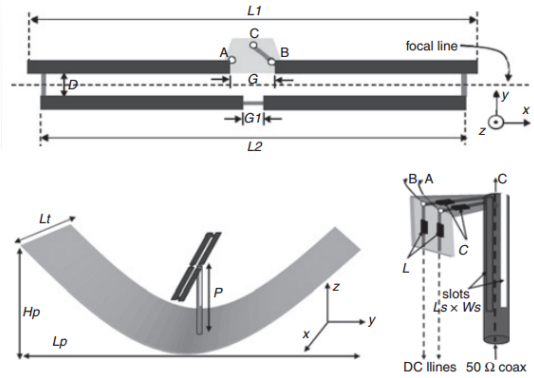

Fig. 1.19 EWT Dipole Antenna [33]

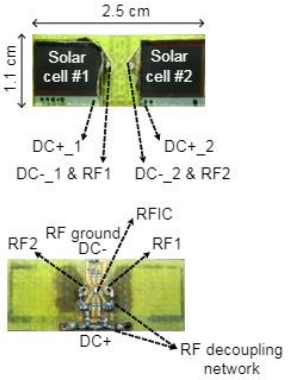

Fig. 1.20 a-Si Dipole Antenna [34]

An enhanced integration was proposed [35] where a-Si cells were configured with an aperture coupled feed to excite a 2.4 / 5.2 GHz slot antenna. However, the antenna footprint is circa 10% of the available footprint reducing the solar collecting area.

In [36] a dipole and a loop antenna covering 3.1 – 10.6 GHz for UWB systems are discussed. Both antennas use amorphous silicon solar cells as the radiating elements. The dipole antenna was capable of producing 0.04 W under a 1000 W/m^2 light source. The loop antenna was capable of producing 0.075 W however in order to function effectively it would require a uniform light source surrounding the antenna. As neither antenna design requires a ground plane, both of these designs maximise use of real estate thus greatly reducing the required size of a wireless sensor.

Four 6% efficient a-Si solar cells were deposited on a stainless steel plate containing a slot antenna achieving 3.4 dBi gain at 4.34 GHz [37]. This work found that the addition of the solar cell on the stainless steel plate reduced efficiency slightly but achieved acceptable radiation performance.

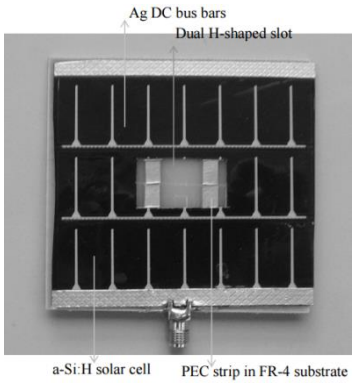

Fig. 1.21 Dual Band a-Si Slot [35]

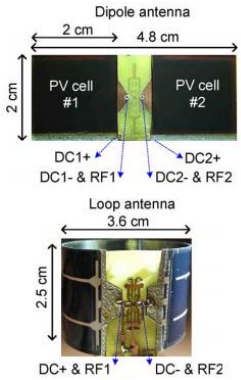

Fig. 1.22 a-Si Dipole and Loop [36]

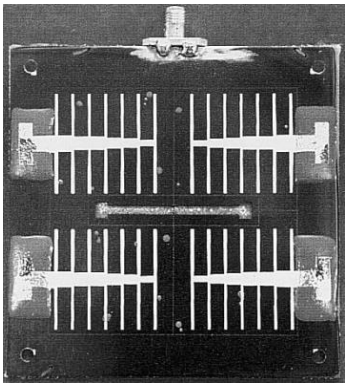

Fig. 1.23 Custom a-Si Slot [37]

1.4.6 Conclusions from Previous Approaches

It is clear from the research that co-locating the antenna results in an excessively large device area to accommodate both systems and involves unnecessary metallisation therefore this integration method should be avoided.

While using solar cells or panels in a supportive role is a successful form of antenna integration, it has limited potential applications as the focused radiation patterns leave little adjustability for solar optimisation.

Utilising a solar cell as the radiating element of an antenna can minimise interaction with the solar cell structure and material properties however the requirement for a metallic ground plane make this method less desirable.

A metallic antenna above a solar cell ground plane is a cost effective method of integration as the antenna element usually presents the least metallisation requirements while the solar cell already has a homogeneous metallic area to act as a ground plane. Further miniaturising of the antenna is required to reduce solar shadowing and improve power production.

Fully solar integrated antennas are the ideal solution requiring only one production cycle to manufacture both the antenna and power source of the device. Further work is

required to maximise use of device real estate by minimising slot apertures and utilising different solar cell types for different applications.

1.5 Applications which can benefit from Solar Antenna Integration

The range of potential applications for solar integrated antennas range from large satellites to small scale wireless sensor nodes and each application has its own unique requirements depending on its environment.

Satellites are becoming smaller meaning that there is increased competition for real estate. Cube satellites, such as the ArduSat which is $100 \times 100 \times 100$ mm square, are an application where surface area is in high demand. To combat these space restrictions the ArduSat uses 30% efficient triple junction solar cells and a turnstile antenna where four monopoles fold out from the chassis after deployment [38]. The four monopoles are fed with a 90º phase shift between each antenna to give circular-polarization in two directions. The monopoles operate at 400 - 480 MHz and achieve a gain of around 1.5 dBi. The use of a solar integrated antenna in this application would maximise real estate use thus increasing solar cell area and reduce the complexity, cost and weight of the satellite.

Weather balloons carry a device called a radiosonde which is used to measure atmospheric parameters such as temperature, humidity and altitude. Measured data is transmitted to fixed receivers on the ground at frequencies of 403 MHz or 1680 MHz. These devices generally use water activated batteries which are expensive, have a short life span and have a low power output. An integrated solar antenna coupled with a rechargeable battery could extend the life of the radiosonde and reduce maintenance costs after recovery. The colder air at high altitudes would suit c-Si solar cells which are more efficient when cooled.

Unmanned aerial vehicles are envisaged for cost effective delivery of goods in the future [39]. Similarly UAVs fitted may be used for meteorological research in areas which lack adequate infrastructure or are too dangerous for manned flight [40]. In these cases electric UAVs could potentially have to travel extensive distances, potentially encountering adverse weather conditions resulting in rapid exhaustion of stored energy. Implementing light weight solar antennas would increase potential flight times and reduce the likelihood of power loss during flight. Polycrystalline silicon solar could provide the high power required by an electric vehicle without incurring excessive cost.

Work has been carried out to investigate the feasibility of wireless sensor nodes powered from solar cells. In [30] a solar cell powered wireless sensor node using a 20 mW 2 cm^2 amorphous silicon solar cell is used as a monopole antenna. A combination of low power components and a super capacitor for storage mean this device can operate at a minimum of 2 mW when not in sleep mode. Solar integrated sensors are envisaged for on-body biomedical applications [41]. Both flexible a-Si and DSS cells configured to include a radiating element have a potential to provide a cost effect wireless solution.

1.6 Thesis Outline and Novelty

An analysis of the impact of the solar lattice present on most crystalline silicon solar cells is carried out in Chapter 2 with a focus on transmission lines and antennas separately. This work isolates the effects of the photovoltaic material from the results using an FR-4 substitute to better understand the effects of the lattice alone.

Chapter 3 investigates the implementation of a grounding strip beneath a microstrip transmission line to improve impedance matching compared to previous solar antennas from the literature. The performance of three different low profile inverted-F antenna configurations above a 3.5 W multicrystalline silicon solar cell is analysed. Centrally located

antennas are studied with the aim to reduce solar shadowing and achieve greater orientation independence compared to previous antennas integrated above solar cells. Offset and dual antenna array configurations are evaluated with the aim to improve solar exposure or implement beam switching to cover a larger area.

Four inverted-F antennas located along the intersections between four multicrystalline silicon solar cells will be used to study circular-polarization on solar antenna array in Chapter 4. The antenna location enables greater solar cell exposure than previous circularly-polarised antennas in the literature. Polarization reconfigurability is envisaged to allow communication between aerial nodes.

A slot is removed from an amorphous silicon solar cell to create the first ultra-wideband solar Vivaldi antenna in Chapter 5 with the aim to investigate if sufficient metallisation is provided to achieve resonance.

Dye-sensitised solar cells are utilised for the first time in Chapter 6 to create a dipole antenna suitable for indoor and low light applications. All solar cell layers are considered to determine their effect on the antenna performance. Indium tin oxide coatings on the solar cells glass outer layer are examined to ensure sufficient conductivity is available to achieve resonance.

2 INTERACTION WITH THE SOLAR LATTICE

The ground plane is an important structure in any antenna design. In an idealized case the ground would be a perfect electric conductor greater than a quarter wavelength in length which would result in optimum radiation performance. Imperfections in the ground plane can result in reduced gain, irregular radiation patterns or undesired resonances.

There are scenarios where an imperfect ground plane is desirable, for example [42] used a meshed ground plane to reduce the radar cross section of an antenna. In this case, the well-designed ground plane reduced the radar cross section by 15 dB at certain frequencies with minimal compromise on antenna performance, 0.5 dB reduction in gain and 0.9% reduction in bandwidth compared to the solid ground. However, in general transmission lines above an imperfect ground plane are susceptible to interference. In [43] work was carried out to investigate the signal quality of a microstrip transmission line above various imperfect ground planes. Maintaining a solid ground plane beneath the microstrip line was found to be crucial for signal quality, discontinuities such as slots in the ground plane resulted in significant signal reflection.

Solar cells are complex structures consisting of a photosensitive material sandwiched between two conductive layers making them imperfect inhomogeneous ground planes. Conductive layers vary greatly between cell types, they can be a homogenous transparent conductor or a lattice of thin silver electrodes intersected by a number of thick bus bars. This configuration allows maximum insolation of the photosensitive material while ensuring enough conductor is present to carry the high currents produced by the solar cell. Typically, antennas radiate using homogenous conductive ground planes. Many crystalline silicon solar cells have a homogenous rear contact which can form the basis of a ground plane where the superstrates are partially conductive. Positioning the antenna above the solar cell as a ground plane has a number of benefits.

- The radio module and other electronics would most likely be located beneath the solar cell to avoid shading the solar cell therefore positioning the antenna behind the cell would cause undesirable interaction with these components.
- The device can be mounted to a concrete or metallic structure with the solar cell facing outward towards the sun meaning that positioning the antenna on the rear of the cell would incur considerable losses.
- Positioning the antenna centrally above the solar cell minimises ground plane effects ensuring a symmetric radiation pattern is achieved.

In this chapter a metallic lattice printed on FR-4 substrate, shown in Fig. 2.1, is used to quantify the interaction with a periodic lattice without a silicon sub-layer. The use of FR-4 substrate in this imitation cell removes any effects caused by electrical conductivity variation in the photosensitive material of a solar cell due to varying light intensities between measurements. It also allows an FR-4 substrate with no lattice to be used for comparison.

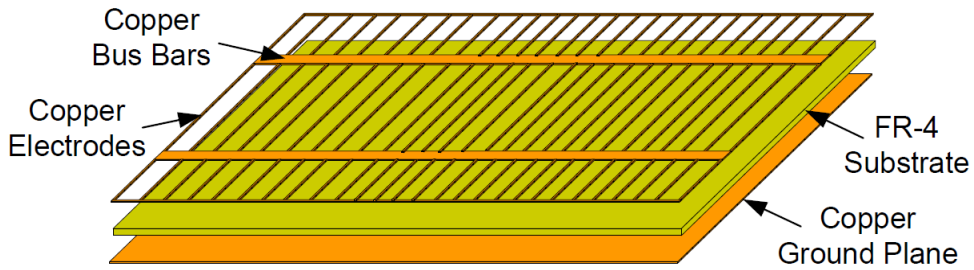

Fig. 2.1 Exploded view of FR-4 Solar Cell Substitute

The lattice structure used is similar to those found on crystalline silicon solar cells. It was printed in copper on one side of a 0.4 mm thick FR-4 substrate with a uniform copper layer on the opposite side. Crystalline silicon cells are commonly manufactured in 6 × 6″ cells (152.4 × 152.4 mm) however due to manufacturing limitations the FR-4 substitute was manufactured to 133 × 133 mm. The lattice consisted of 49 × 0.1 mm wide copper traces intersected by 2 × 2 mm traces spaced 74.18 mm apart. Although the dielectric constant for

FR-4 at $\varepsilon_r = 4.3$ is lower than the $\varepsilon_r = 20$ for silicon, this approach enables an initial analysis of the effects of the conducting lattice.

The effect of changing the lattice orientation on both an IFA and the transmission line will be investigated in this chapter. The orientation of the models discussed is in relation to the lattice of electrodes for example Fig. 2.2 (a) shows the antenna parallel to the lattice and the transmission line perpendicular to the lattice. Fig. 2.2 (b) shows the antenna perpendicular to the lattice and the transmission line parallel to the lattice.

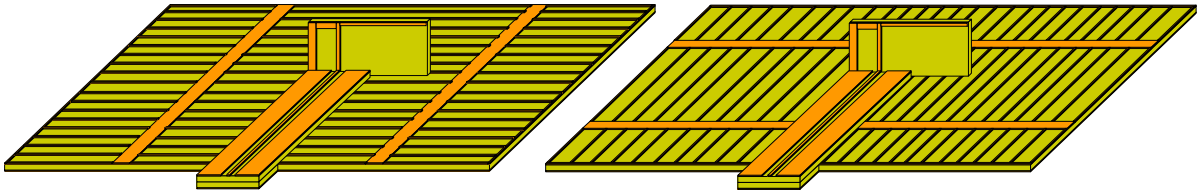

(a) Parallel (b) Perpendicular

Fig. 2.2 Antenna Orientations

2.1 Transmission Lines and the Solar Lattice

A grounded coplanar waveguide (CPW) traversing the lattice was used to assess the interaction between a transmission line and the lattice. A grounded CPW was chosen as microstrip line sensitivity to lattice orientation has previously been demonstrated in [31]. The additional grounding of the CPW was expected to achieve greater isolation however a connection to the solar cell was required for improved antenna grounding. The structure is shown in Fig. 2.3 was printed on 0.4 mm thick FR-4 substrate with the strip width $w_s = 0.715$ mm, the gap $g = 0$.

The CPW transmission line was designed without the lattice and then tested in four configurations (a) with no lattice or airgap, (b) with no lattice and with an airgap, (c) parallel to lattice and (d) perpendicular to the lattice.8 mm and the ground width $w_g = 4.94$ mm.

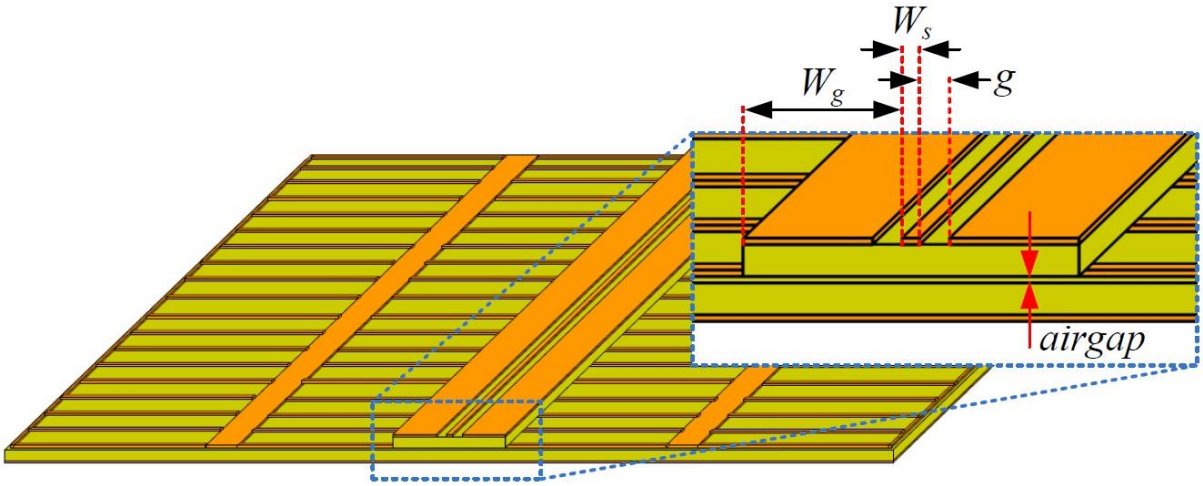

Fig. 2.3 Coplanar Waveguide Dimensions

The transmission line and its substrate from configuration (a) were raised by the height of the lattice thickness (0.035 mm) to create the configuration (b) leaving an air gap between the substrates. This gap reduces capacitance in the system as capacitance between two plates is inversely related to the distance between the two plates. This can be simulated by adding a negative capacitance in parallel to the transmission line of configuration (a) as shown in Fig. 2.4.

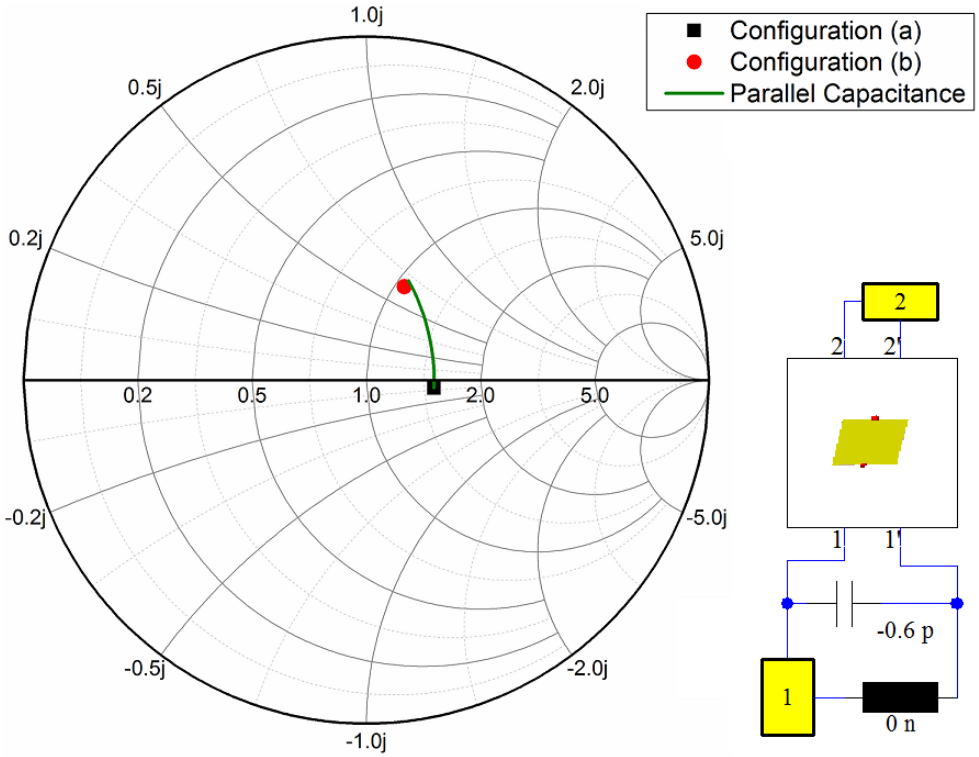

Fig. 2.4 Impedance Variation between Configurations (a) and (b)

Configuration (c) introduced the metallic lattice in the parallel orientation this increases the capacitance from configuration (b) as the lattice introduces differing capacitance areas along the transmission line length. Where the transmission line crosses the bus bar, Fig. 2.5 (a), the bus bar provides a route for current to flow along a greater area. Away from the bus bar there are stronger electric field between the transmission line and the ground plane but there is also interaction with the single electrode running beneath the transmission line, Fig. 2.5 (b).

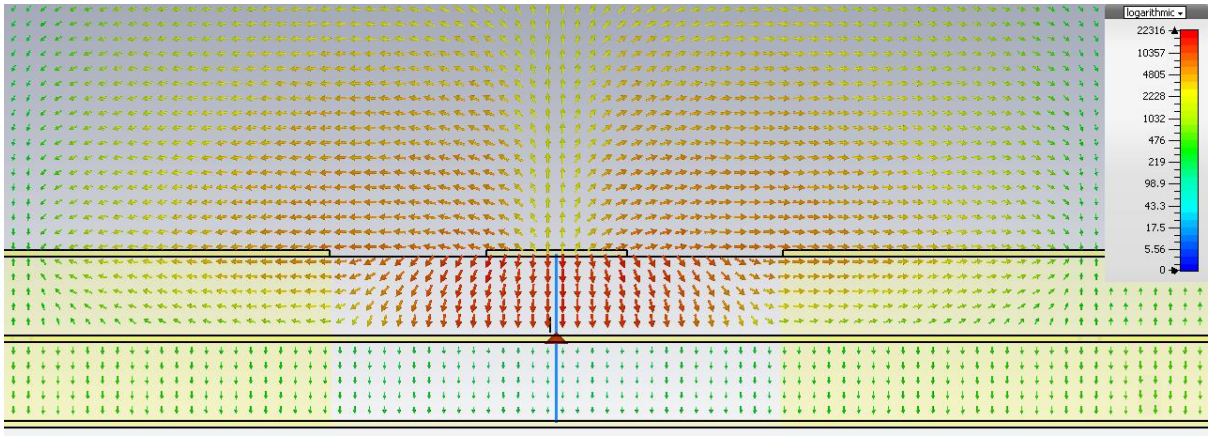

(a) Current Density Cut Through Bus Bar

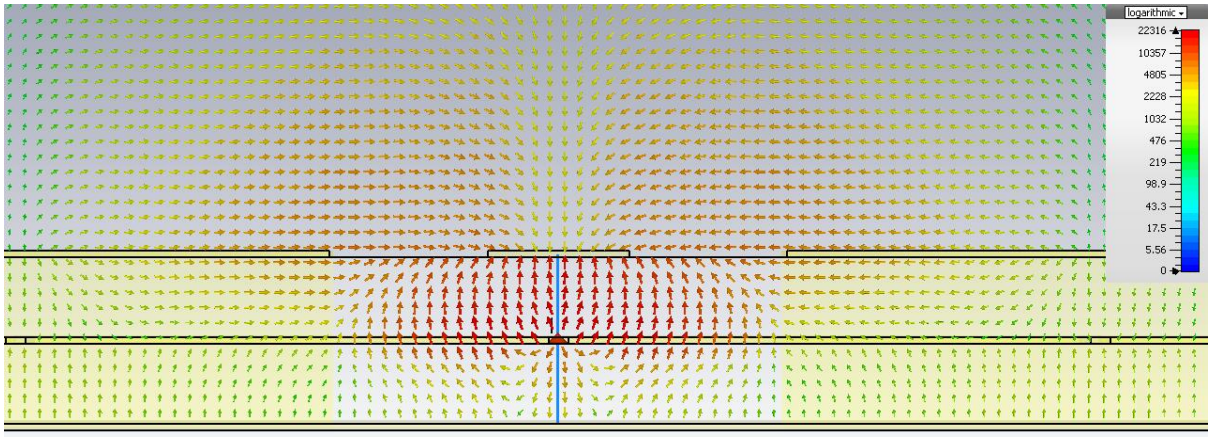

(b) Current Density Cut Through Cell Centre

Fig. 2.5 Parallel Current Density Plots

The increased current density between the transmission line and the bus bar shown in Fig. 2.5 (a) appears to be evenly distributed along the length of the bus bar which introduces a series inductance. The additional capacitance and inductance can be simulated in CST microwave studio, shown in Fig. 2.6.

Configuration (d) utilised the lattice in the perpendicular orientation which increased the parallel capacitance considerably as the transmission line covered a greater area of the lattice. In addition the orientation of the lattice allows currents to flow further on the lattice introducing an inductive element into the system, shown in Fig. 2.7.

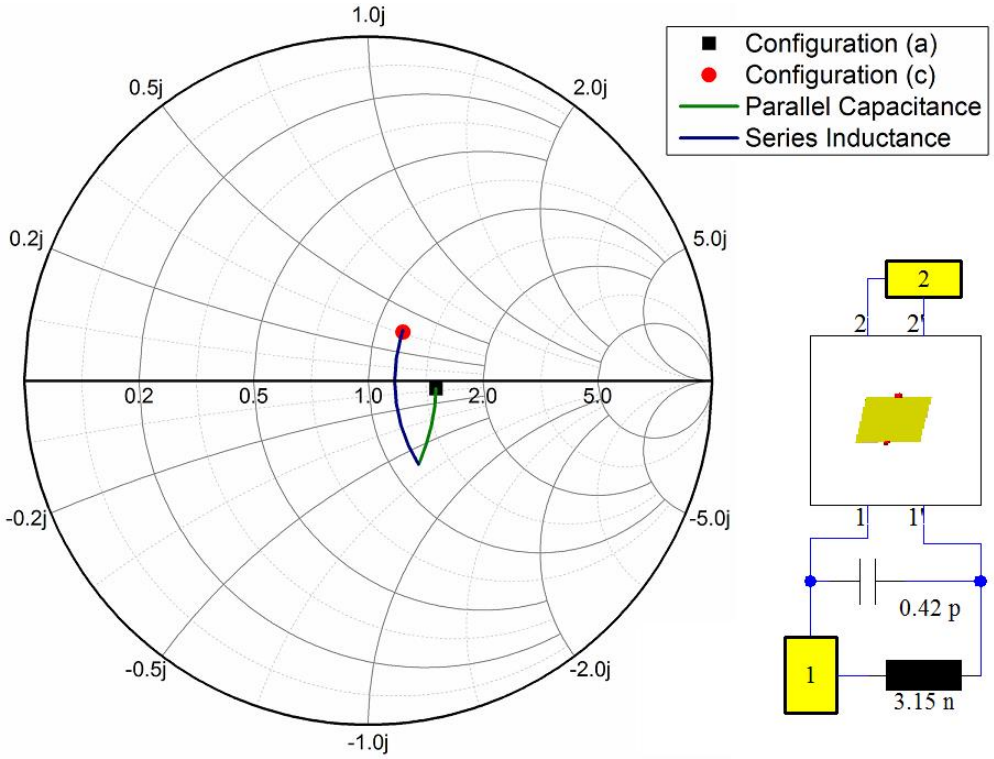

Fig. 2.6 Impedance Variation between Configurations (a) and (c)

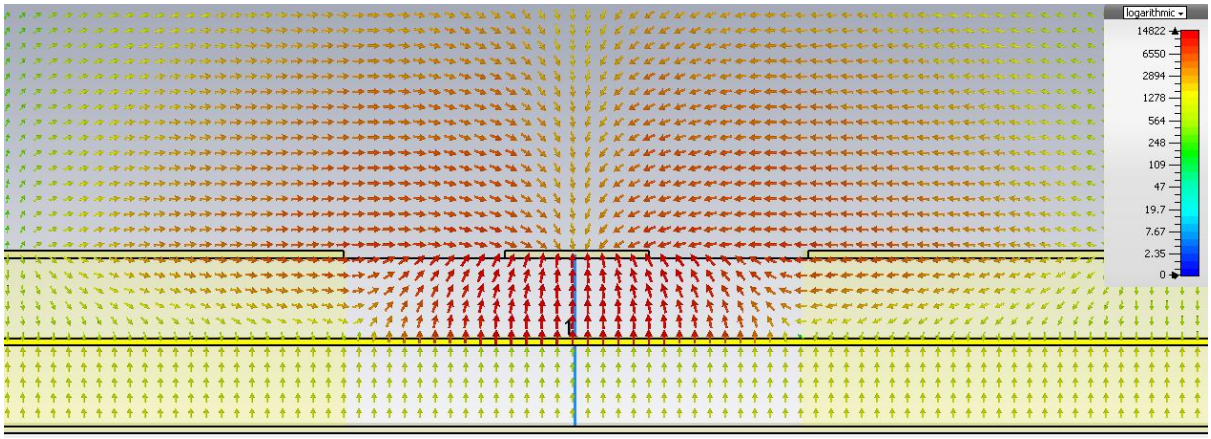

(a) Current Density Cut Through Lattice Bar

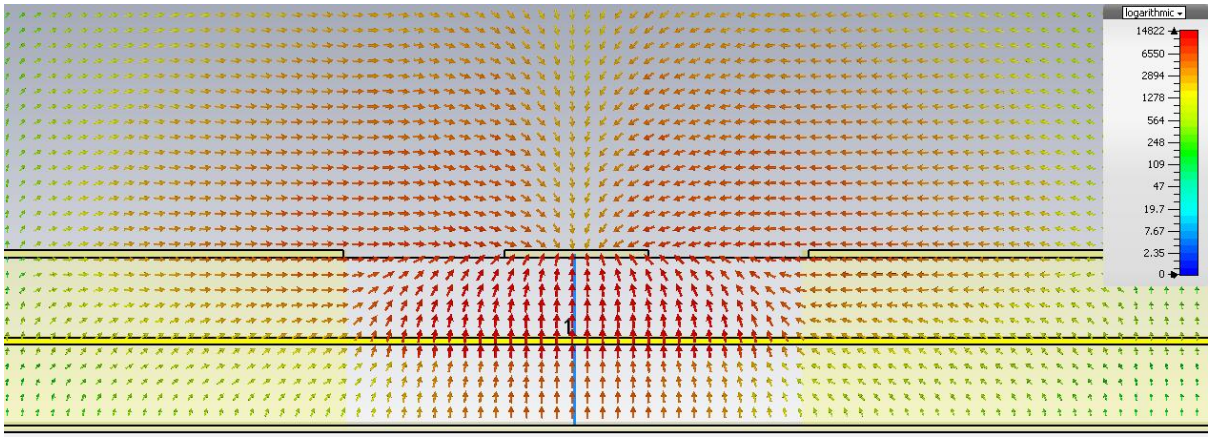

(b) Current Density Cut Between Lattice Bars

Fig. 2.7 Perpendicular Current Density Plots

In the area where the lattice is not between the transmission line and the ground plane the capacitance has the same properties as configuration (b) except the area is now reduced. Where the lattice is located between the transmission line and ground plane there is effectively two small capacitors, one between the transmission line and lattice and one between the lattice and ground. All these capacitors combine to yield an equivalent capacitance which is greater than configuration (b). These properties can be simulated by increasing the parallel capacitance and including a series inductance as shown in Fig. 2.8.

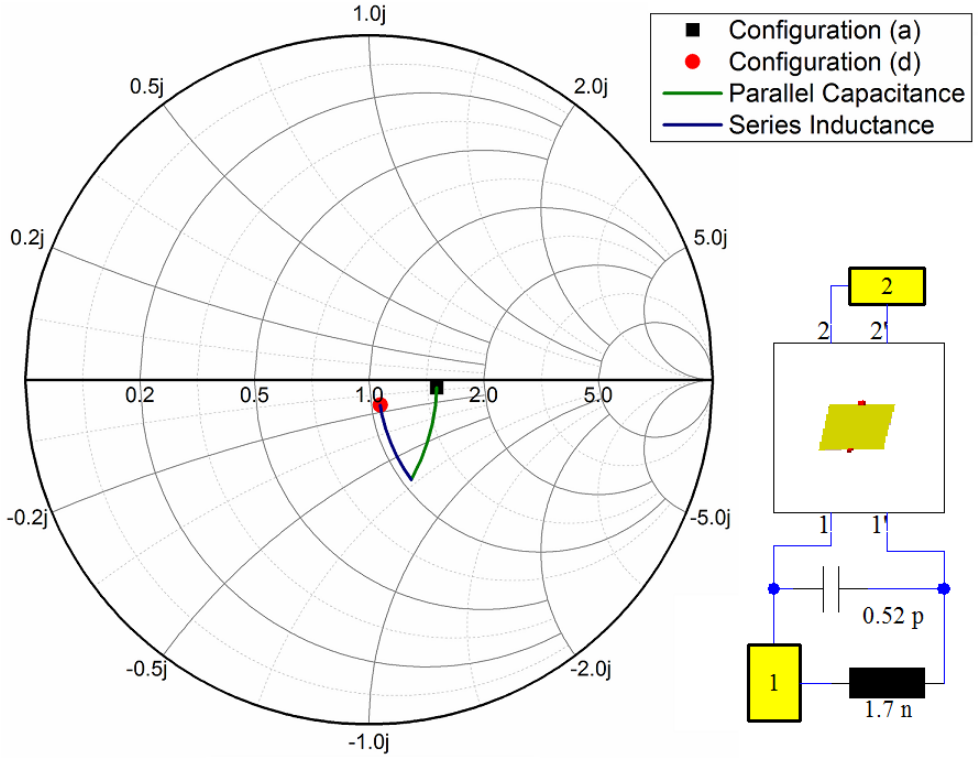

Fig. 2.8 Impedance Variation between Configurations (a) and (d)

The insertion loss also indicates the considerable mismatch between orientations, it was 2.5 dB for configuration (a), 3.3 dB for configuration (b), 3.8 dB for configuration (c) and 2.1 dB for configuration (d). Transmission coefficients are shown in Fig. 2.9.

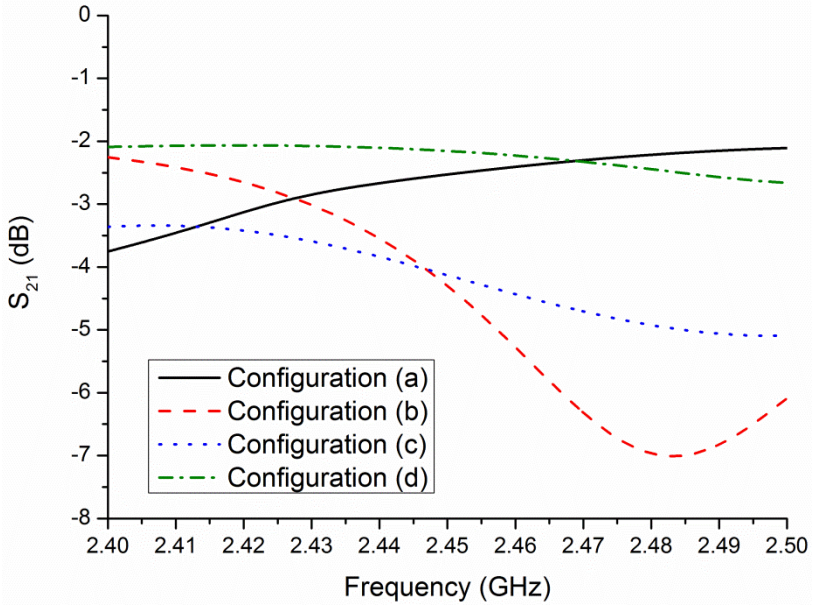

Fig. 2.9 Simulated Transmission Coefficient

A simulation was carried out in which the number of electrodes in the lattice was reduced from 49 to 25 to assess the impact of the electrode number on the transmission line performance. Both the parallel and perpendicular orientations saw a reduction in capacitance and inductance due to the removal of the electrodes as would be expected.

Increasing bus bar spacing was also simulated to assess the impact on the interaction. In both parallel and perpendicular cases there was an increase in inductance due increased current flow on the electrodes between the bus bars.

The FR-4 substitute is imitating the lattice structure found on a 6 × 6″ (152.4 × 152.4 mm) crystalline silicon solar cells but these cells are also commonly manufactured as 3 × 6″ cells (76.2 × 152.4 mm). To assess the impact of reducing the cell width the FR-4 substitute was reduced to 66.5 × 133 mm. This cell was simulated in the parallel orientation as this maintains the 133 mm CPW length. It was found that reducing the

length of the electrodes reduced the capacitance however greater current flow along the outer sections of the lattice resulted in a slight rise in inductance, shown in Fig. 2.10.

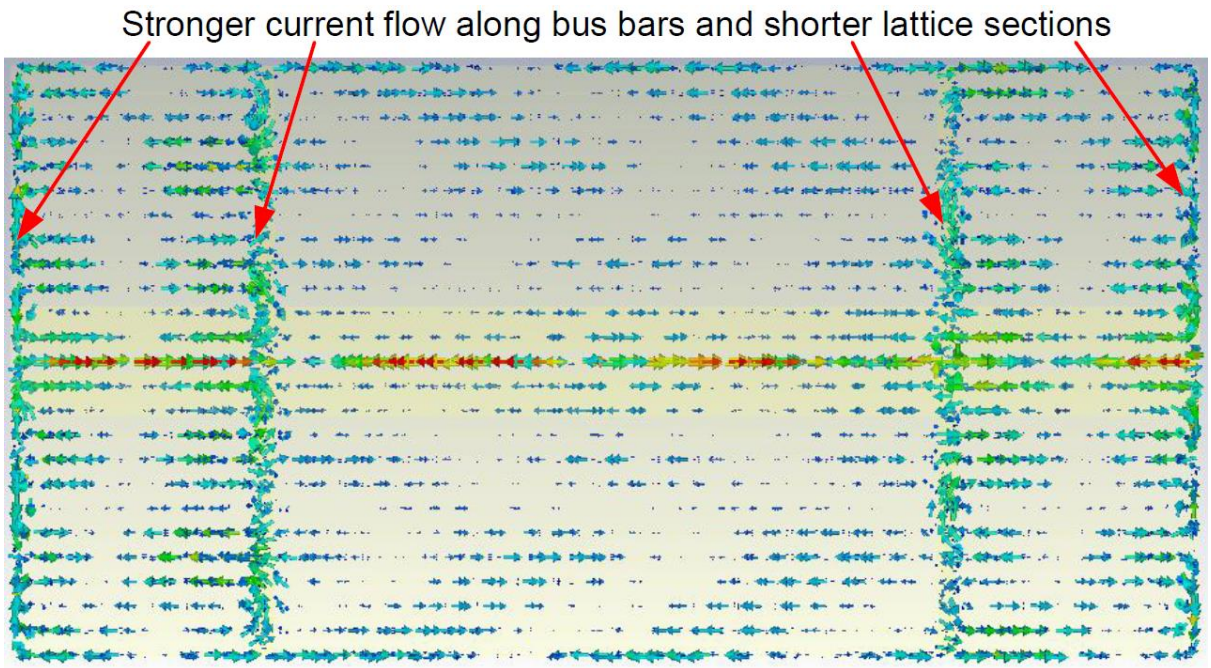

Fig. 2.10 Current Flow on Lattice of 66.5 × 133 mm Substitute Cell

2.2 Antennas and the Solar Lattice

To analyse the contributing factors, simulations were carried out in which the IFA grounding stub was connected directly to the ground plane through the substrate and the antenna was fed directly through the substrate as shown in Fig. 2.11. A printed IFA was chosen due to its small footprint compared to patch antennas which are commonly used above solar cells in the literature.

This configuration would not be possible in reality as it would damage the brittle solar cell. These simulations show the effect of the lattice on the antenna only i.e. removes the effect of the transmission line.

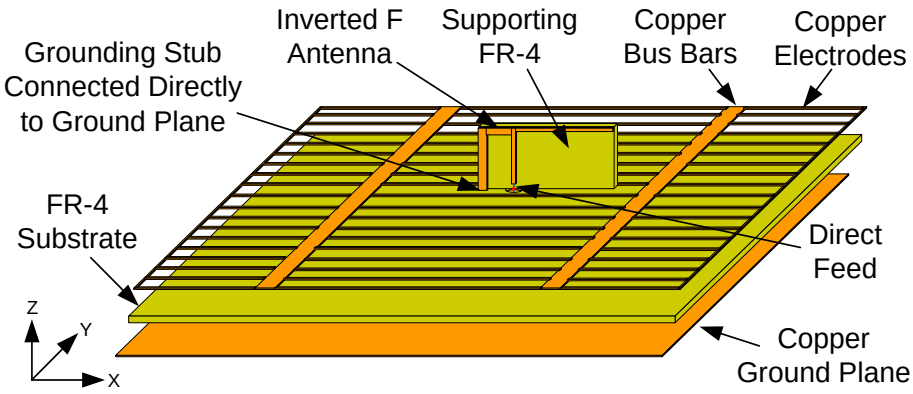

Fig. 2.11 Antenna Configuration

The antenna is an IFA printed on 0.4 mm thick FR-4 substrate which was designed above the conventional ground plane with no lattice to cover all the WLAN channels. The latticed structure was then introduced beneath the antenna for the perpendicular and parallel tests.

The antenna above the conventional ground plane was resonant at 2.454 GHz with a 6.44% bandwidth as shown in Fig. 2.12. The antenna has a simulated efficiency of 95% and 0.62 dBi boresight gain with a peak gain of 3.9 dBi. The beamwidths were 146° in the *XZ* plane and 156 in the *YZ* plane.

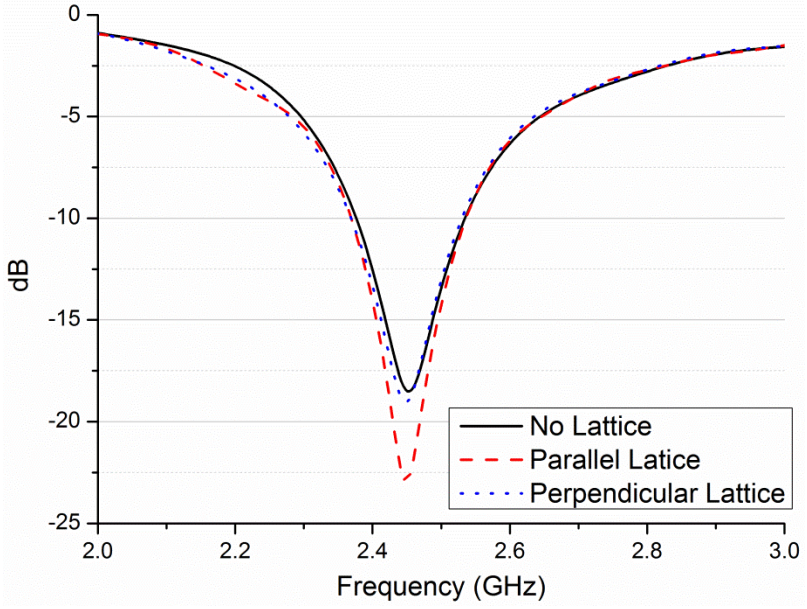

Fig. 2.12 No Transmission Line S_{11} Results

Introducing the lattice in the parallel orientation shifted the resonant frequency to 2.448 GHz and increased the bandwidth to 6.82% due to a change in the input impedance of

the antenna. The efficiency was reduced to 89% and the boresight gain was also reduced to 0.28 dBi with 3.6 dBi peak gain.

Rotating the lattice into the perpendicular changes the input impedance but the resonant frequency remains at 2.448 GHz with a bandwidth of 6.58%. Again efficiency at 92% was reduced compared to the copper ground and boresight gain was also reduced to 0.31 dBi with a peak of 3.68 dBi.

Antenna impedance variation due to the lattice is considerably lower than the transmission line variation however the downward shift in resonant frequency is evidence of the introduction of capacitive and inductive element due to the lattice, shown in Fig. 2.13.

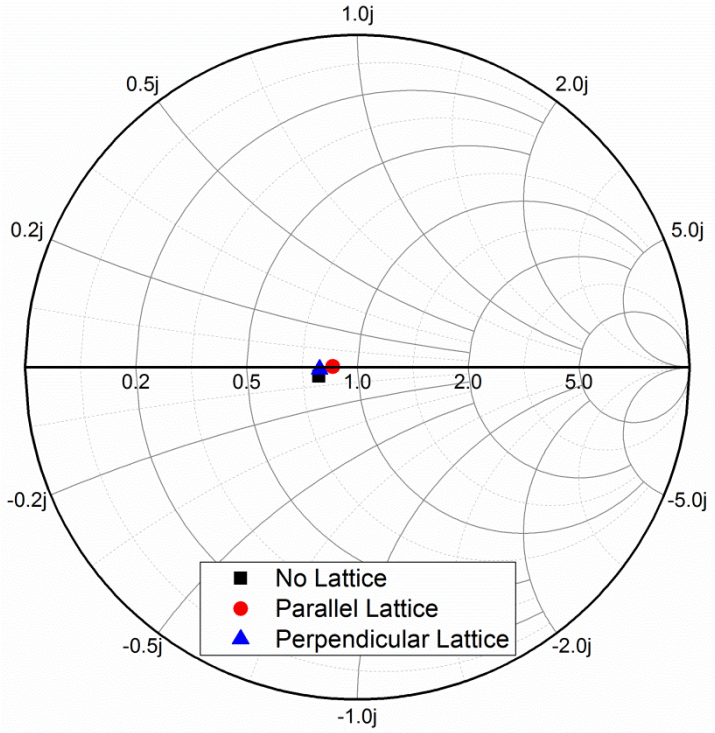

Fig. 2.13 Variation in Antenna Input Impedance

The antenna input impedance changes can be replicated by adding parallel capacitance and series inductance to the ground of the FR-4 antenna. Adding 0.06 pF of parallel capacitance and 0.2 nF of series inductance shifts the input impedance of the FR-4 antenna to match that of the parallel antenna.

2.3 Complete System

An IFA fed using a 50 Ohm grounded CPW transmission line created on a 0.4 mm thick FR-4 substrate with $\varepsilon_r = 4.3$ was used to investigate the interaction of combined antenna and transmission line with the lattice. The dimensions of the IFA, shown in Fig. 2.14, are $L_A = 19.12$ mm, $H_A = 10$ mm, $T_A = 0.784$ mm and the grounding stub dimensions are $L_S = 5.9$ mm and $T_S = 1.6$ mm.

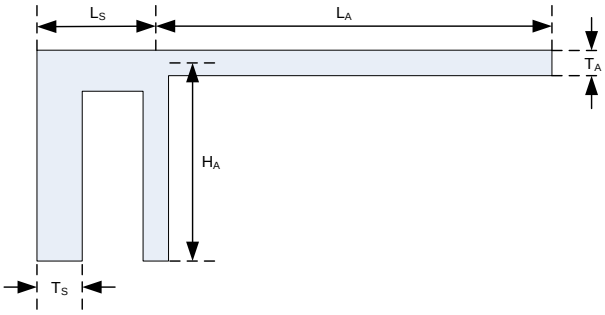

Fig. 2.14 Antenna Dimensions

As before, a 0.4 mm thick substrate with a lattice of copper electrodes printed on one side and a solid copper ground plane on the other is used to represent a solar cell. The coplanar ground is connected to the imitation cell copper ground via the SMA connector. The transmission line extends 5 mm out from the lattice to prevent shorting between the front and rear contacts of the solar cell when the SMA is connected.

In contrast to the antenna only simulation, the complete system experiences a frequency shift as a result of a change in lattice orientation due to the transmission line impedance mismatch. The measured bandwidth of the antenna on the FR-4 covered ground plane was 4.93% and increased to 5.40% and 7.29% for the perpendicular and parallel orientations, respectively. S_{11} results are shown in Fig. 2.15

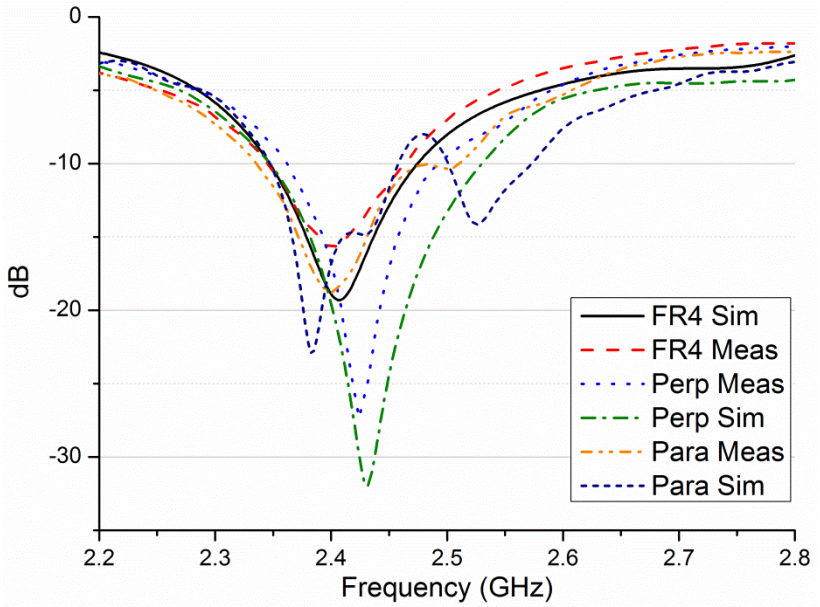

Fig. 2.15 Complete System S_{11} Results

The antenna on the FR-4 covered ground had an efficiency of 88% with a simulated realised gain of 3.6 dBi. The perpendicular orientation had an efficiency of 62% with a peak realised gain of 2.0 dBi while in the parallel orientation was 34% with 0.3 dBi realised gain. The reduction in simulated gain for both the parallel and perpendicular orientations compared to the FR-4 covered ground plane is an indicator of the impedance mismatch due to the presence of the lattice.

2.4 Conclusion

Previous works have shown a reduction in antenna performance as a result of antenna orientation on a solar cell lattice using microstrip patch antennas. This chapter has focused on the impact of the lattice by isolating the lattice using an FR-4 based solar cell substitute.

It has been shown that crossing the solar lattice with a transmission line induces current on the solar lattice; these currents lead to variation in the transmission line impedance of 23% with the introduction of the solar lattice. Due to the a-symmetric nature of the solar lattice, there is a 10% impedance variation between orientations. It has been shown that the impedance change is due to changes in the capacitance and inductance of the transmission

line. A matching network could be used to counteract this variation in one orientation however the transmission line would still be mismatched in the orthogonal orientation.

Antennas fed directly without a transmission line have shown greater resilience to impedance mismatch than the transmission line, experiencing an 8% impedance variation with change in orientation. Despite this the introduction of the solar lattice still has an impact on the antenna performance with 6% lower efficiency and 0.3 dB less gain compared to the no lattice case. The antenna is also found to have differing levels of interaction with the solar lattice depending on its orientation such as a 3% efficiency difference between orientations.

The complete system exhibits similar sensitivity to orientation with efficiency reduced to 62% with the introduction of the perpendicular lattice and 34% with the introduction of the parallel lattice. This clearly demonstrates a need to isolate the transmission line from the solar lattice as will be demonstrated in Chapter 3.

3 MULTICRYSTALLINE SOLAR CELL AS GROUND PLANE FOR IFA

In an ideal scenario the RF ground would be a homogeneous conductor with $\sigma = \infty$, however in addition to the latticed electrodes, solar cells contain a photosensitive material between the front and rear electrical contacts which also interacts with radiating structures. This material is usually a semiconductor with a high dielectric constant and a conductivity which varies depending on the light intensity [44]. This conductivity variation can affect the antenna performance when the homogeneous rear contact of a crystalline silicon cell is used as RF ground.

Additionally solar cells absorb photons which provide enough energy for electrons to break free from their bounding atoms creating the potential difference between the cell contacts. Under increased levels of insolation more energy is absorbed than can be utilised in this process and the excess is released as heat [8]. In [45] the influence of solar heating on the performance of a patch antenna integrated with a multi-crystalline silicon solar cell was reported. It was found that the temperature of the solar cell after 30 minutes of exposure to a 1000 W/m^2 light source did not significantly affect the antenna performance. The dielectric substrate used to isolate the patch from the solar cell exhibited less temperature stability.

In this chapter a sample multi-crystalline silicon solar cell produced by Solland is integrated with Inverted-F Antennas positioned in three configurations to investigate the interaction with a full solar cell. The solar cell consists of three elements, a latticed anode front contact, a cathode layer rear contact and a semiconductor material between the contacts. Two perpendicularly oriented 2 mm wide bus-bars, 74.18 mm apart, interconnect the 57×0.1 mm wide electrode wires which form the lattice. The semiconductor is a multicrystalline silicon layer and is simulated with a permittivity of 20 and an electrical conductivity of 242,270 S/m for exposed silicon and 500 S/m for shaded silicon. The cathode layer of the solar cell consists of a homogeneous layer of aluminium.

The solar cell can produce 3.5 W under irradiance of 1000 W/m^2 which is considerably higher than most alternative solar cells, such as the current record holding a-Si cell which would produce 2.5 W if manufactured to cover an identical area [14]. A low profile IFA is used to retain the high solar cell power output by minimising shadow on the solar cell. The first antenna configuration centred the antenna on the ground plane, the second configuration located the antenna above a bus bar and the final location introduced a second antenna above the opposing bus bar to create a dual antenna array.

3.1 Transmission Line Design

To counteract the interaction with the solar lattice discussed in Chapter 1, each antenna discussed in this chapter is fed using a 50 Ω microstrip transmission line (0.784 mm wide) on a 0.4 mm thick FR-4 substrate with a 6 mm wide copper ground. The ground is isolated from the anode front contact by another 0.4 mm thick FR-4 layer as shown in Fig. 3.1.

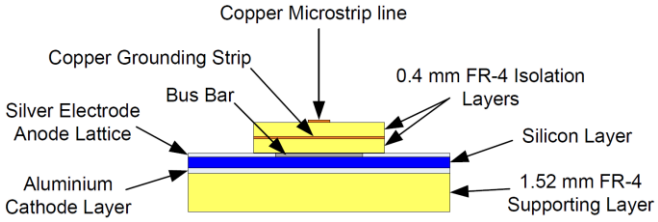

Fig. 3.1 Transmission Line Configuration

The copper ground runs the entire length of the solar cell and is connected to the cathode layer at both ends. Simulations were carried out where the connection is removed from the end of the grounding strip leaving a 156.18 mm long grounding strip. The grounding strip was further reduced to 91.34 mm long, the end of the antenna and finally the grounding strip was reduced to 69.5 mm, the end of the grounding stub. The results are arranged in pairs where colours denote orientation and symbols denote configuration, shown in Fig. 3.2.

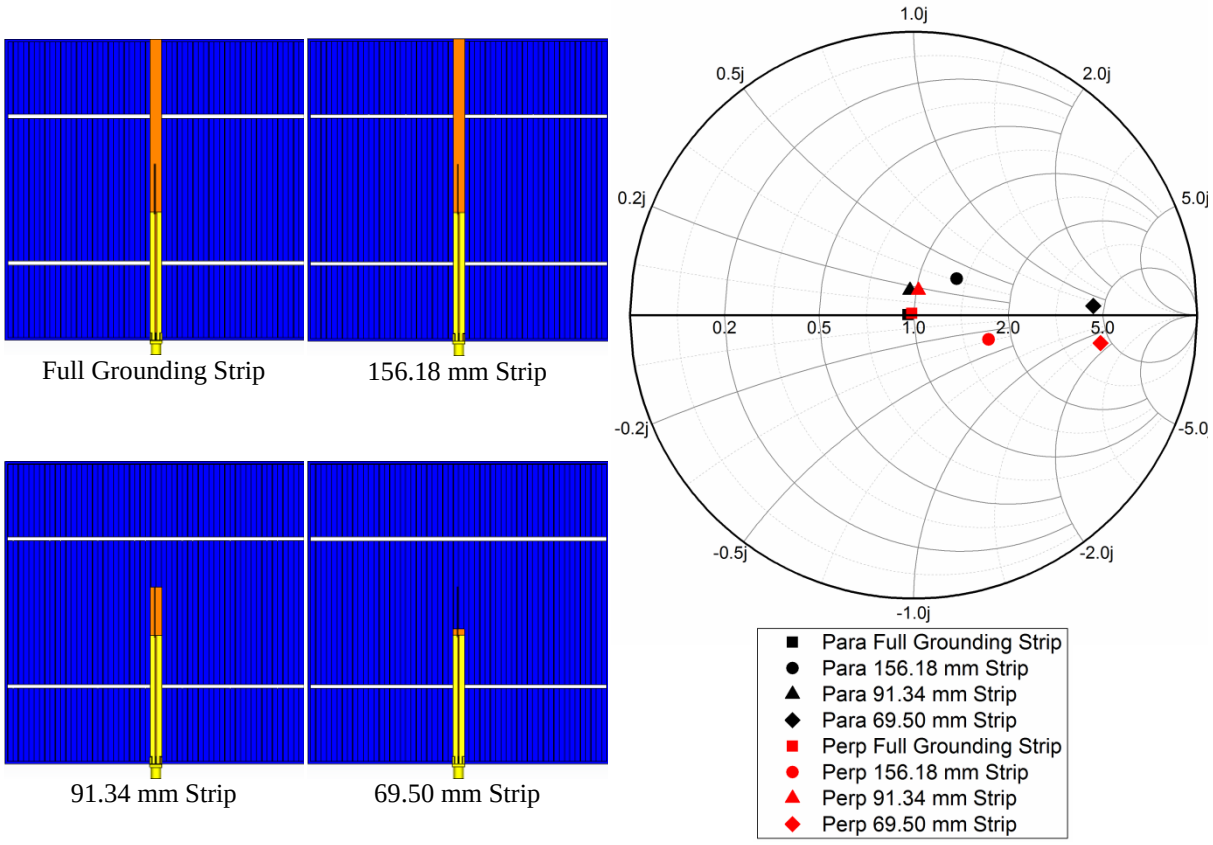

Fig. 3.2 Effect of Grounding Strip on Impedance

It is clear from the results that an IFA is less susceptible to impedance mismatch due to orientation when the grounding strip is connected at both ends of the solar cell. The 6 mm ground width adequately isolates the transmission line from the cell lattice, thereby improving gain, efficiency and bandwidth, while maximizing the surface area of the solar cell exposed to sunlight.

3.2 Antenna Design

The antenna was designed to use the cathode layer of the solar cell as a ground plane, with the transmission line positioned above the electrode lattice of the solar cell. The IFA is printed on 0.4 mm thick FR-4 with dimensions HA = 6 mm, TA = 1 mm, TS = 0.4 mm, LS = 3.5 mm and LA = 22 mm as shown in Fig. 3.3.

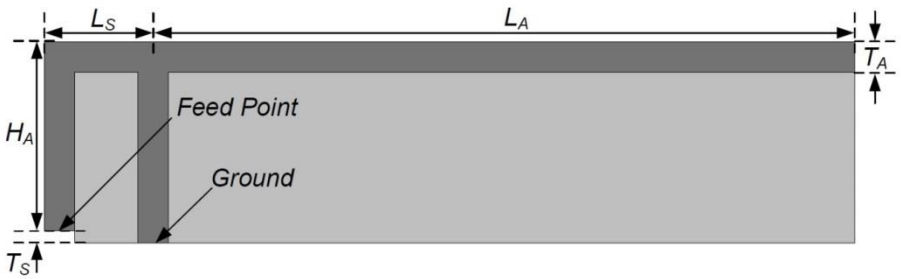

Fig. 3.3 Printed Inverted-F Antenna Dimensions

The antenna could be optimised to reduce its height, further reducing shadowing and in turn reducing the impact on the solar cell performance. However decreasing the height of the IFA will reduce its bandwidth [46]. There are however many solutions to this problem as these antenna types are commonly used in laptop design [47], [48], [49]. In some cases adjustment to the size of the ground plane and grounding stub are sufficient to achieve a higher bandwidth [47]. A better method is to consider the IFA as two separate resonating structures, an inverted L monopole and a slot created between the grounding stub and the ILA [49]. This allows optimisation of both of these resonators to give a combined bandwidth much greater than that achievable from the monopole alone. It is also possible to introduce a second resonance by adding a spiral into the resonating element of the IFA [50].

Solar cell integration rather than IFA optimisation is the focus of this chapter so a classical IFA element is used however the feed and shorting strips are reversed to facilitate improved grounding of the antenna. To ensure a direct comparison the same antenna and transmission line configuration is used in each location.

3.3 Centrally located IFA

Centrally locating the antenna in the ground plane is desirable to achieve a symmetric radiation pattern. This setup allows the antenna to be oriented either perpendicular or parallel to the lattice. The perpendicular configuration can be seen in Fig. 3.4.

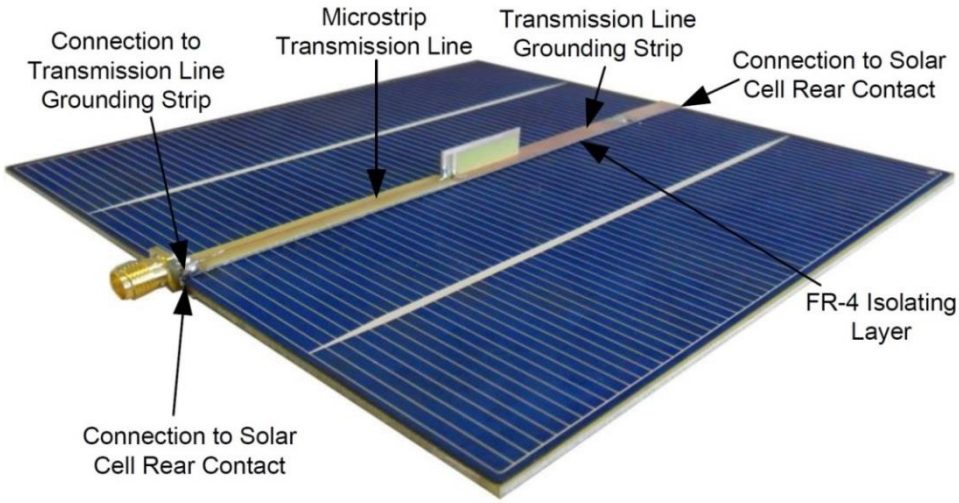

Fig. 3.4 Centrally Positioned Antenna in Perpendicular Configuration

The antenna has a height of 6.9 mm above the solar cell and along with the transmission line, has a combined footprint which is 3.94% of the solar cell surface which is a considerable reduction in antenna footprint compared to previous solar patch antenna designs which covered 12.95% of the cell area [44]. The measured and simulated results for the centrally located antenna in the (a) parallel to lattice; (b) perpendicular to lattice orientations are given in Table 3.1, with S_{11} results are shown in Fig. 3.5.

Table 3.1 Central Antenna Orientation Results

Transmission Line Orientation	Freq (GHz)	-10 dB Bandwidth (%)	Peak Gain (dBi)
Para to Lattice Sim	2.448	3.54	3.9
Para to Lattice Meas	2.450	3.47	4.4
Perp to Lattice Sim	2.456	3.72	3.7
Perp to Lattice Meas	2.459	3.83	4.3

The measured bandwidth for the parallel and perpendicular orientation was found to be 3.47% and 3.83%, respectively. The measured gain for the parallel and perpendicular orientations was 4.4 dBi and 4.3 dBi, respectively, with simulated total efficiencies of 72.5% and 69.9%. The peak gain and bandwidth are superior to reported microstrip patch solar integrations with a gain improvement of 3.2 dB for either orientation due to reduced exposure to the silicon in the solar cell. The measured 3 dB beamwidths for the proposed antenna are between 140° and 150° which are also notably wider than the solar patch antenna (75° - 95°). The beamwidth results are shown in Fig. 3.6.

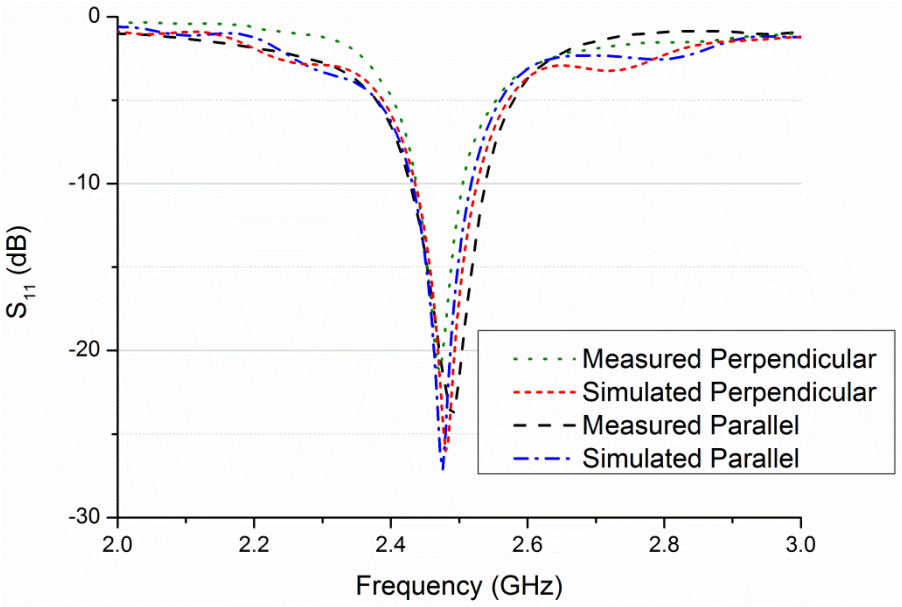

Fig. 3.5 Measured and simulated S_{11} for the parallel and perpendicular antenna

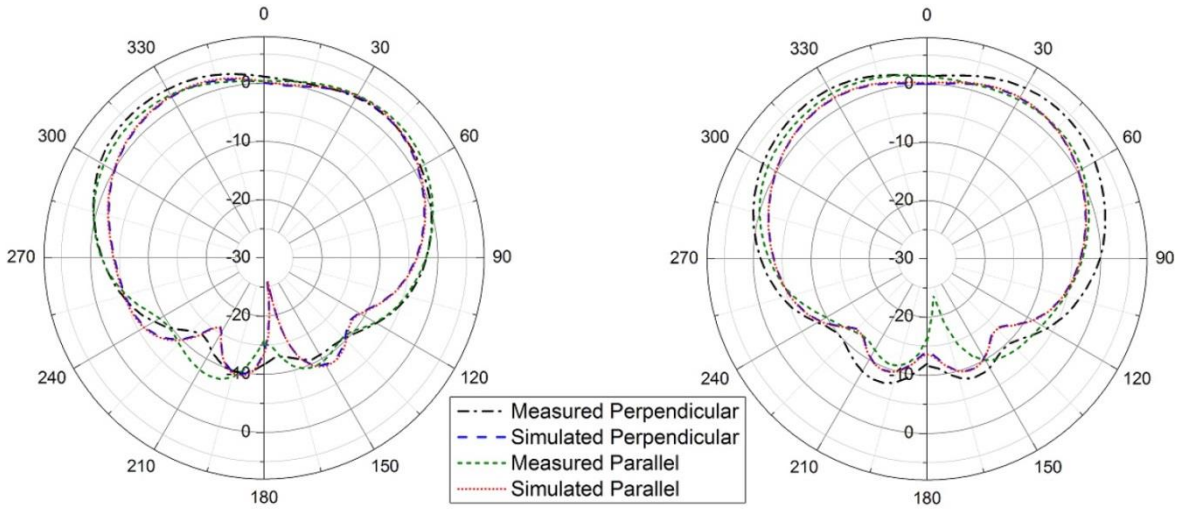

Fig. 3.6 Radiation Patterns for *YZ* Plane (Left) and *XZ* Plane (Right)

The antenna has a larger bandwidth, lower gain and efficiency in the perpendicular orientation compared to the parallel orientation due to more exposure to lossy silicon. A small frequency shift between the two orientations was observed, caused by current flow in the lattice. The current flow in the lattice electrodes is aligned with the antenna when in the parallel orientation. In the perpendicular orientation the lattice current flow is opposed to the antenna current. This results in a slight decrease in effective antenna length, upwardly shifting the resonant frequency for the perpendicular orientation.

Simulations were carried out to assess the impact on the IFA performance of varying the solar cell semiconductor electrical conductivity. In both orientations above the lattice, a conductance variation from 242,270 S/m^2 to 500 S/m^2 caused a 0.3% shift downward in frequency with no significant change in bandwidth. It should be noted that when replicating this test with measurements, caution should be used while interpreting the results as varying levels of insolation will result in a temperature change. Therefore it would be difficult to isolate the effects to purely those of the conductivity variation as has been simulated.

3.4 Offset above bus bar

Offsetting the antenna from the centre of the ground plane, shown in Fig. 3.7, is desirable to steer the antenna beam for example when the solar cell is mounted at an angle for maximum solar insolation.

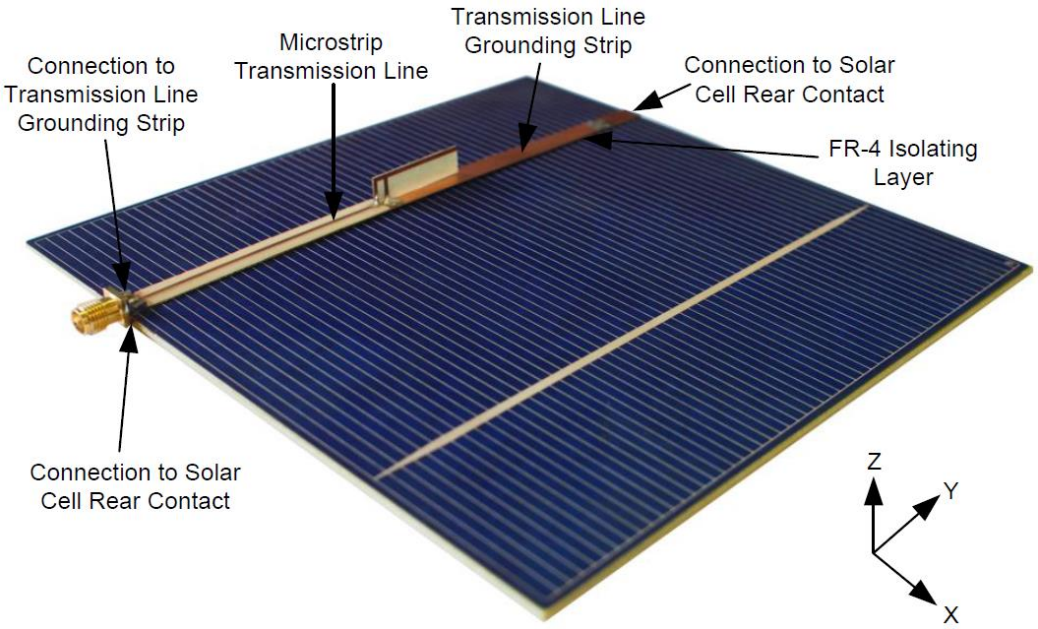

Fig. 3.7 Offset IFA Configuration

For an antenna and feed line positioned above one of the bus-bars, the area of exposed silicon is reduced by 2.65%. The antenna is resonant as 2.451 GHz with a simulated 71% efficiency and a bandwidth of 2.57%, as shown in Fig. 3.8.

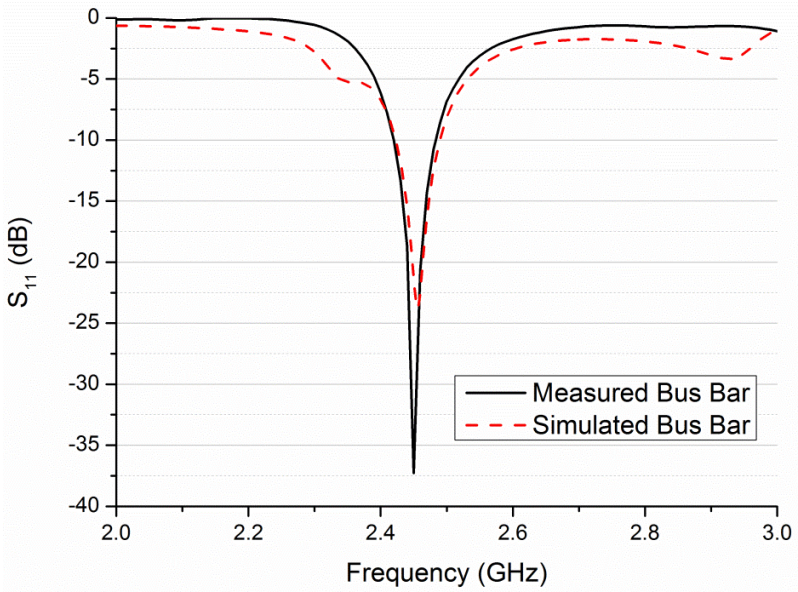

Fig. 3.8 Measured and Simulated S_{11} for the Offset Antenna

The pattern was divergent with a null located centrally above the ground plane and four lobes of ~64° beamwidth asymmetrically positioned around the null due to the off-centre position of the antenna/bus-bar with respect to the ground plane. The peak measured gain was 4.3 dBi, radiation patterns are shown in Fig. 3.9.

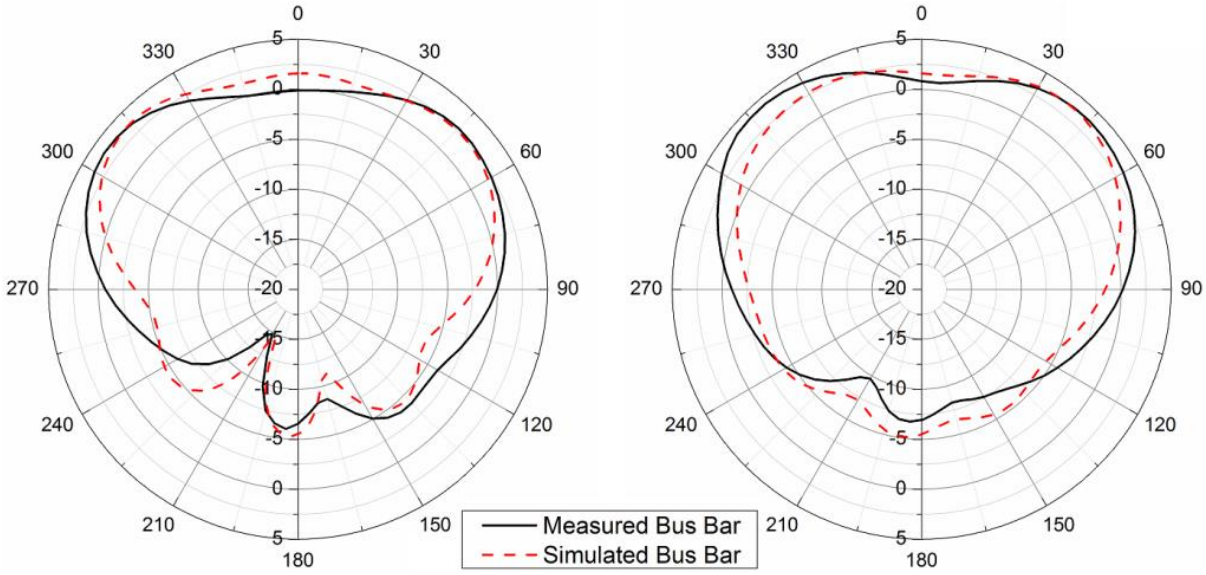

Fig. 3.9 Radiation Patterns for *YZ* Plane (Left) and *XZ* Plane (Right)

3.5 Dual IFA Array

To improve the radiation symmetry and gain, an array was configured using an antenna on each bus-bar spaced 76.18 mm apart as shown in Fig. 3.10.

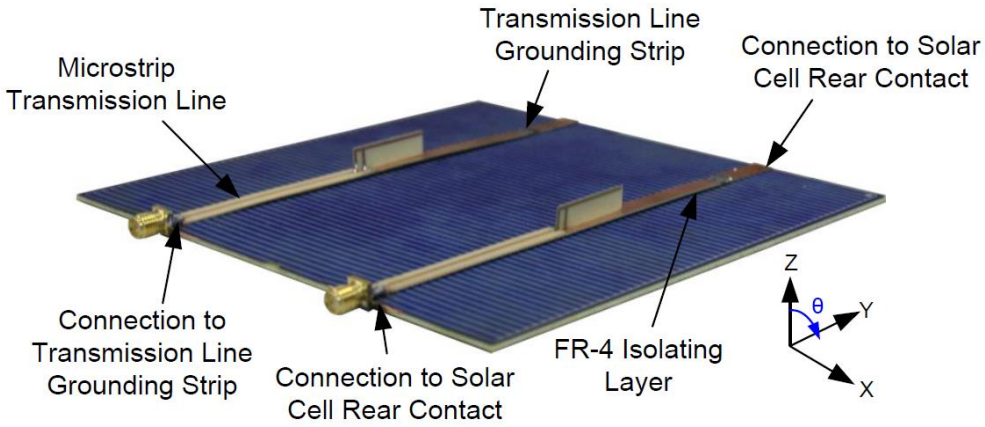

Fig. 3.10 Dual Antenna Configuration

While there is a cost in terms of a 5.30% solar shadow of the cell area, it is considerably less than previous solar patch antenna designs which covered up to 13% [44]. If the antennas were moved off the bus bars and closer to each other, there would be a solar shadow of 7.89%. Fig. 3.11 shows that there is greater than 20 dB isolation between the two antennas. The measured bandwidth for the antenna array was 3.22%.

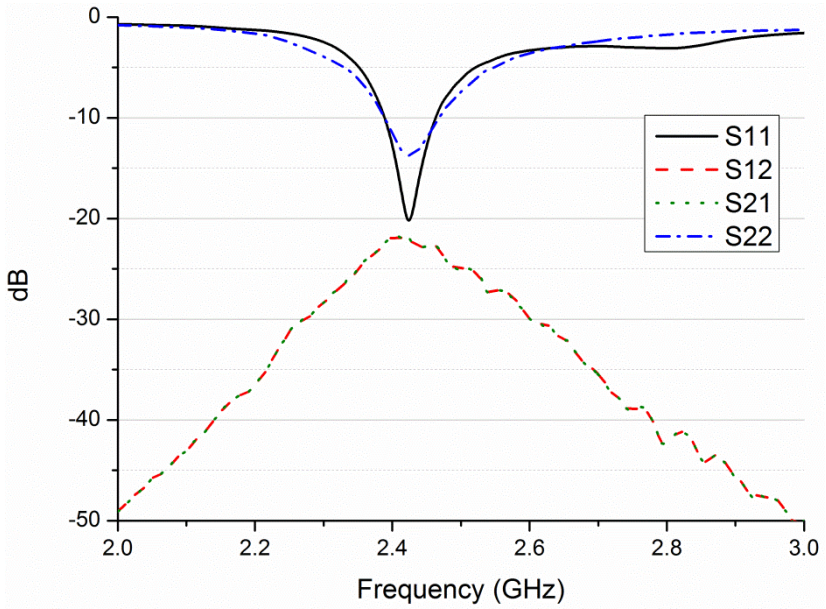

Fig. 3.11 Measured Dual Antenna Coupling

A microstrip transmission line power splitter, shown in Fig. 3.12, was used to distribute power evenly between each antenna while maintaining a 0° phase offset. Measured results show the insertion loss at the outputs to be 3.5 dB and 3.9 dB with a phase offset of 0.78°.

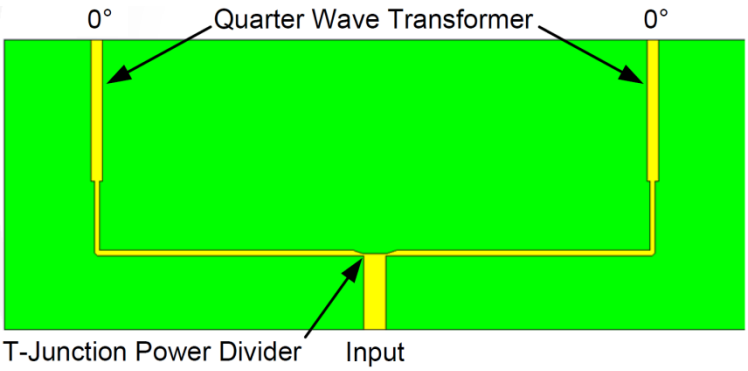

Fig. 3.12 Microstrip Power Divider Configuration

The measured radiation pattern is more focused with 6.5 dBi gain and 3 dB beamwidths of 60.2º and 144.8º for XZ and YZ planes respectively, shown in Fig. 3.13. The simulated efficiency was 67.37%. This is a 2.2 dB gain improvement over a single antenna centrally-positioned on the solar cell (off bus-bar) and is more suited to applications that require greater range. Antenna position results are shown in Table 3.2.

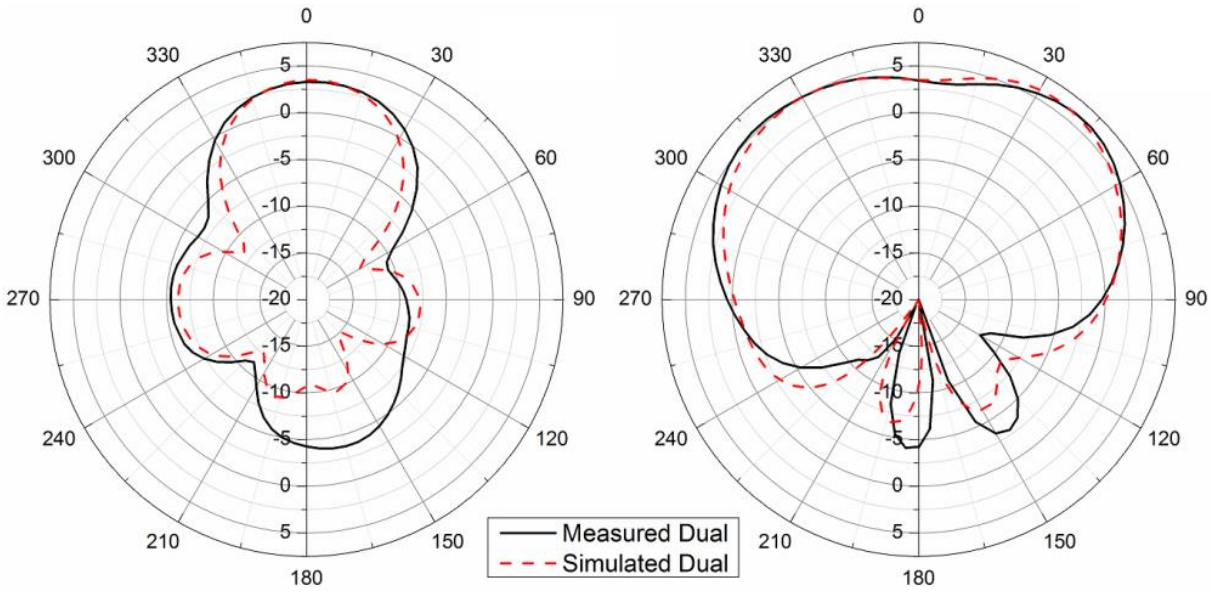

Fig. 3.13 Radiation Pattern for *XZ* Plane (Left) and *YZ* Plane (Right)

Table 3.2 Measured Dual Antenna Position Results

Antenna Configuration	Realized Gain (dBi)	Beamwidth (°)	
		XZ Plane	*YZ* Plane
Single Antenna off Bus-Bar	4.3	152.4	141.0
Dual Antenna on Bus-Bars	6.5	60.2	144.8

The antenna S_{11} was measured under various levels of insolation. The solar test light was off for the first measurement, and the light intensity was 94 Lux and the cell surface temperature was 20°C. The light was turned on and the S_{11} was recorded immediately; the light intensity was 26600 Lux and the surface temperature was 23°C. The light was left on for a further 5 minutes and the S_{11} was again recorded; the light intensity was 28100 Lux and the surface temperature was 46°C. The measured S_{11} is shown in Fig. 3.14; a 0.8% frequency shift is observed after the light source is turned on possibly due to electrical conductivity variation as discussed in Section 3.3. The curve appears to degrade as the cell heats up due to the level of insolation.

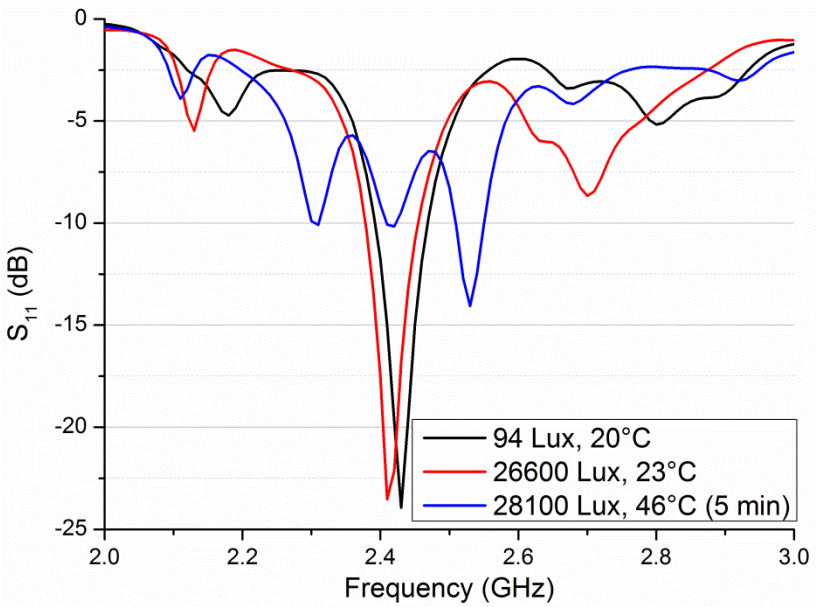

Fig. 3.14 Dual Antenna S_{11} for Different Insolation Levels

3.6 Beam Switching

Blind zones due to the relatively narrow 60.2º beamwidth of the antenna array in the *XZ* plane can be counteracted by implementing beam switching. Measurements were carried out with phase shifts Δφ = 0º, +90º and ─90º between the feeds to the two antennas.

The Δφ = 0º phase shift was obtained using the microstrip power splitter with quarter wave transformers discussed in Section 3.5. A single-box branch line coupler was used to produce the Δφ = +90º and Δφ = ─90º phase shifts as shown in Fig. 3.15. The branch line coupler created a phase offset of 89.55° with insertion loss of 3.9 dB and 2.5 dB at the outputs.

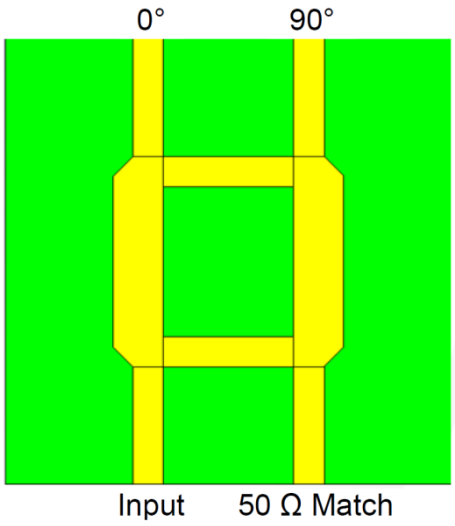

Fig. 3.15 Branchline Coupler Configuration

With a Δφ = 0º phase shift, the main lobe has a peak broadside gain of 3.33 dBi. The Δφ = +90º phase shift produces a 5.24 dBi peak gain at θ = +39º. The Δφ = ─90º phase shift provides a 4.52 dBi gain main lobe at θ = ─31º. Measured radiation patterns for the beam switching are shown in Fig. 3.16.

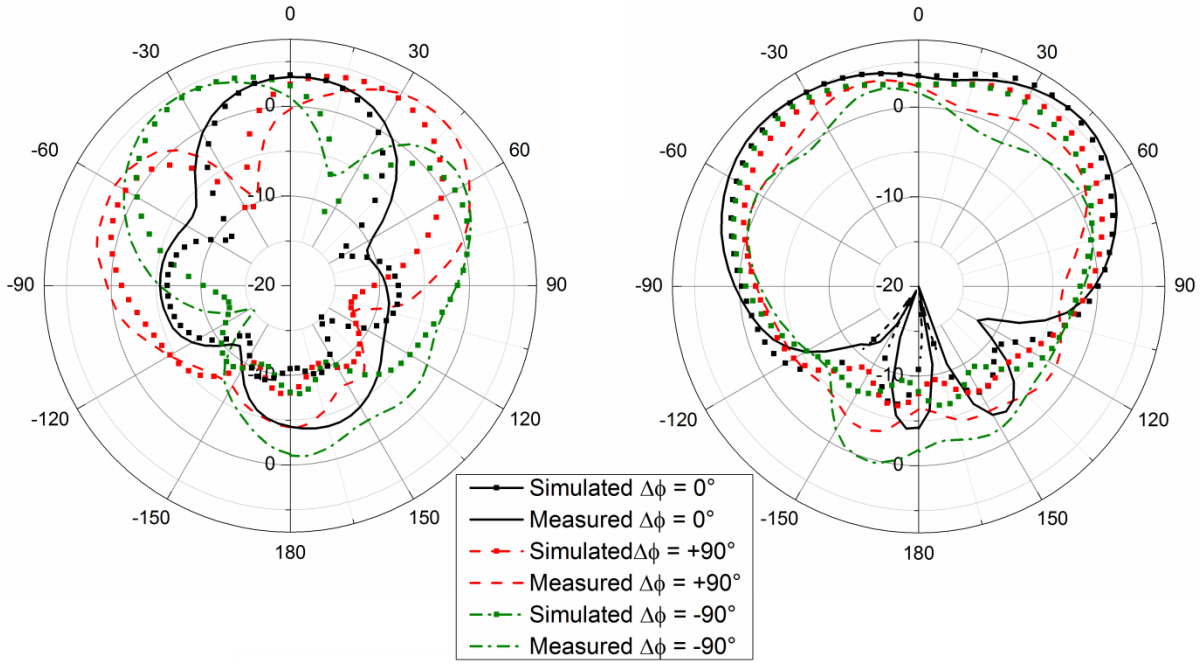

Fig. 3.16 *XZ* plane (left) and *YZ* plane (right) for Array Phase Offset (Δφ)

3.7 Solar Shadowing

Solar shadowing tests were carried out on the worst case scenario which was the dual antenna which covered 5.3% of the solar cell when facing directly into a light source. A 1450 Lux tungsten halogen directed light source was used to evaluate antenna shadowing on the cell. The light source is positioned 960 mm from a pivoting table used for angle of incidence measurements on solar cells. Shade due to the covered area is added to when the angles of incident light tend towards the plane of the solar cell. Extra shadows are projected from the vertical surfaces on the antenna and microstrip line profile. Antenna shadows from the *YZ* plane remain over the 6 mm wide ground plane of the microstrip line but they extend beyond its surface when the angle of incidence $\theta \geq 24^{o}$ for the *XZ* plane.

The shadow cast by the antenna and its transmission line minus the lattice as a result of the angle of the incidence was measured. For $\theta = 0^{o}$, 5.30% shadowing of the solar cell area occurs. For $\theta = 30^{o}$ it increases to 6.18% and for $\theta = 60^{o}$, shadowing accounts for 9.65% coverage.

The effect of shadowing on the solar cell output was assessed by measuring the open-circuit voltage (Voc) and short-circuit current (Isc) for each of the sampled incident angles, shown in Table 3.3.

Table 3.3 V_{oc} and I_{sc} Results

Incident Angle	Shade (%)	V_{oc} (V)	I_{sc} (A)
No Antenna 0º	0	0.499	4.03
No Antenna 30º	0	0.513	3.01
No Antenna 60º	0	0.518	1.30
Dual Antenna 0º	5.30	0.506	3.81
Dual Antenna 30º	6.18	0.511	2.88
Dual Antenna 60º	9.65	0.515	1.26

The Voc increases suggest that the addition of the antenna and the oblique incident angles allow the solar cell to cool slightly, thereby increasing the solar efficiency. Isc decreases as the shadowing increases. Measured I-V Curves for each incident angle are shown in Fig. 3.17.

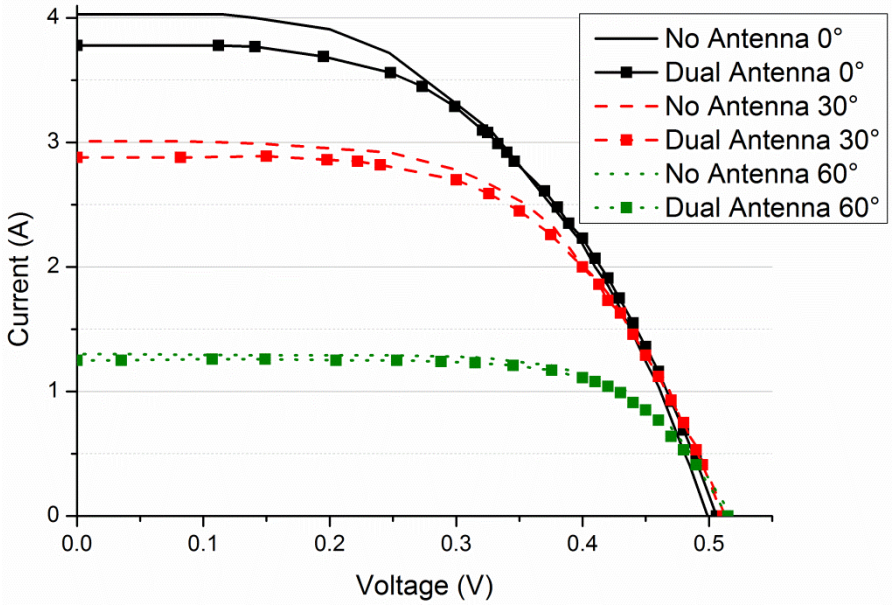

Fig. 3.17 Measured Solar Output at Various Incident Angles

In the $\theta = 0^{o}$ case, 5.30% of the solar cell area is shaded yet measured results show a 9.5% degradation in the solar output. In the 30^{o} case, 6.18% shading occurs yet the measurement shows 3.6% degradation. For the 60^{o} case, the 9.65% shadow corresponds to a 3.4% reduction in the measured output. The results indicate that the reduction of the effective solar cell area due to oblique angling of the light source is more significant than antenna shadowing, shown in Fig. 3.18.

A geometrical analysis was carried out by subtracting the lattice area from the total solar cell area and by taking account of the reduction of the effective aperture area of exposed silicon due to the angle to the light source. The maximum power point (MPP) for each angle was calculated from the measured data. This analysis shows that for a 0° angle, there is 22,845 mm^2 of exposed silicon and the antennas shadow covers 1,214 mm^2 (5.3%). At a 30^{o} angle, the silicon area directly facing the light source is reduced to 19,785 mm^2 (86.6%) which corresponds to 87.7% of the measured 0^{o} MPP for the solar cell without antennas. Although the shadow increases in the plane of the solar cell, from the perspective of the collimated light source there is only shadow cast over 942 mm^2 (4.8%) of exposed silicon similar to the 4.3% reduction in Isc. Similarly, the 60^{o} case is reduced to 11,423 mm^2 (50%) of the available silicon and produces 45.0% of the measured 0^{o} MPP. The antenna shadow covers 335 mm^2 (2.9%) which is in line with the 3.1% reduction in Isc.

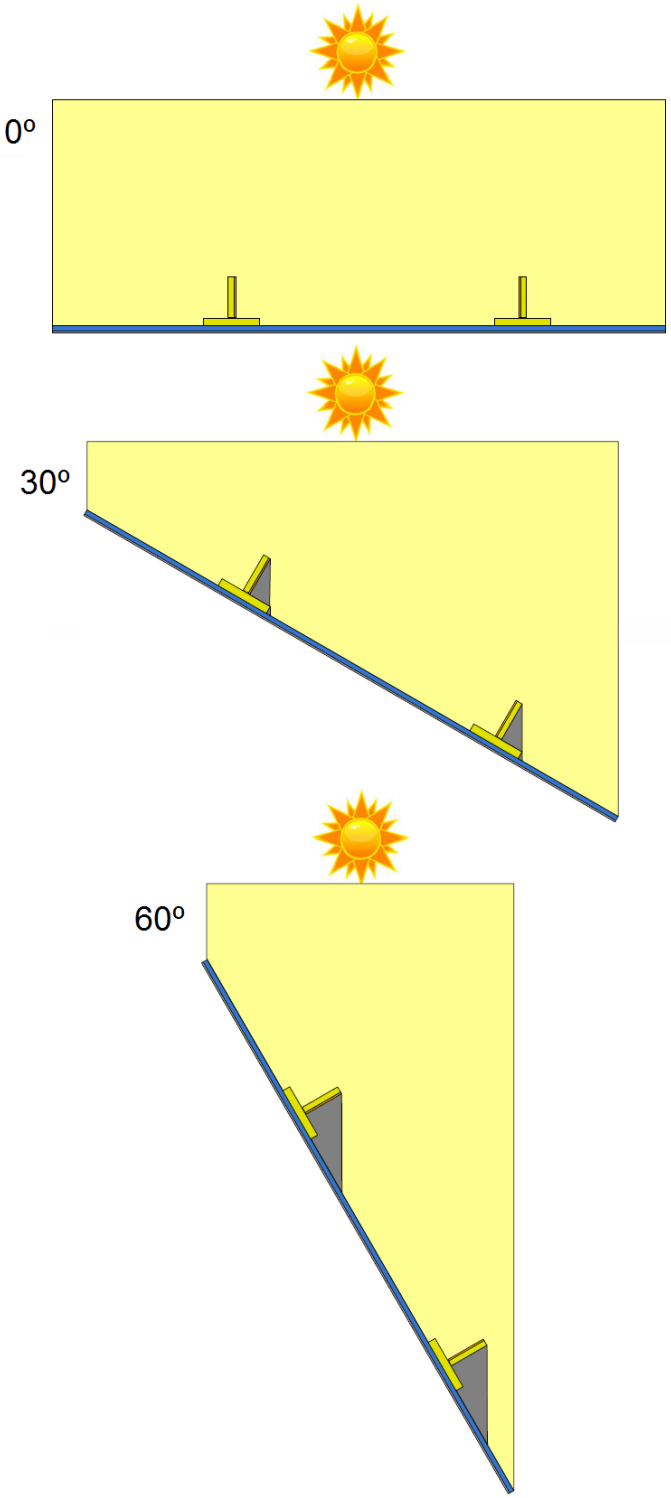

Fig. 3.18 Reduction in Solar Capture Area due to Oblique Incident Angles

3.8 Application: Greenhouse Sensor

Remote monitoring of environmental conditions for control of temperature and humidity in horticultural growing houses is one of the emerging applications where autonomous sensors are linked with radio networks. Industrial glasshouses like Thanet Earth, shown in Fig. 3.19, can be 8 m high with an area of 0.90 km^2 and battery maintenance of portable units can become a considerable expense.

Fig. 3.19 Thanet Earth Industrial Greenhouse [52]

Wireless sensor nodes are envisaged located throughout the greenhouse positioned on growing tables as required. A master node located in the rafters of the building could relay measured data to a central monitoring system, shown in Fig. 3.20. The wide beamwidths of the solar antennas discussed in this chapter mean the sensor could be better positioned to optimise solar collection while maintaining an RF link to the master node.

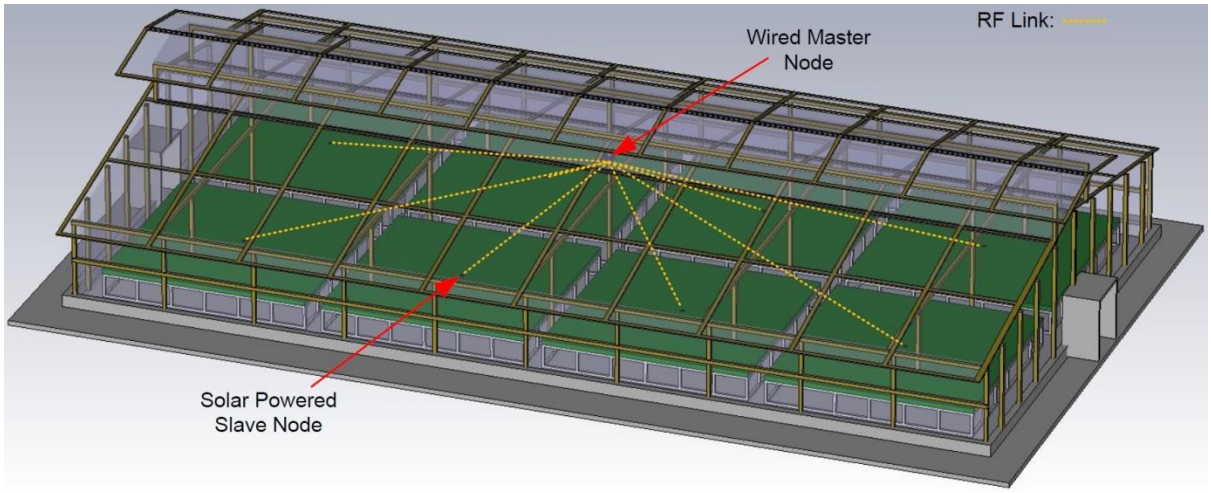

Fig. 3.20 Proposed Wireless Sensor Configuration

The solar antenna uses a 3 W solar cell which delivers a high current but low voltage. Boost converters which raise the 0.5 V output to a more useable range of 1.8 V to 5 V can usually only output 100's of mAs with such low input voltages. Super capacitors could be implemented as a reservoir before the boost converter allowing the solar cell to charge the capacitor with its maximum current output during periods of sufficient insolation. The boost converter could then slowly charge a second bank of capacitors to the higher voltage required by the microcontroller and the sensors, this would reduce the output variation due to an intermittent light source. A device based on super capacitors would present considerable initial investment however, a maintenance technician would not be required, there would be no replacement battery costs and the capacitors are capable of millions of discharge cycles while batteries which have low cycle lives and can suffer overcharge and overheat failures [53].

It is common for the individual sensors which make up a wireless sensor to come in modular form which would allow the sensor to be reconfigured to suit different plants and environmental factors to be monitored. Ensuring that only required sensors are used reduces the power requirements of the overall wireless sensor prolonging its life. In addition the system can be designed to supply power to sensors during measurements only, common sensor active power requirements are shown in Table IV.

TABLE IV
V_{OC} AND I_{SC} RESULTS

Sensor	Power (mW)	REF
Temperature	0.03	[54]
Humidity	10	[55]
Soil Moisture	15	[56]
Light Intensity	0.6	[57]

3.9 Conclusion

The addition of a grounding strip along the length of the solar cell reduces the coupling effect of the transmission line to the solar lattice. This greatly reduces the sensitivity to antenna/feedline orientation on the lattice.

Low profile IFA antennas integrated with a photovoltaic solar cell which provide greater solar exposure and improved antenna performance have been discussed. Both the single and dual antenna designs have considerably reduced footprint when compared to previous work with patch antennas. Despite the grounding strip stretching the length of the cell, the area exposed to sunlight is 9.11% greater for the central antenna than solar patch designs in the literature when facing directly into the light source [44].

The central antenna has a slightly larger bandwidth, a significantly wider beamwidth in both the *YZ* and *XZ* directions and a gain of 4.4 dBi, a gain increase of 3.2 dB compared to previous patch integrations.

While the offset configuration minimizes impact to the solar power output, the divergent radiation pattern with a-symmetric lobes is less desirable.

The dual antenna array covers more of the solar cell area than a single element IFA but the peak gain has a 2.2 dB improvement with a slightly larger beamwidth in the *YZ* plane and the ability to cover a larger angular sector in *XZ* plane by implementing beam switching. It also compares favourably to patch antenna integrations by providing wider bandwidth and higher gain. Beam switching offers flexible pattern configurations for different mounting angles.

Shadow casting tests show that the antenna shadow has less impact than oblique angles of incidence. Oriented directly at a 1450 Lux light source, the antenna reduction of solar power output is limited to 5.5%.

4 MULTICRYSTALLINE SILICON SOLAR PANEL AS GROUND PLANE FOR CP ANTENNA

There are many applications in which linearly polarized solar antennas may not be capable of supporting a satisfactory RF link due to movement of the integrated device for example an Unmanned Aerial Vehicle (UAV) or a cubesat. Both of these devices rotate as they travel which can cause polarization mismatch, fading and flutter resulting in loss of data. Satellites also suffer from faraday rotation and ionospheric scintillation due to diffraction as the RF signal passes through electron dense ionosphere regions resulting in variations in polarization, amplitude and phase [58], [59]. Where a linearly polarized signal might disappear in a fade, a circularly-polarized signal is less sensitive to polarization mismatch losses increasing the probability of a successful transmission.

Circular-polarization in the S-band has been achieved using two linearly-polarized 70%-transparent meshed patch antennas with a 90° phase-offset sharing a single microstrip feed line [60]. The patches are designed to use the conductive shielding of a satellite as the ground plane and the solar panel glass as a substrate. Printed on non-transparent Rogers laminate without the solar cells, the antenna gain is 5.15 dBi at 2.47 GHz. However exposing the electric fields to lossy solar cells is likely to degrade the gain. The impedance bandwidth of 2% covers WiFi channels 9-14. The Left-hand Circular-Polarization (LHCP) bandwidth of 0.61% has 3-dB beamwidths of 20° and 80° in the orthogonal planes.

A 2.5 GHz cavity backed CP slot antenna [61] has potential for solar cells integration on upper surface areas without interfering with the radiated performance. The antenna and feedline are manufactured on separate substrates which add 3 mm volume below the solar cells. Measurements without solar cells showed a 3.5 dBi gain and a 2.7 dB axial-ratio in the main beam with a 60° beamwidth. The measured bandwidth was 2.39% and covered Wi-Fi channel 14.

A 3.87 GHz amorphous silicon solar cell was manufactured with an integrated crossed-slot antenna [62]. The slot is excited with a microstrip line printed on 0.76 mm thick substrate and offset beneath the slots at a 45° angle. A 3.7 dBi gain is achieved using a back reflector offset 10 mm behind the transmission line, with a 10.8 mm overall device thickness. The antenna achieves a 3.1% CP bandwidth that covers the 2.6% impedance bandwidth. The beamwidths were 46° and 71° in the *XZ*- and *YZ*-planes respectively.

This chapter will discuss a circularly-polarized solar cell antenna consisting of four low-profile printed inverted-F antennas with a groundplane of four multicrystalline silicon solar cells suited to airborne CP communications. The antennas are sandwiched between neighbouring solar cells to minimise the profile and solar shadowing ensuring 100% insolation of the multicrystalline cells when directly facing a light source. The antenna is designed to achieve CP over the WLAN channels 2.4 - 2.45 GHz. With the antennas fed individually, it is possible to alter the polarization or implement beam switching improving potential RF coverage.

4.1 Proposed Antenna Configurations

The square ground plane consisted of four of the c-Si cells described in Chapter 3 arranged to form a 322 mm wide ground plane over a lightweight support. The antenna uses the cathode layer of the solar cells as a ground plane. A strip of copper is used to connect the rear contacts of each solar cell to create a solar panel with an output of around 0.5 V and over 12 W. The solar panel and antennas are shown in Fig. 4.1.

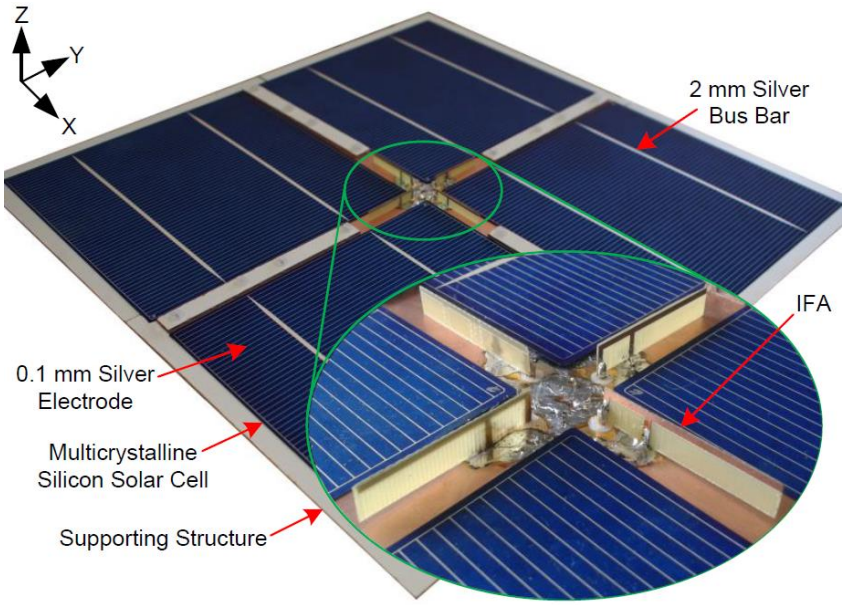

Fig. 4.1 CP solar antenna configuration

The IFA dimensions are H_A = 6 mm, T_A = 1 mm, L_A = 22.65 mm and L_S = 8.96 mm, shown in Fig. 4.2. Each antenna is positioned between each pair of solar cells 8.67 mm from the centre of the ground plane. This location allows for 100% irradiation of the solar cell when directly facing into a light source. While the low-profile of the antenna minimises shadow casting from light sources at low oblique angles, this has lower impact than the loss of light intensity at low angles.

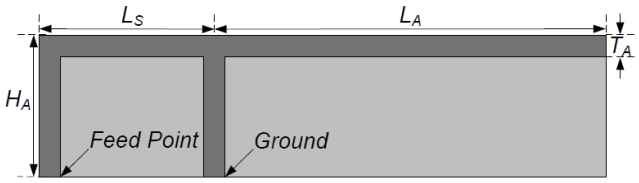

Fig. 4.2 Printed inverted-f antenna parameters

4.2 Feed Network Design

The feed line consists of a rat race coupler and two branchline couplers. The rat race coupler has two outputs with equal power but a 180° phase shift between them. Each output feeds a branchline coupler which introduces a 90° phase shift resulting in four outputs of equal power with a 90° phase shift between them.

All simulations were carried out using CST Microwave Studio. Measured results for the transmission line were used to create a touchstone file which was used to feed the antenna in the simulation. The use of a touchstone file instead of a simulated version of the transmission lines removes variation due to discrepancies in the manufacturing process. In addition the large antenna size with minute detail results in a large computational domain, introducing the transmission line into this simulation would further increase computational expense making progress slow. Identical antennas positioned above a copper ground plane and fed using the same transmission line configuration were simulated for comparison.

The feed line network has measured insertion losses of -6.9 dB, -6.6 dB, -6.8 dB and -6.5 dB from ports 2, 3, 4 and 5, respectively. The measured phase offset between ports 2 and 3 was 89.5°, between ports 3 and 4 was 90.0º, between ports 4 and 5 was 89.7° and between ports 5 and 2 was 90.9°.

4.3 Antenna Performance

The simulated and measured results for each antenna are given in Table 4.1. The simulated and measured S_{11} for each antenna is shown in Fig. 4.3 and isolation is shown in Fig. 4.4. The results show a frequency difference of less than 20 MHz (0.77%) between simulated and measured resonant frequency of each antenna. The measured bandwidth was slightly less than simulated by 0.3%. These differences are due to manufacturing discrepancies in the assembly of the four antennas and the solar panel.

Table 4.1 Individual Antenna Results

	Frequency (GHz)	-10dB Bandwidth (%)
Simulated Solar Antenna 1	2.45	1.7
Measured Solar Antenna 1	2.45	1.6
Simulated Solar Antenna 2	2.46	1.8
Measured Solar Antenna 2	2.45	1.5
Simulated Solar Antenna 3	2.45	1.7
Measured Solar Antenna 3	2.45	1.5
Simulated Solar Antenna 4	2.46	1.8
Measured Solar Antenna 4	2.45	1.6
Simulated Copper Antenna	2.42	1.7

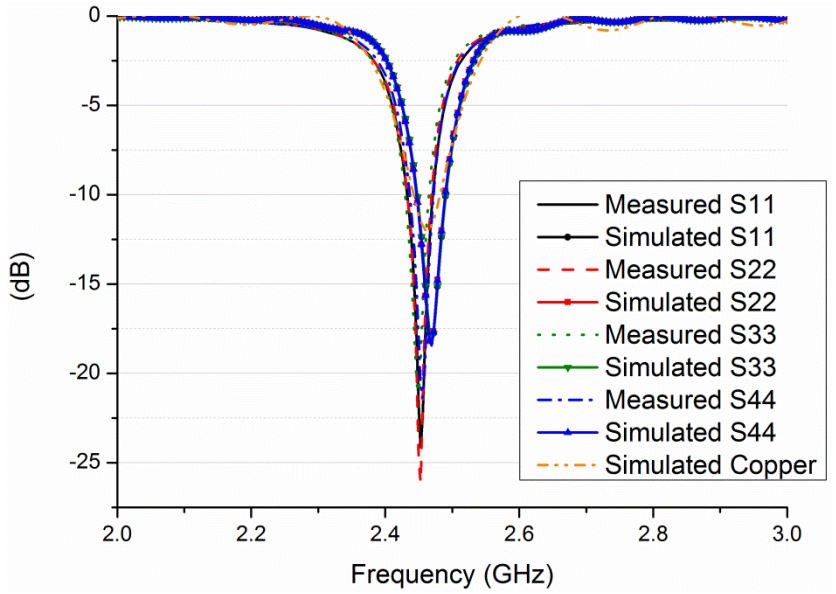

Fig. 4.3 Measured and simulated reflection coefficient for each antenna

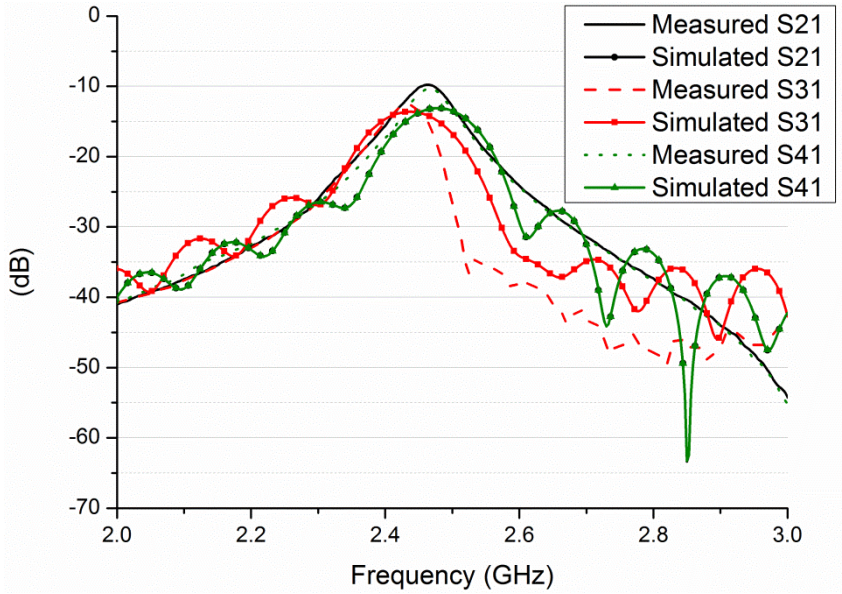

Fig. 4.4 Measured and simulated transmission coefficient between antennas

When comparing a simulated setup using a solid copper groundplane instead of multicrystalline silicon, the wider bandwidth is attributed to losses in the silicon. In addition, there is higher resonance in the solar case due to an electrical shortening of the antenna, where the silicon surface is higher than the copper surface.

Simulated and measured isolation between antennas is better than 10 dB in all cases for 2.4 - 2.45 GHz. The simulated axial-ratio is below 3 dB for 2.33 - 2.58 GHz. The measured axial-ratio is below 3 dB for 2.29 - 2.63 GHz. Axial-ratio results are shown in Fig. 4.5.

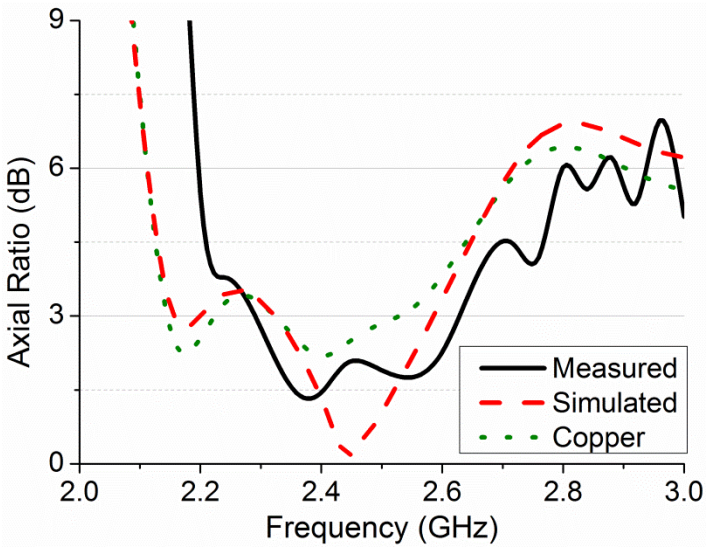

Fig. 4.5 Measured and simulated axial ratio

The feed line is configured for left-hand circular-polarization (LHCP). Measured LHCP gain for the solar antenna is 3.7 dBic at boresight while RHCP gain is -10.2 dBic. Gain results are shown in Table 4.2. While the antenna has slightly lower gain than CP meshed patch antennas [60], the IFA design offers 30% less shadowing than the meshed patch. The measured 3 dB beamwidth for the solar antenna was 50° in the *XZ* plane and 58° in the *YZ* plane. Simulated LHCP gain for the solar antenna is 4.5 dBic at boresight with 3 dB beamwidths of 62° in the *XZ* plane and 61° in the *YZ* plane. Simulated LHCP gain for the copper antenna is 4.5 dBic at boresight with 3 dB beamwidths of 63° in the *XZ* plane and 61° in the *YZ* plane. Radiation pattern plots are shown in Fig. 4.6. The antennas are optimised for integration with the solar cells, when the antenna is placed above the solid copper ground plane the input impedance of the antenna changes from 53 Ω to 107 Ω at 2.45 GHz resulting in lower gain for the copper antenna.

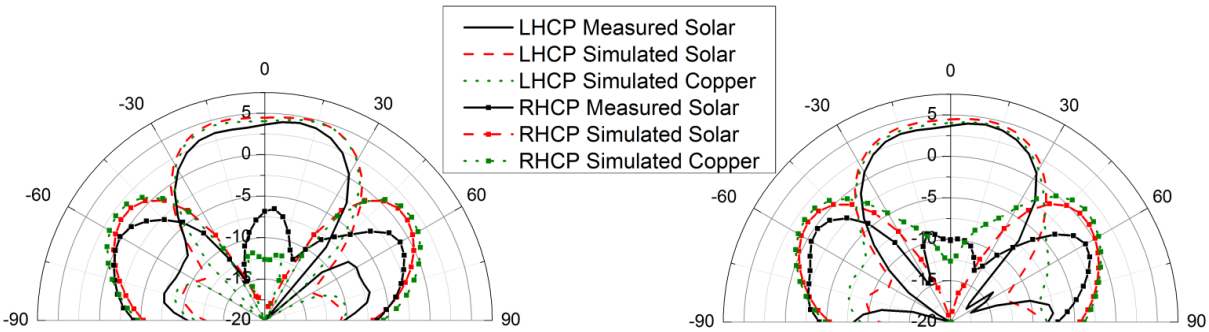

Fig. 4.6 CP Gain *XZ* (left) and *YZ* (right)

Table 4.2 Antenna Radiation Results at 2.45 GHz

Antenna	LHCP Boresight Gain (dBic)	RHCP Boresight Gain (dBic)	Axial Ratio Bandwidth (%)	LHCP 3 dB Beamwidth (°)	
				XZ	*YZ*
Meas Sol	3.7	-10.2	13.8	50	58
Sim Sol	4.5	-34.8	10.4	62	61
Sim Cop	4.0	-12.7	8.3	61	61

4.4 Polarization Reconfigurability

The ability to feed the four IFAs individually allows the antenna to be reconfigured to RHCP by reversing the feed phase offsets. The simulations in this section where carried out by feeding the ports of the individual antenna directly with signals of equal magnitude and with exact phase offsets. In reality this would not be the case as the additional length of transmission line required to create the desired phase offsets would result in differing signal magnitudes at each antenna. Fig. 4.7 shows simulated surface currents on the ground plane for both the LHCP and RHCP configurations.

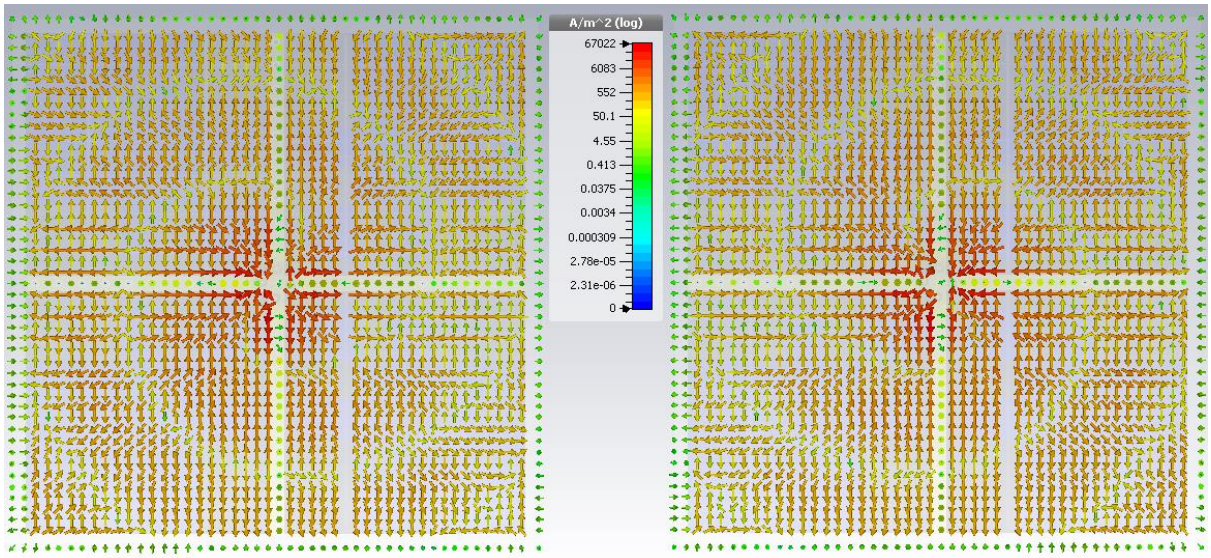

Fig. 4.7 Ground plane currents in LHCP (Left) and RHCP (Right)

Linear polarizations can be achieved by feeding two opposing antennas with a 180° phase offset while the adjacent antennas remain inactive. Simulated results show the antenna achieves 3 dB beamwidths of 51° and 114° in linear configurations and Fig. 4.8 shows the radiation patterns of two perpendicular linear polarizations.

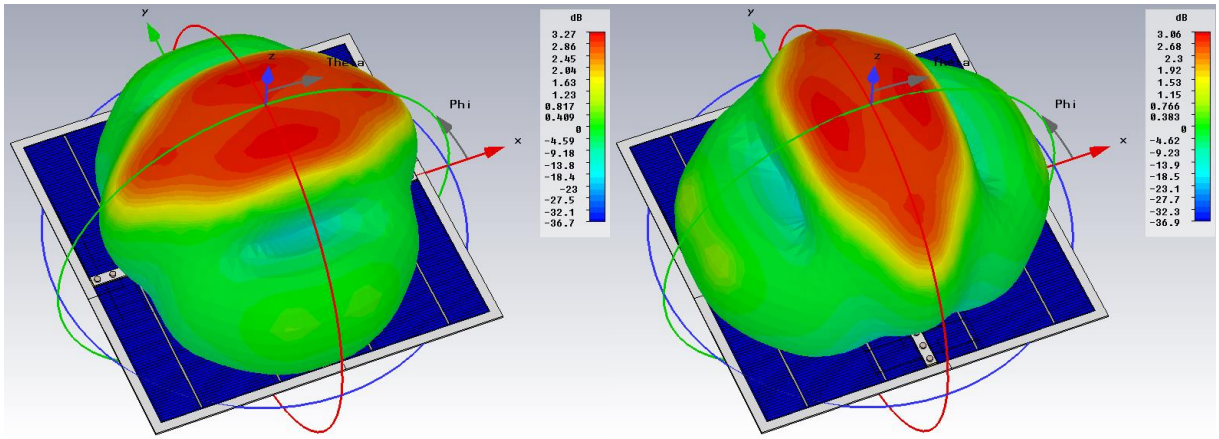

Fig. 4.8 Linear Polarization Radiation Patterns

45° Slanted polarizations are possible by feeding two adjacent antennas with a 180° phase offset while the opposing antennas remain inactive. Simulated results show that the antenna has beamwidths of 66° and 96° in the slanted polarizations however due to the off centre location of the antennas there is a peak gain away from the active antennas, shown in Fig. 4.9.

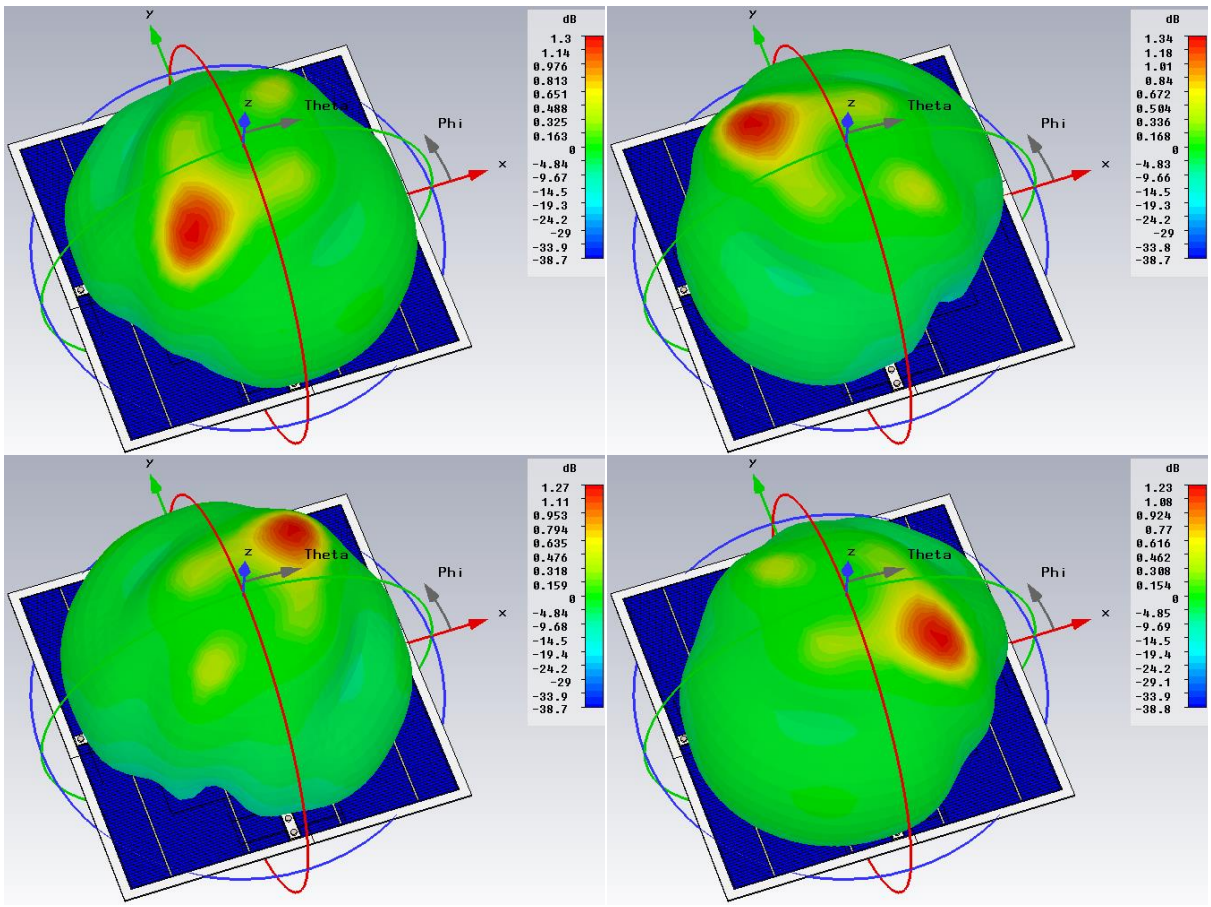

Fig. 4.9 45° Slanted Radiation Patterns

4.5 Beam Switching

Beam switching can be implemented in linear polarizations by changing the phase offset between the two antennas thus increasing coverage in linear polarizations, shown in Fig. 4.10.

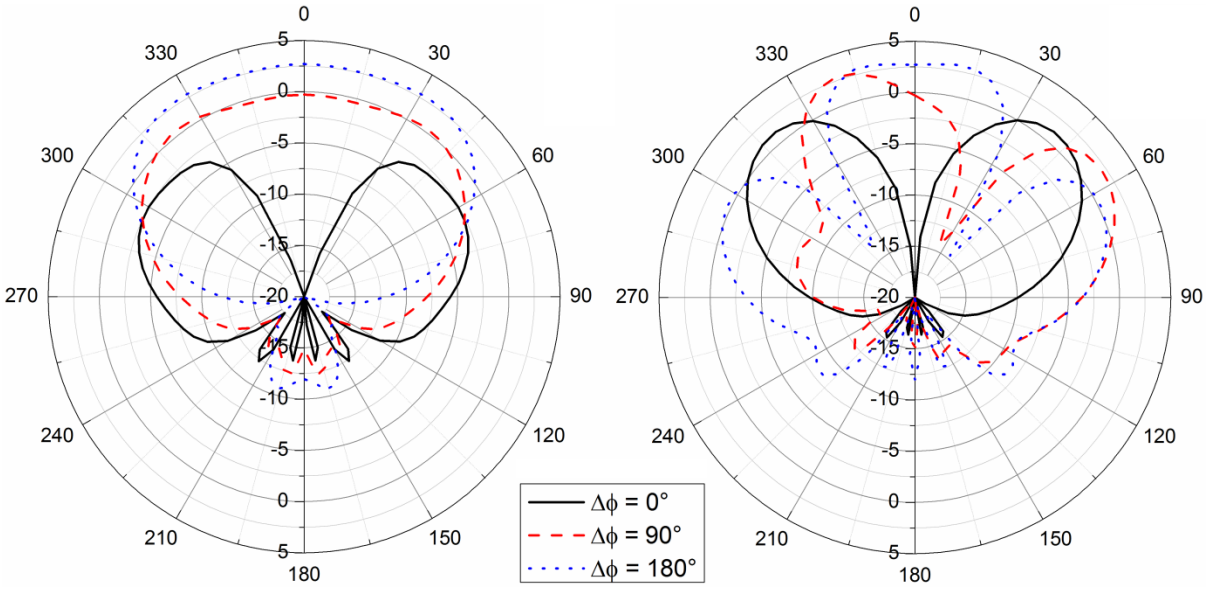

Fig. 4.10 Linear Polarization Beam Switching Radiation Patterns

The interaction between the two antennas can be seen in the e-field patterns shown in Fig. 4.11. With 180° offset the e-fields are between the two antennas resulting in a focused radiation pattern. At 0° offset the antennas interact primarily with the ground plane resulting in a divergent radiation pattern.

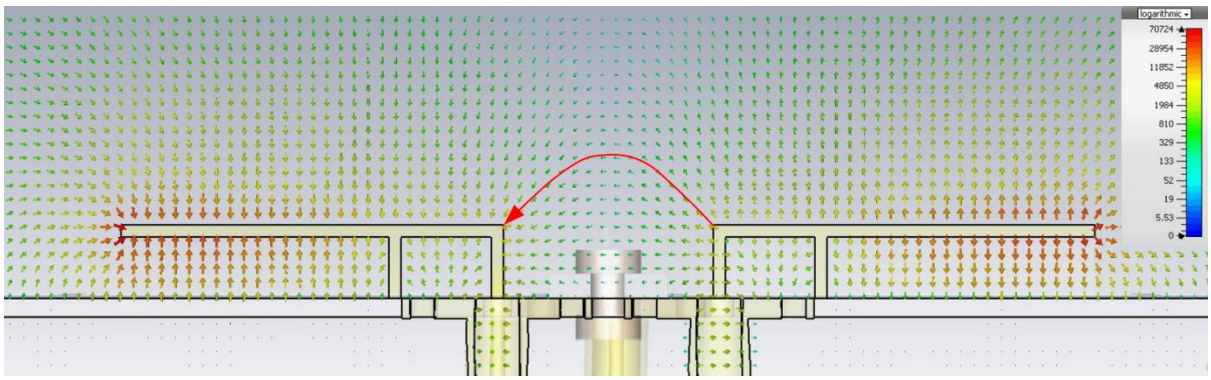

(a) Linear Polarized E-Field Δφ = 180°

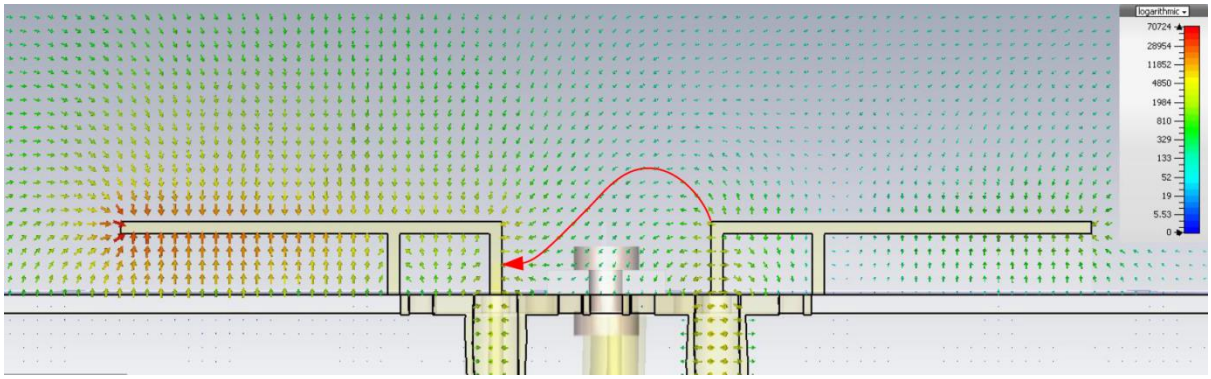

(b) Linear Polarized E-Field Δφ = 90°

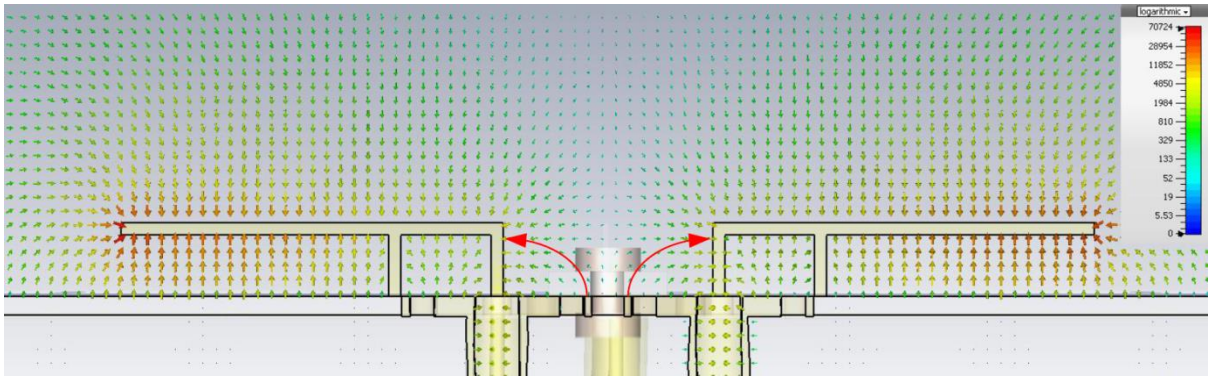

(c) Linear Polarized E-Field Δφ = 0°

Fig. 4.11 Linear Polarization E-Field Plots

Beam switching can also be implemented while maintaining circular-polarization provided the phase of the antennas feeds are Ant 1 = 0°, Ant 2 = (90° - Δφ), Ant 3 = (180° - 2Δφ) and Ant 4 = (270° - Δφ). Radiation plots of beam switching along the *XZ* axis are shown in Fig. 4.12.

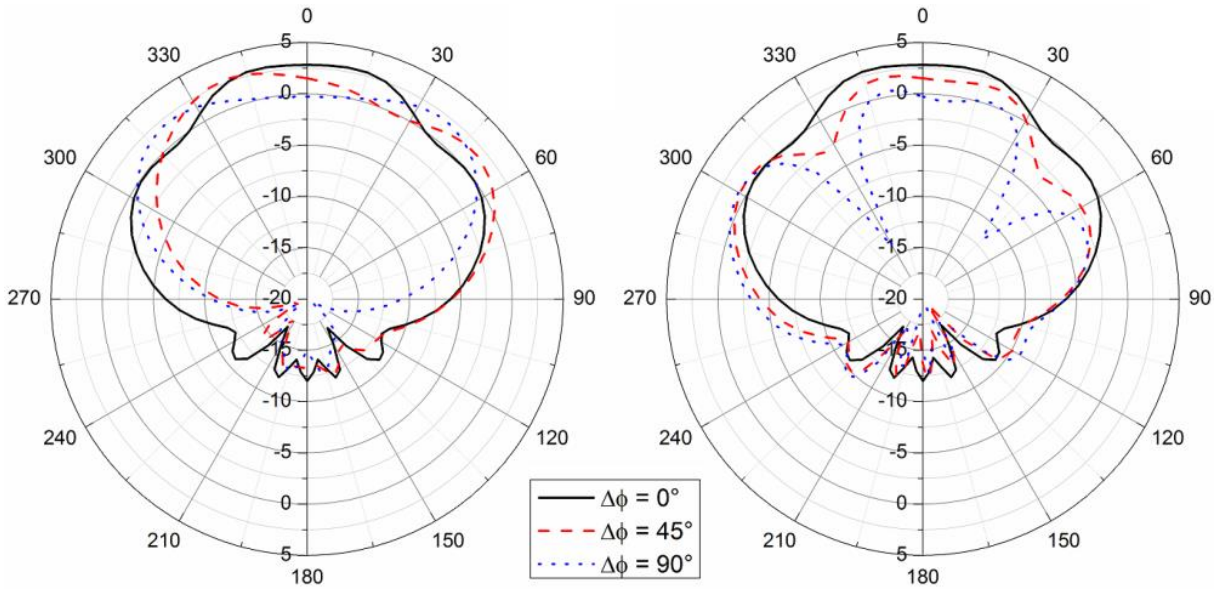

Fig. 4.12 Circular-Polarization Beam Switching Radiation Patterns

The beam steers in a similar fashion to the linear pattern with a divergent pattern at 90° resulting in a 121° *XZ* beamwidth. The axial ratio pattern is much narrower than the radiation pattern however it does follow the same orientation in the *XZ* plane during beam switching as shown in Fig. 4.13.

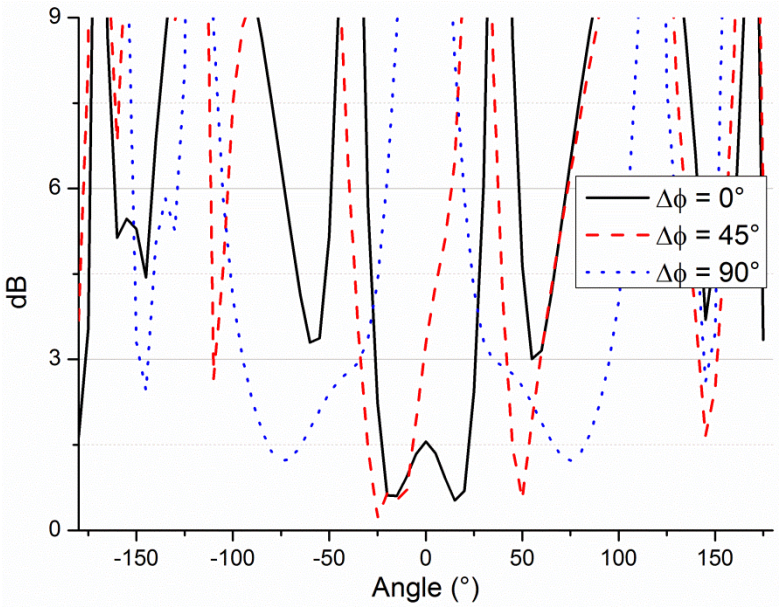

Fig. 4.13 Circular-Polarization Beam Switching Axial Ratio

4.6 Application: Weather Balloon

Low-altitude airborne communication nodes are envisaged for improved wireless communications over remote areas and to support emergency services responding to large scale natural disasters [63]. Short-term systems can be deployed rapidly to the lower troposphere, while longer-term systems are placed in the upper troposphere or stratosphere. Networked nodes are to communicate with each other and with ground users as shown in Fig. 4.14.

Entirely solar powered, each node makes use of increased solar energy availability at altitude to charge lithium batteries for low light conditions [64]. TETRA, WiFi and WiMAX radios have been tested on tethered balloons [65], with TETRA achieving 9 km but with WiFi achieving higher data rates at 1 km. The proliferation of WiFi enabled consumer devices also

makes it a viable aid in emergency situations. Airborne antennas can be randomly oriented, so circularly-polarized (CP) devices are considered.

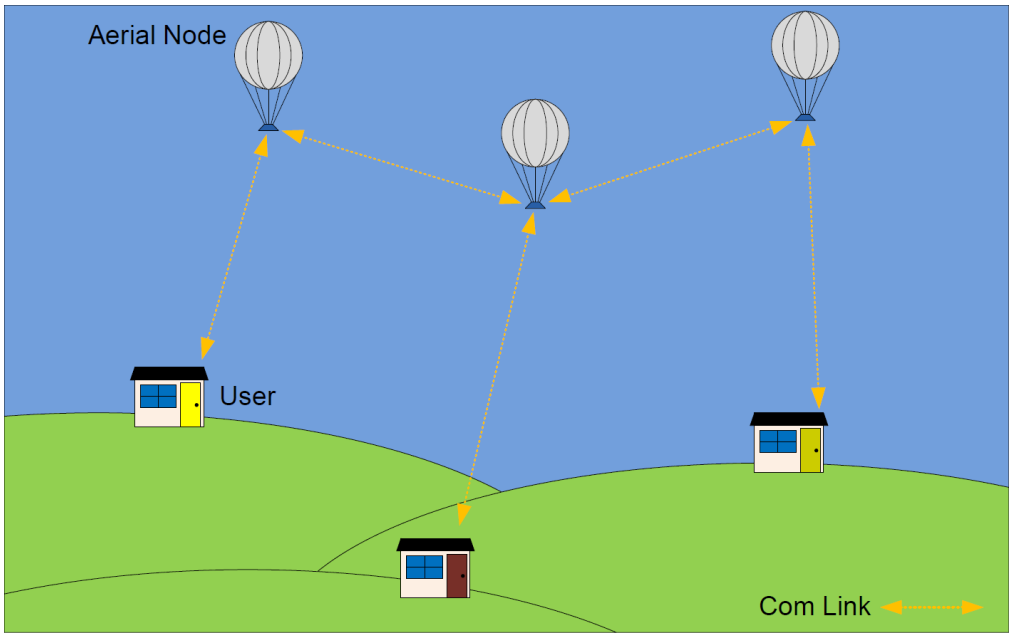

Fig. 4.14 Communication between Aerial Nodes and Ground Based Users

The CP solar antenna discussed in this chapter has potential for use in node to node communication. The antenna size in relation to a weather balloon used in [63] can be seen in Fig. 4.15.

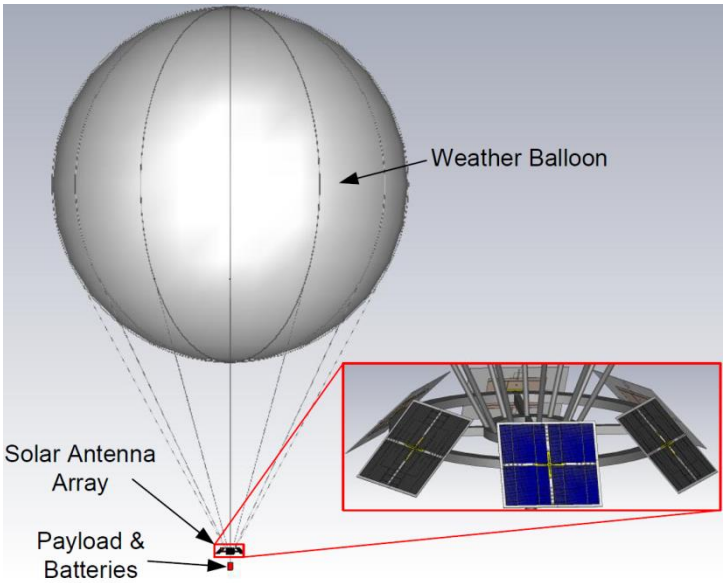

Fig. 4.15 CP Antenna Integrated with Aerial Node

The six antenna arrays rotated 60° apart would provide 360° coverage and allow polarization diversity to improve signal quality between nodes. The solar array would have a

total power output of ~72 W with the possibility to locate additional solar cells between the antenna arrays. As node location data would be held by all nodes it would be possible to reduced power consumption by utilising the most efficient path between nodes rather than transmitting an omnidirectional pattern.

4.7 Conclusion

The integration of four low-profile IFAs, for circular-polarization, with a photovoltaic solar panel is reported. The antennas are located between solar cells in a solar panel and avoid any difficult modification of the solar cells. The configuration ensures 100% solar cell irradiation due to directly facing light sources, while the low profile antenna height minimises shadowing due to oblique angle light sources. The colder temperatures at high altitudes maximise the output power of the high power c-Si solar cells which become less efficient as their temperature rises.

Wider bandwidths compared to antennas above a solid copper ground plane illustrate the effect of increased losses due to the interaction of electric fields with the silicon solar cell. Bandwidths can be further increased with higher antennas.

Beam switching and polarization changing can be achieved by adjusting the phase offset between antenna elements, improving signal strength on mobile platforms whose motion can result in fading of particular polarisations. Larger beamwidths allow the antenna to cover a larger area than other CP integrations increasing the probability of achieving an RF link while maximising solar generation.

5 AMORPHOUS SILICON SOLAR VIVALDI

Wireless devices capable of harvesting energy from their environments are desirable to prolong the life of batteries and reduce maintenance costs [66]. Scavenging solar energy can be cheaply achieved cheaply using a-Si panels with output voltages greater than 3 V as they don't require a lossy boost converter however cell efficiencies around 10% are low.

The level of scavenged power required for wireless sensors continues to drop as MCUs become more efficient. In [67], a wireless temperature sensor tag with an a-Si cell power source was presented. The tag consisted of a 2.43 GHz antenna to receive control commands and an ultra-wideband (UWB) antenna which acted as a backscatterer. The UWB antenna had a load which was adjusted relative to the temperature thus the backscattered signal was modified relative to the measured temperature. The sensor had a range of 150 cm with a current consumption min of 4 µA in standby and a max of 82 µA during calibration. These power requirements can easily be achieved by a-Si solar cells which offer advantages of cheaper production in a compact panelised form yielding readily useable voltages, whereas c-Si cells require additional assembly to achieve desirable voltages and waterproofing.

This chapter will discuss a Vivaldi antenna cut from a panel of a-Si solar cells designed for wireless communications, with complementary solar energy harvesting, or to act as a rectenna for dual-energy harvesting. The slot was located between two strings of solar cells in the panel to minimise the loss of photovoltaic material.

A Vivaldi slot enables a wide bandwidth covering GSM and WLAN bands this facilitating wireless scavenging to complement stored solar energy during hours of darkness and supplement the supply during daylight. Wireless energy scavenging [68] from 0.35 - 3 GHz showed 8 bands that sum to 195 MHz which could support low-power sensor devices. While scavenged power was small [69], low-powered microcontrollers (e.g. 24FJ series PIC) can maintain a deep sleep mode without data loss using 132 nW [70].

5.1 Antenna Configuration

A coplanar Vivaldi antenna was cut from a 0.6 W a-Si panel of ten solar cells arranged in a series of 5 pairs of parallel connected cells, shown in Fig. 5.1 [71]. The 400 nm thick a-Si layer of each cell was 71 × 18 mm and separated from other cells by a 2 mm gap [72]. Each cell had 7 silver electrodes on the front contact. The electrodes are 0.5 × 16.5 mm and separated by 9.5 mm. Rear contacts, 19.9 × 146 mm, provided parallel connections between cells and were isolated from adjacent contacts by a 0.1 mm gap. The low cost flexible panels were manufactured for one of many different power configurations and the layout enabled various antenna shapes. End edge contacts on the panel were made from tin coated copper plate. The entire panel was encapsulated by flexible polymide layer.

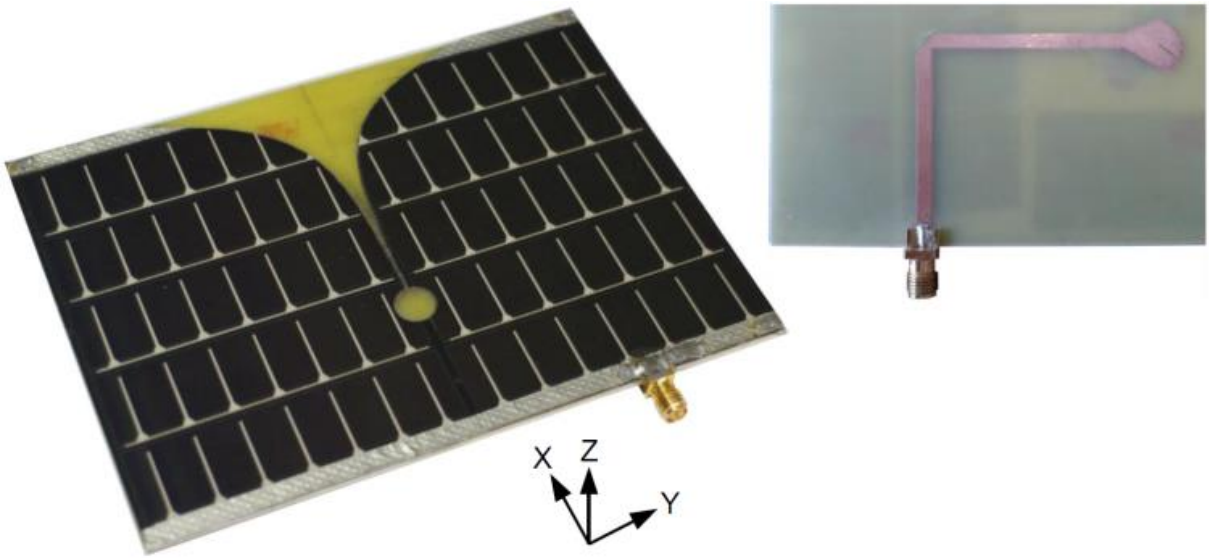

Fig. 5.1 Solar Vivaldi antenna (left) and rear-side transmission line (right)

Equation (1) describes the exponential curve of the Vivaldi antenna where x_0 was the first point of the curve and gr was the rate of change in the curve [73].

$$x = x_0 * exp(gr * t)\ for\ y_{min} < t < y_{max} \qquad (1)$$

The antenna was fed with a 50 Ω microstrip transmission line printed on the FR-4 substrate used to support the solar panel. The transmission line was terminated in a microstrip-to-slot-line transition between a quarter wave radial stub and quarter wave circular

slot. Table 5.1 summarises preliminary simulations with CST Microwave Studio that optimised the stub length to support a band lower than GSM-900 while minimising a circular slot in a copper layer. Having built the simulation model to include the entire solar panel and antenna, final dimensions were optimised for the Vivaldi slot.

Table 5.1 Simulated Microstrip-to-slotline transition results

Stub Length	Lower -10 dB limit (GHz)	Cell Area Removed (%)	S_{11} at		
			0.95 GHz (dB)	1.87 GHz (dB)	2.45 GHz (dB)
10 mm	0.98	2.29	-8.9	-22.4	-10.2
12 mm	0.84	3.49	-16.8	-21.1	-9.8
14 mm	0.74	4.93	-28.4	-17.5	-9.8

The simulated solar Vivaldi antenna was designed with the minimal amount (3.6%) of silicon removed. The slot location was varied to 35 mm from the symmetrical centre between the cells with a loss of 5% of a-Si. While a 5 mm offset had minimal impact, the 35 mm offset reduced the bandwidth by 294 MHz to remove the 900 GSM band. The silicon-optimised features were copied in double-sided copper on an FR-4 substrate for performance benchmark.

5.2 Solar Performance

Solar measurements were carried out using a 1450 Lux light source positioned 960 mm from the solar panel. The solar Vivaldi antenna has been compared to an intact solar panel. The intact solar panel was also supported on an FR-4 substrate to prevent any differences in thermal properties. The outline of the Vivaldi slot is shown imposed on the intact solar panel in Fig. 5.2 with the removed sections of silicon marked in green.

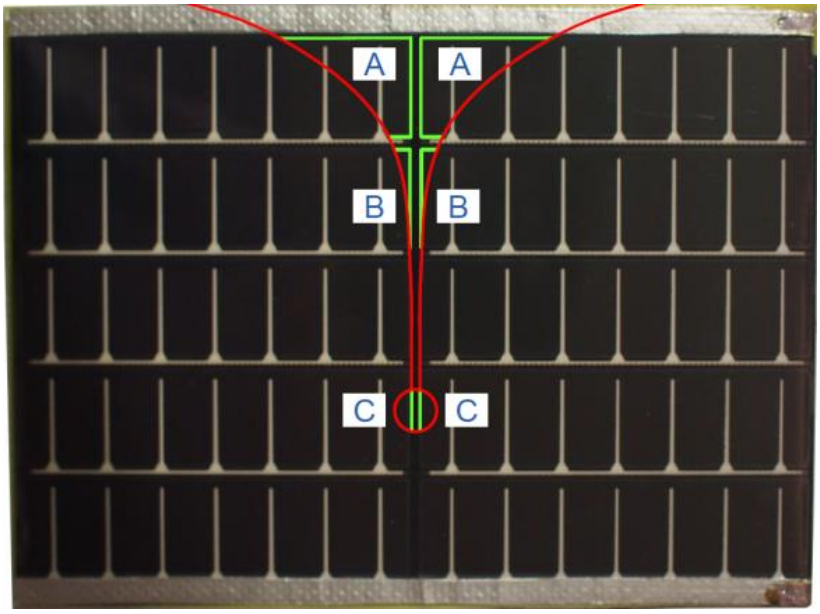

Fig. 5.2 Sections removed from solar cell

As the Vivaldi slot was centred between adjacent solar cells it removes equal amounts of silicon from each cell and splits the panel into two strings of series connected cells. Section A removed 14.40% of the silicon from the affected cell. Section B removed 1.71% and section C was 1.89%. This resulted in a loss of 3.6% of the total available silicon. As section A was the largest cut in a single cell, thereby setting the current limit of that string.

The maximum power point of the full solar cell was 51.7 mW (4.25 V × 12.2 mA). With the strings reconnected, the maximum power point of the solar Vivaldi antenna was 27.4 mW (2.67 V × 10.3 mA). This was a 15.57% decrease in current at the maximum power point which was proportionate with the percentage of material removed. Measured solar power outputs are shown in Fig. 5.3.

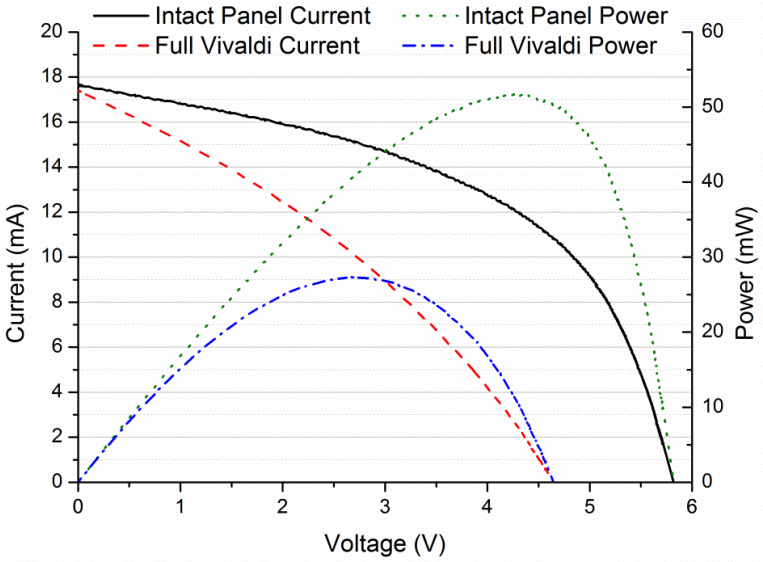

Fig. 5.3 Solar performance results

5.3 Antenna Performance

The S_{11} results, simulated efficiencies and gain data for the measured and simulated antennas are summarised in Table 5.2. Plot comparisons of S_{11} are shown in Fig. 5.4 and a comparison between measured boresight gain for the solar and copper Vivaldis are shown in Fig. 5.5.

Table 5.2 Vivaldi Antenna Performance

Antenna	Min S_{11} (GHz)	Bandwidth (%)	Efficiency			Boresight Gain (dBi)		
			0.95 GHz	1.87 GHz	2.45 GHz	0.95 GHz	1.87 GHz	2.45 GHz
Meas a-Si	0.938	127	N/A	N/A	N/A	0.04	3.91	5.28
Sim a-Si	0.921	123	84%	78%	70%	0.31	4.20	4.52
Meas Cu	0.576	159	N/A	N/A	N/A	1.05	3.84	5.46
Sim Cu	0.752	148	95%	89%	77%	0.92	4.66	5.19

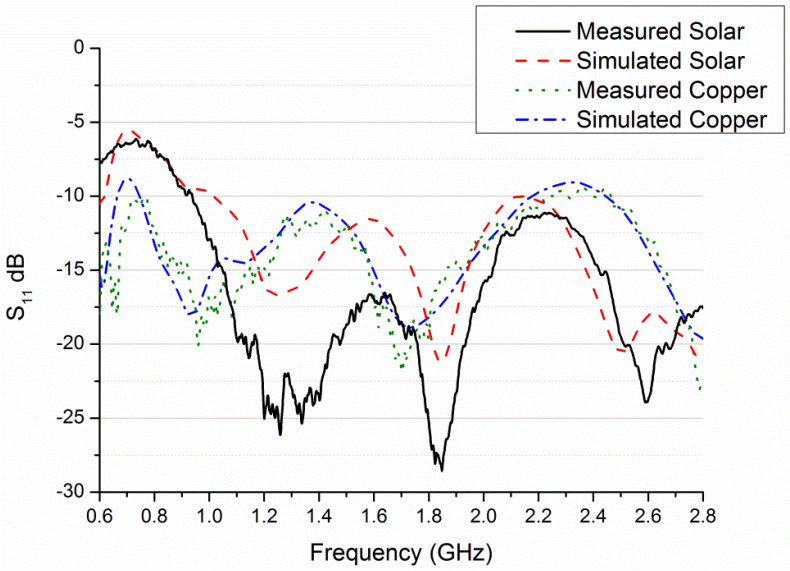

Fig. 5.4 Measured and Simulated S_{11}

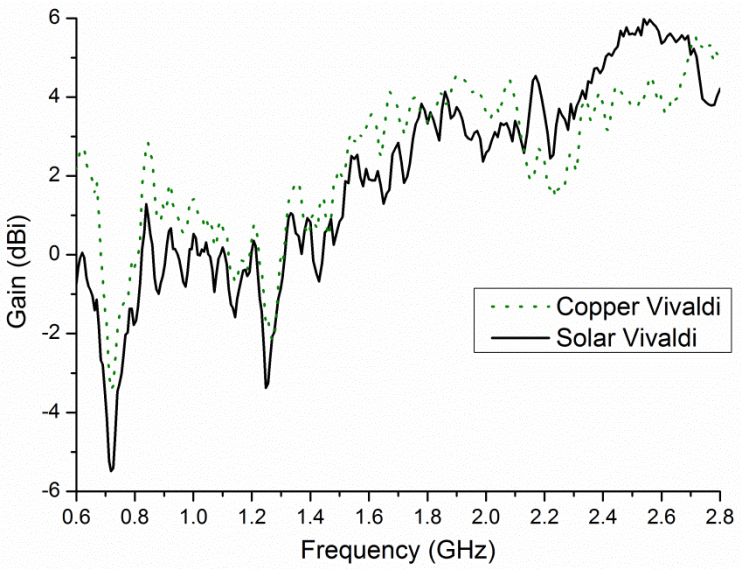

Fig. 5.5 Measured Boresight Gain

The S_{11} response, the efficiency and the gain values are lower for the solar antenna when compared to the copper antenna suggesting increased losses. Simulated results show that some of this loss is due to current flow along the edges of intersections between the solar cells as shown in Fig. 5.6.

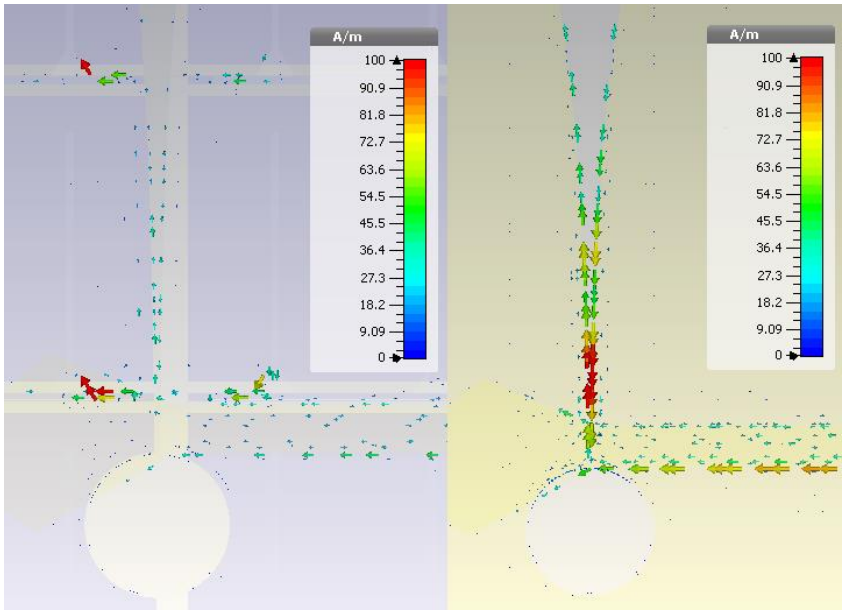

Fig. 5.6 Antenna Surface Currents for Solar (Left) and Copper (Right)

The Vivaldi S_{11} was also measured under various levels of insolation. Measured light intensity was 79 Lux and cell surface temperature was 20°C with the light was off. With the light on for a few seconds, the light intensity was 25300 Lux and the surface temperature was 21°C. After 5 minutes with the light on, the light intensity was 26500 Lux and the surface

temperature was 40°C. The measured S_{11} is shown in Fig. 5.7, no significant variation is observed after the light source is turned on but variation is observed as the cell heats up.

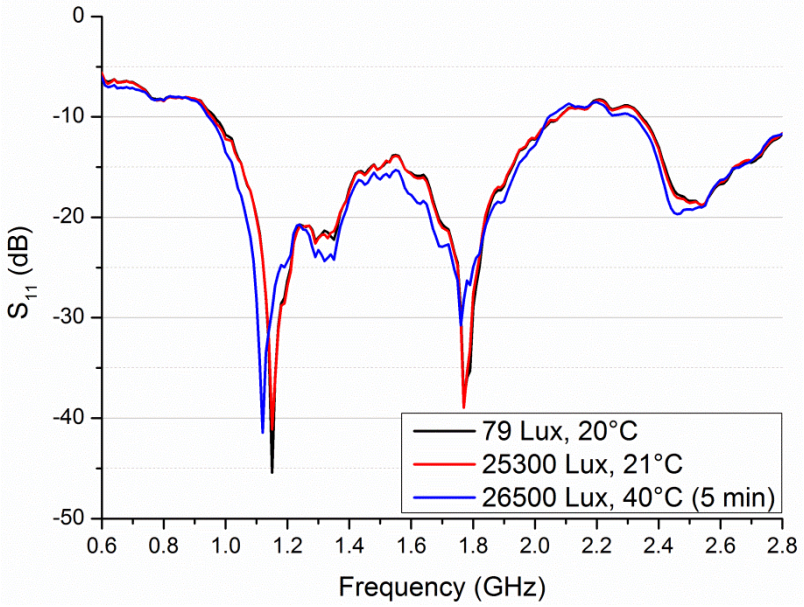

Fig. 5.7 Vivaldi Antenna S_{11} for Different Insolation Levels

The *XZ* beamwidth is narrower than the X-Y beamwidth for all frequencies. In addition the beamwidths narrow as frequency increases with the lower frequency being omnidirectional in the X-Y plane. Radiations plots for the antenna at 950 MHz, 1.87 GHz and 2.45 GHz are shown in Fig. 5.8, Fig. 5.9 and Fig. 5.10 respectively.

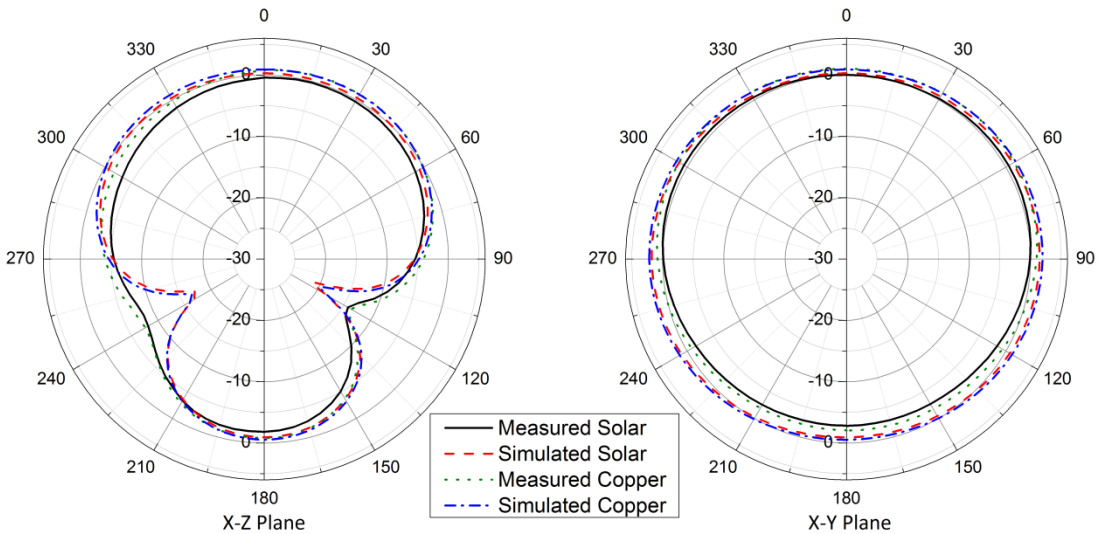

Fig. 5.8 Solar Vivaldi Radiation pattern at 950 MHz

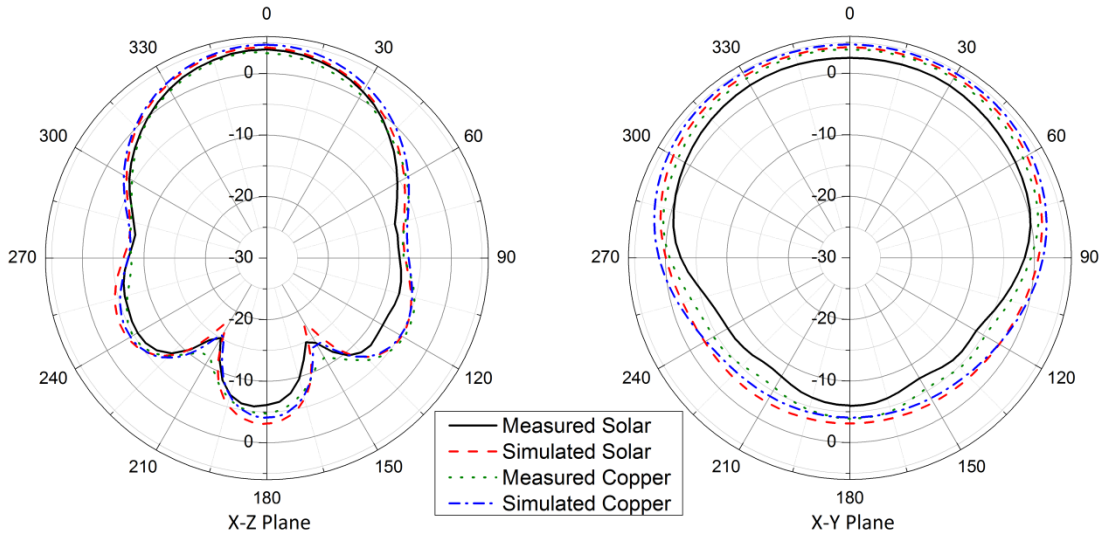

Fig. 5.9 Solar Vivaldi Radiation pattern at 1.87 GHz

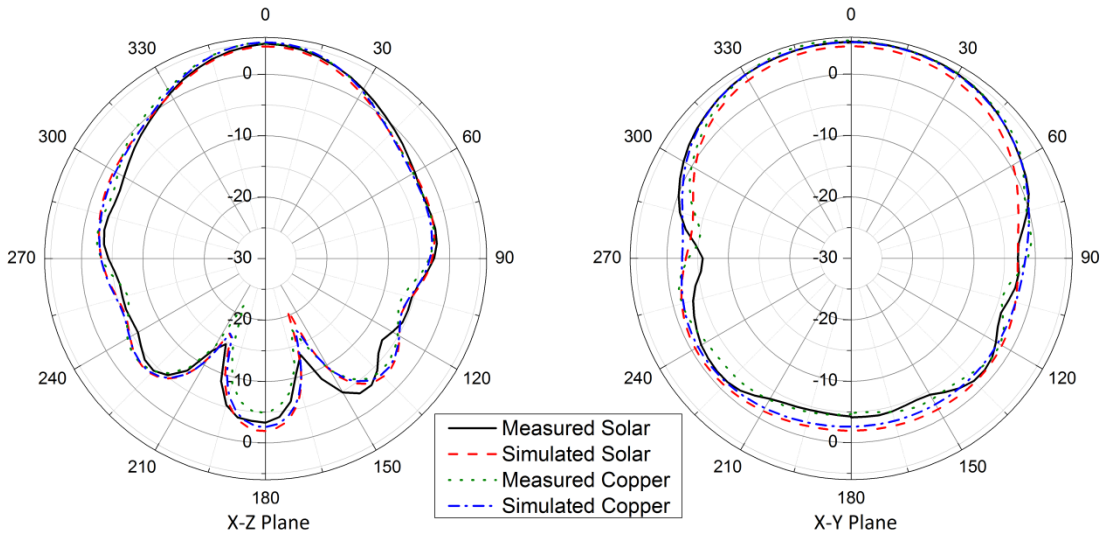

Fig. 5.10 Solar Vivaldi Radiation pattern at 2.45 GHz

5.4 Energy Scavenging Potential

An 8-stage Villard cascade voltage multiplier circuit was designed to test the energy scavenging potential of the solar Vivaldi. The Villard cascade configuration is shown in Fig. 5.11 where the C1 = 100 pF, R1 = 10M Ω and D1is a HSMS-268C-TR1G. A 100 pF storage capacitor and 10M Ω load were chosen to ensure quick charge and discharge during testing.

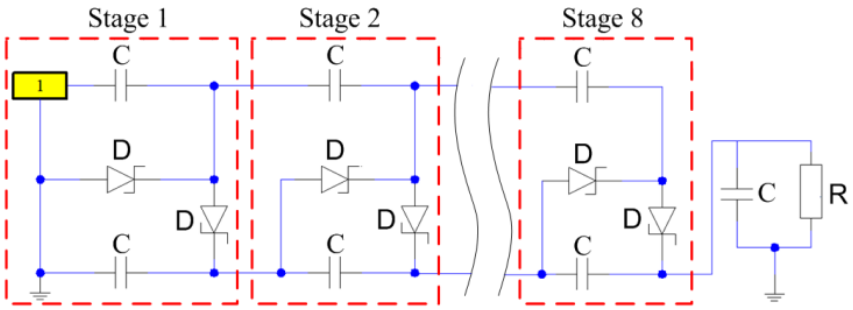

Fig. 5.11 Villard Cascade Voltage Multiplier Circuit

A Hewlett Packard 8648C signal generator with a Mini-Circuits ZFL-2500 31 dB amplifier and a horn antenna located 1 m from the solar Vivaldi was used for testing. The system was measured between the signal generator and the horn, giving a gain of 31 dB at 950 MHz, 32 dB at 1.87 GHz and 31 dB at 2.45 GHz. The horn antenna gain was 9.6 dBi at 950 MHz, 10.8 dBi at 1.87 GHz and 12.4 dBi at 2.45 GHz. The voltage multiplier output was measured in an anechoic chamber to minimise reflection and the inverse-square law was used to calculate the power density (P_D) at the receive antenna, results are shown in Table 5.3. It is clear that with an incident power density of 1.6 µW/cm^2 at 950 MHz, 2.7 µW/cm^2 at 1.87 GHz or 17.4 µW/cm^2 at 2.45 GHz the rectenna can exceed the 1.8 V and 132 nW required for a microcontroller [70] to maintain deep sleep mode.

Table 5.3 Measured DC Output for Different Signal Generator Powers

	-17.5 dBm		-15 dBm		-12.5 dBm		-10 dBm	
Freq (GHz)	P_D (µW/cm^2)	Voltage (V)	P_D (µW/cm^2)	Voltage (V)	P_D (µW/cm^2)	Voltage (V)	P_D (µW/cm^2)	Voltage (V)
0.95	1.6	2.09 V (0.44 µW)	2.9	3.25 V (1.06 µW)	5.1	4.56 V (2.08 µW)	9.1	5.53 V (3.06 µW)
1.87	2.7	2.01 V (0.40 µW)	4.8	2.92 V (0.85 µW)	8.5	3.97 V (1.57 µW)	15.2	4.78 V (2.28 µW)
2.45	3.1	0.83 V (0.06 µW)	5.5	1.27 V (0.16 µW)	9.8	1.73 V (0.30 µW)	17.4	2.06 V (0.42 µW)

5.5 Ideal Solar Vivaldi

If the solar Vivaldi antenna was produced commercially, the solar cell could be redesigned to ensure each cell in the panel had an equal volume of a-Si. In [74], a custom a-Si:H solar cell was manufactured to conform to the shape required for a slot antenna. Laser etching of the solar cell layers in certain patterns make it possible to achieve resonant shapes

without requiring modification to existing production equipment [75]. This would optimize the cells to suit the available space of the solar Vivaldi antenna and improve the output power of the final solar panel.

It is possible to simulate an idealised scenario where the solar Vivaldi has been designed to optimise both solar and RF performance. The DC negative connection between adjacent panels has been restored with the added benefit of providing a continuous metallic strip along the shape of the Vivaldi slot as shown in Fig. 5.12.

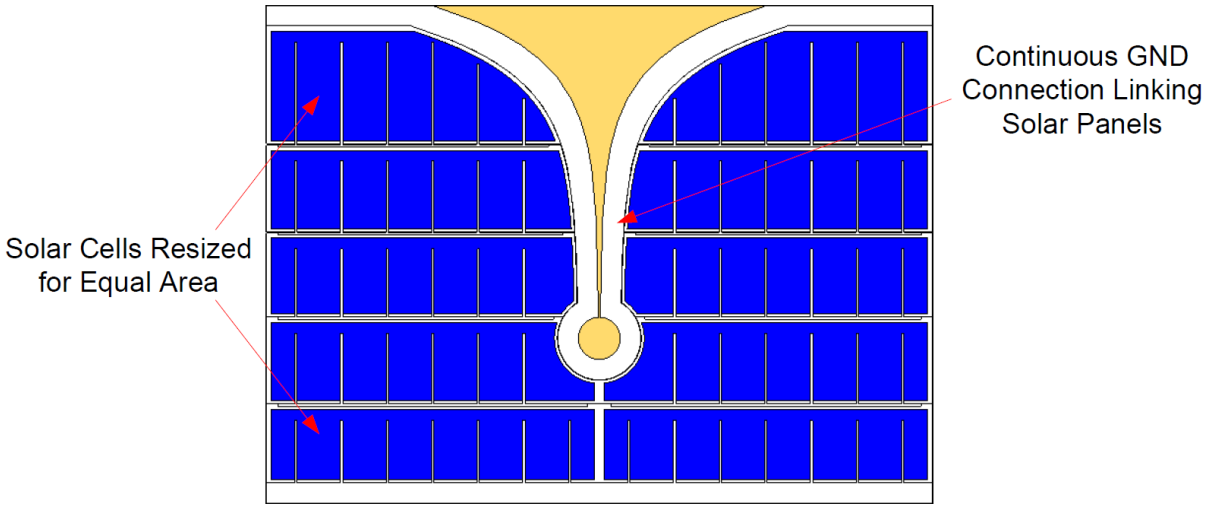

Fig. 5.12 CST Model of Idealised Solar Vivaldi

Each cell now has a surface area of 1090 mm^2 compared to the 1278 mm^2 area of a cell in a conventional solar panel. Interpolating power output based on a-Si surface area estimates a maximum power output of ~0.51 W, 15% lower than a conventional a-Si panel covering the same panel area.

The antenna is resonant from 0.861 GHz with a bandwidth of 125%. S_{11} results are shown in Fig. 5.13 and antenna performance results can be found in Table 5.4. The minimum S_{11}, efficiency and gain values all fall between the values of the copper Vivaldi and the solar Vivaldi discussed in Section 7.1 which would be expected due to the continuous metallic strip along the Vivaldi slot. Fig. 5.14 shows reduced current flow along the cell intersection of the ideal Vivaldi compared to prototype Vivaldi shown in Fig. 5.6.

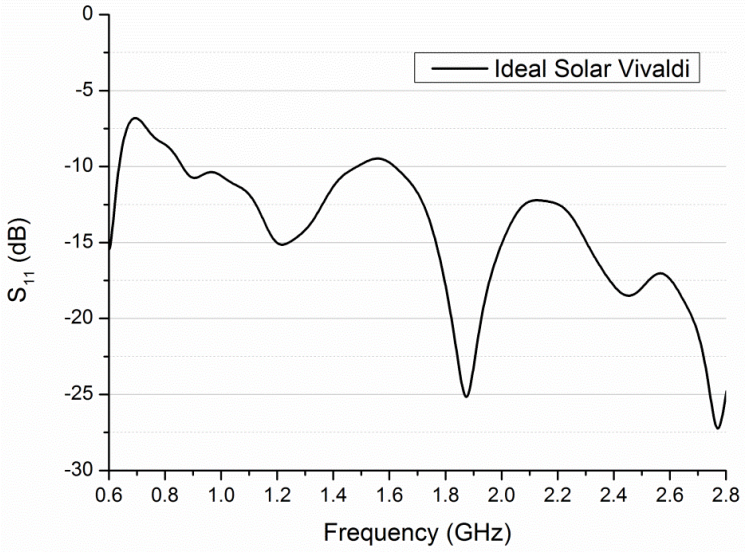

Fig. 5.13 Idealised Solar Vivaldi S_{11} Results

Table 5.4 Ideal Antenna Performance

Frequency	Efficiency	Boresight Gain (dBi)	*XY* Beamwidth	*XZ* Beamwidth
0.95 GHz	87%	0.493	151.7°	360.0°
1.87 GHz	81%	4.277	70.0°	169.7°
2.45 GHz	71%	4.667	51.2°	102.0°

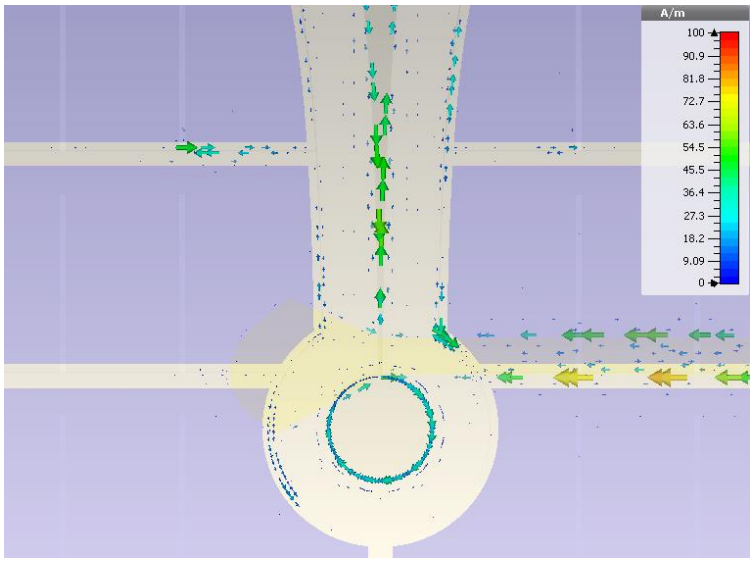

Fig. 5.14 Idealised Solar Vivaldi Surface Currents

As the a-Si solar panels are manufactured in reels there is significant opportunity to cheaply manufacture multi element arrays making it possible to increase the narrow *XY* beamwidth coverage by implementing beam switching. A simulation was carried out in which two solar Vivaldi's are manufactured alongside each other as shown in Fig. 5.15.

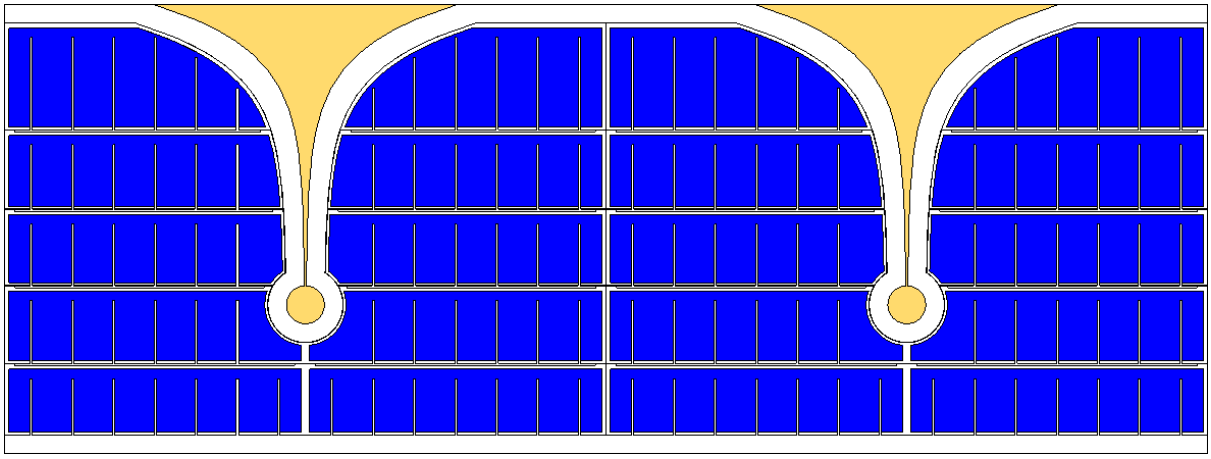

Fig. 5.15 Solar Vivaldi Array Configuration 1

Isolation between the two antennas is better than 10 dB from 0.9 GHz and better than 17 dB from 1.6 GHz, shown in Fig. 5.16.

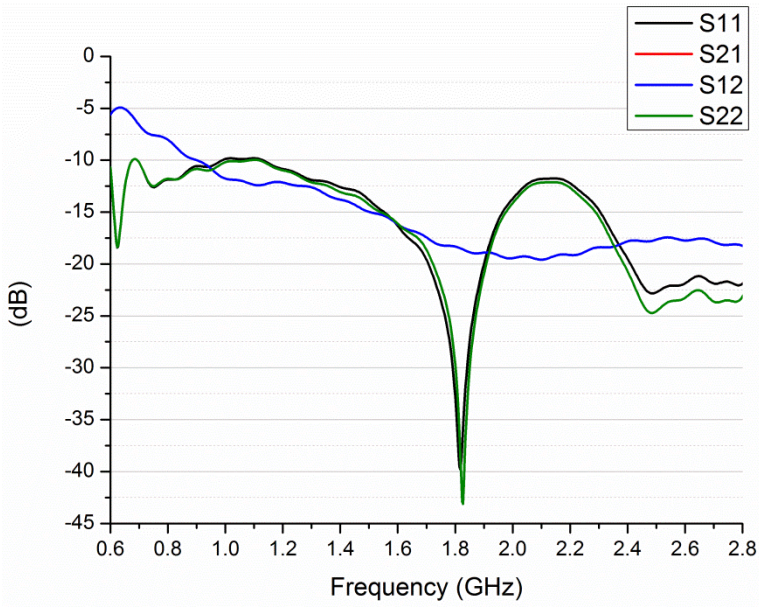

Fig. 5.16 Solar Vivaldi Array Configuration 1 S_{11}

The array has a narrower *XY* beamwidth than the individual antenna however this can be overcome by implementing beam switching, shown in Fig. 5.17, Fig. 5.18 and Fig. 5.19.

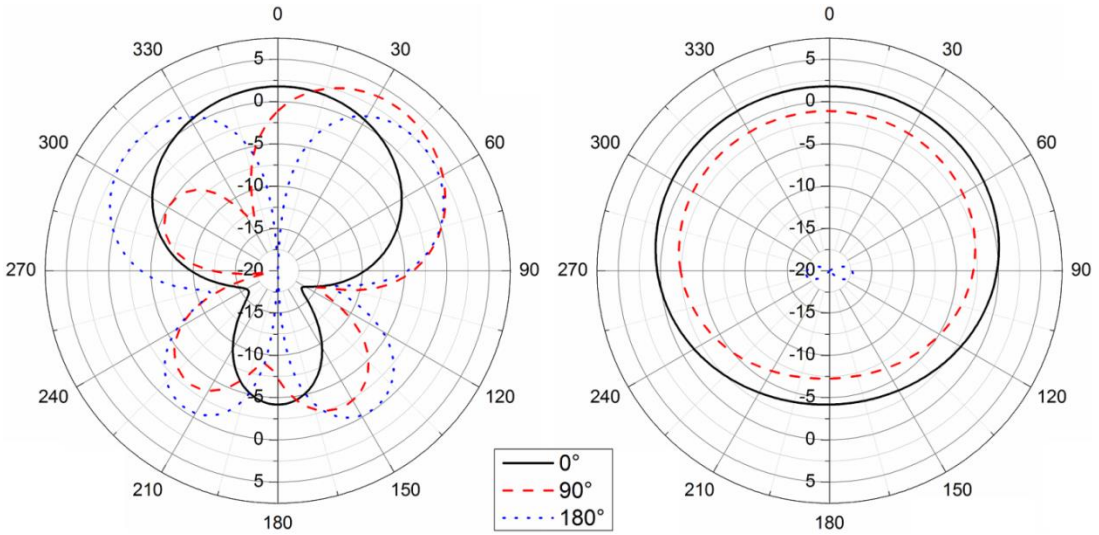

Fig. 5.17 Solar Array Configuration 1Radiation pattern at 950 MHz

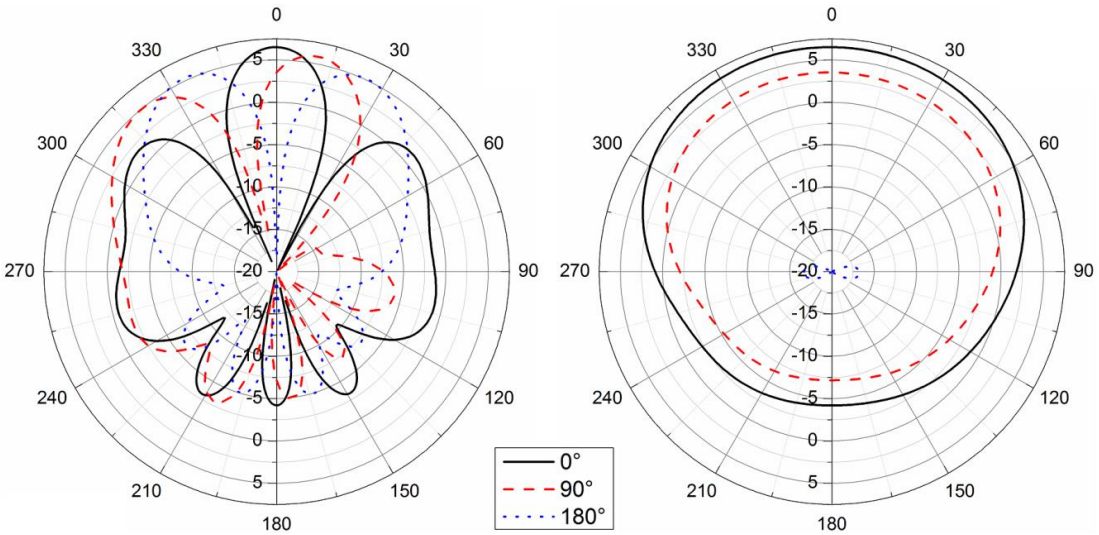

Fig. 5.18 Solar Array Configuration 1Radiation pattern at 1.87 GHz

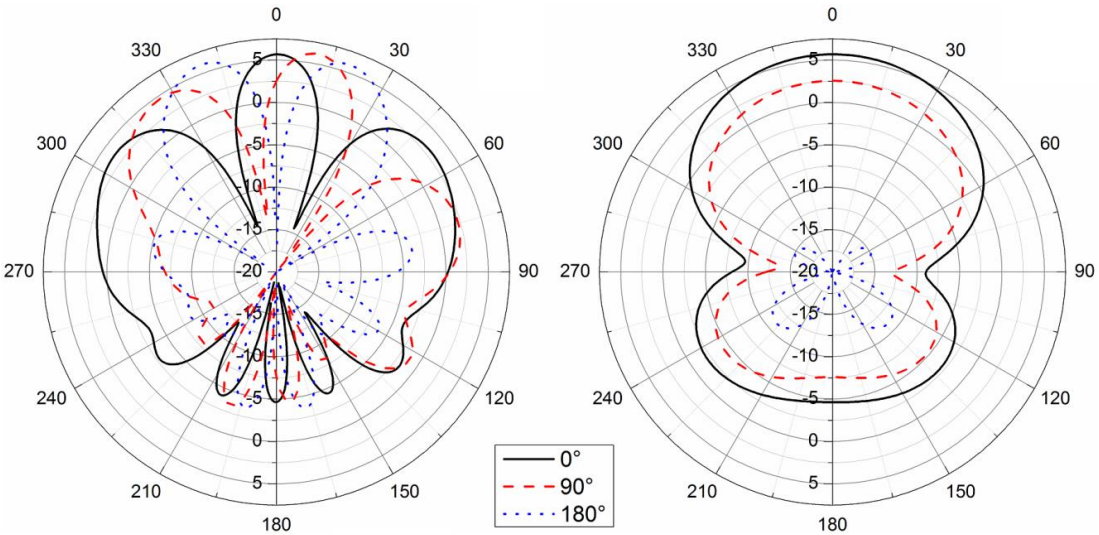

Fig. 5.19 Solar Array Configuration 1Radiation pattern at 2.45 GHz

Antenna spacing within the array can be adjusted by adding additional solar panels between the antennas printed on the reel. A model including one conventional five cell a-Si panel located between two solar Vivaldi's was simulated as shown in Fig. 5.20.

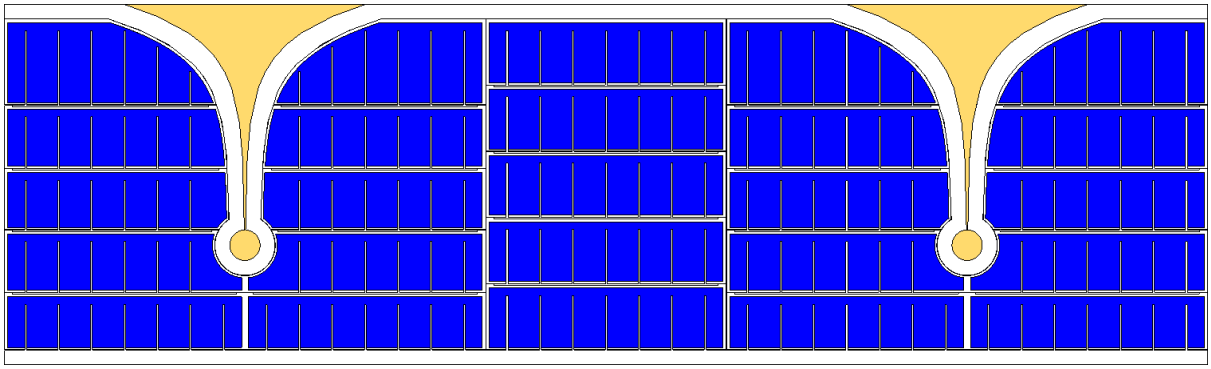

Fig. 5.20 Solar Vivaldi Array Configuration 2

The addition of the extra solar panel increases solar power output to ~1.32 W and improves the isolation by an average of 1.7 dB between 0.6 GHz and 2.8 GHz, shown in Fig. 5.21.

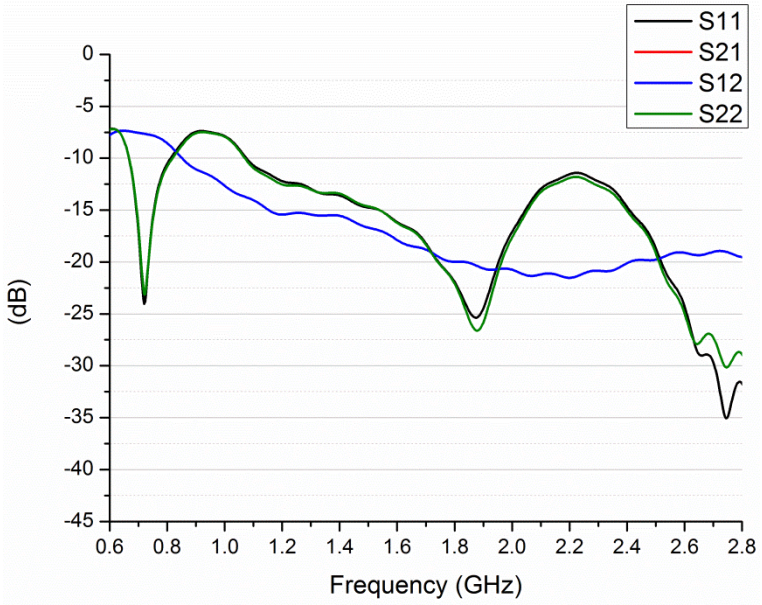

Fig. 5.21 Solar Vivaldi Array Configuration 2 S_{11}

However this also results in narrower main beams and additional side lobes, shown in Fig. 5.22, Fig. 5.23 and Fig. 5.24.

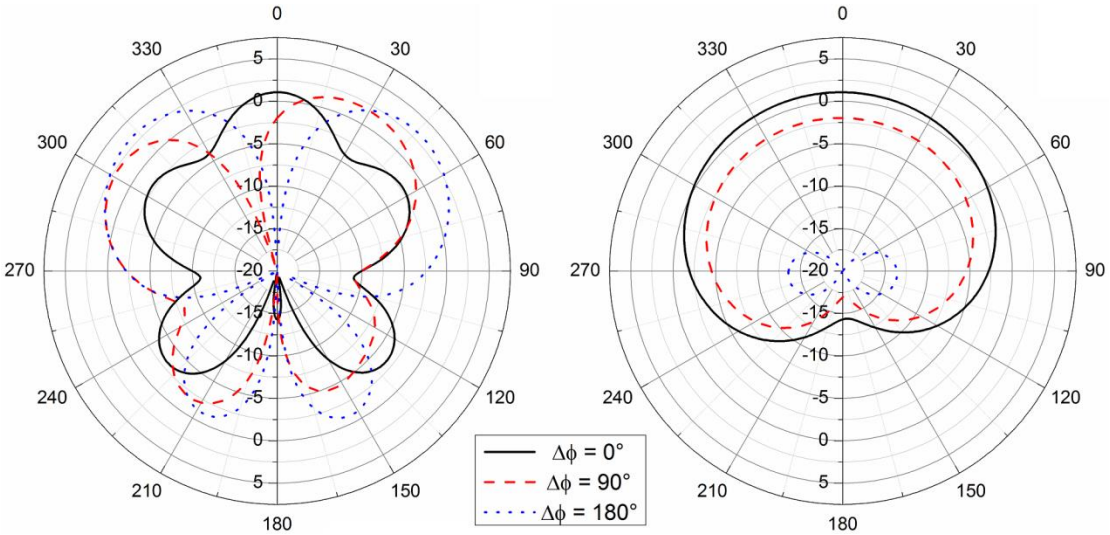

Fig. 5.22 Solar Array Configuration 1Radiation pattern at 950 MHz

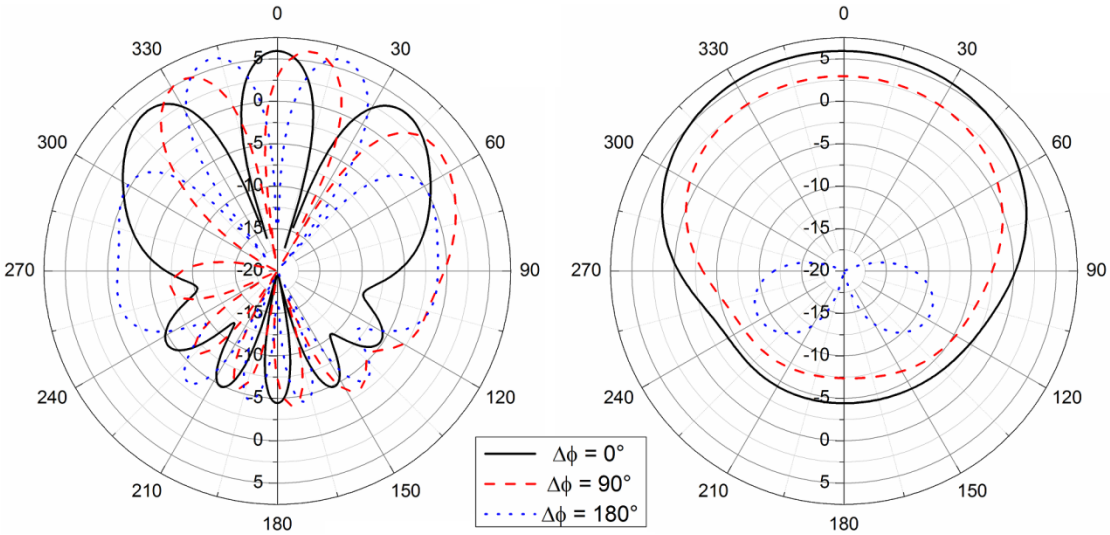

Fig. 5.23 Solar Array Configuration 1Radiation pattern at 1.87 GHz

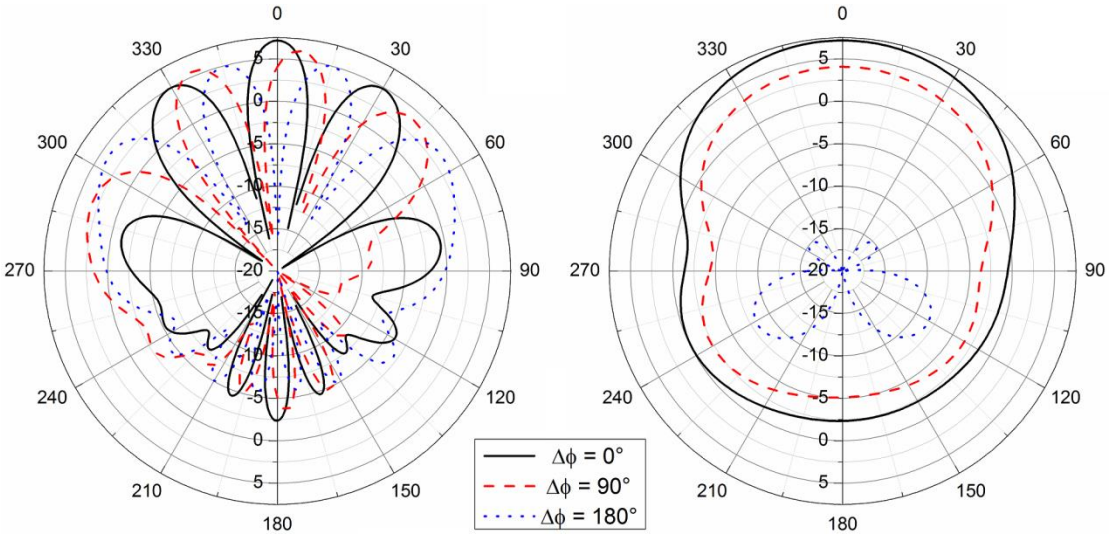

Fig. 5.24 Solar Array Configuration 1Radiation pattern at 2.45 GHz

5.6 Application: Building Sun Shade Integration

Crystalline silicon solar cells are currently used in buildings to create sun shades requiring expensive assembly and glass structures as shown in Fig. 5.25.

Fig. 5.25 Sun Shades incorporating c-Si Solar Cells [76]

Solar Vivaldi arrays could be easily added to existing louvered sun shades commonly found on large commercial and public buildings. Fig. 5.26 shows the extensively louvered facade of Dublin airport with an inset showing the concept of a solar Vivaldi antenna integrated into a large a-Si solar panel located on a louver.

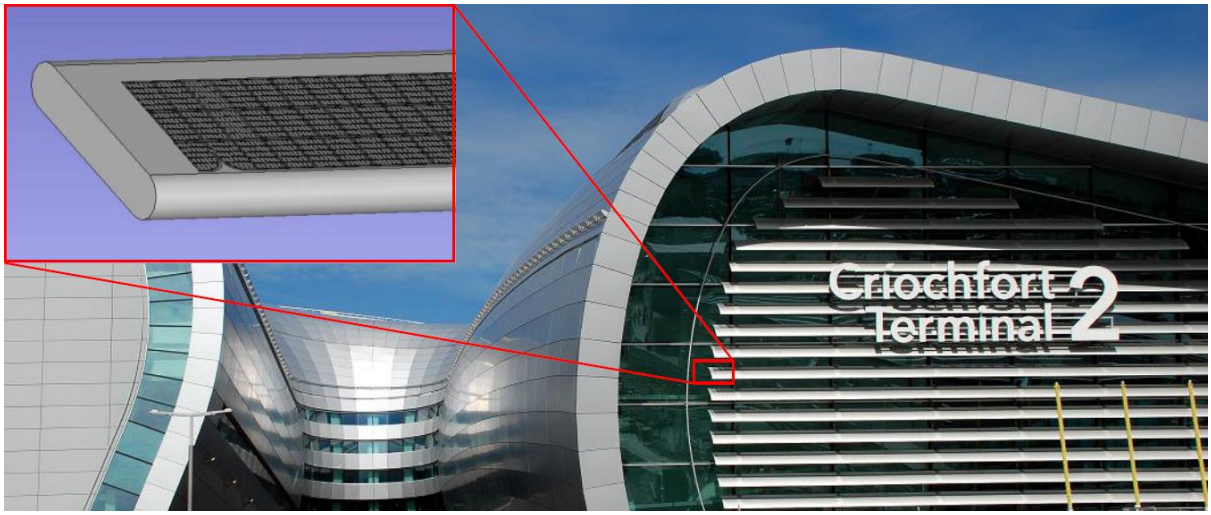

Fig. 5.26 Concept of Installing a-Si Solar Cells on Existing Louvered Facades [77]

5.7 Conclusions

An ultra-wideband (0.938 - 2.45 GHz) Vivaldi antenna was made for the first time from amorphous silicon (a-Si) in order to exploit panelised solar cells that produce readily useable voltages and sufficient power for compact wireless sensors.

The wide bandwidth included GSM and WLAN channels to support remote device locations. The pattern beamwidth exceeded 110º in at least one plane, which was superior to other a-Si solar antennas and enables improved RF transmission, solar generation and wireless energy scavenging consecutively.

Simulated and measured results illustrated how the narrow spacing between the rear aluminium contacts was sufficiently smaller than a wavelength to support stable performance. The antenna feed on the rear of the cell realised current flow predominantly on the larger rear contacts rather than an induced resonance on the more resistive front lattice. This demonstrates that a-Si based solar antennas covering wide bandwidths can be cheaply prototyped from of the shelf cells.

Simulated results reveal that the solar antenna is only 10% less efficient than an equivalent copper antenna and measured gain was 1 dB less at 950 MHz. Increased losses were attributed to the silicon, encapsulating material and current flow at the spaces between cells. The measured gain values are ~1 dB higher than other ultra wideband solar antennas.

Energy scavenging calculations showed the potential to maintain a microcontroller in deep sleep mode while energy is stored for later use.

The removal of a-Si for the Vivaldi slot was limited to 3.6% of the photosensitive section and shows that a Vivaldi design can improve on previous a-Si solar antennas. The 27.4 mW measured maximum power point of the solar Vivaldi was 47% lower than the intact panel but would comfortably power a wireless sensor requiring 55 µW. Manufacture

incorporating a Vivaldi slot and with equal areas of silicon in each cell would easily improve power output thus increasing potential sensor activity. Simulations have shown that an idealised solar Vivaldi would have superior bandwidth, efficiency and gain performance improving range or reducing power requirements for an amplifier.

The a-Si solar panel manufacturing techniques would allow the antennas to be manufactured cheaply into solar array. In addition it has been demonstrated that solar antenna arrays capable of implementing beam switching are also a possibility. This would allow large arrays to be cheaply designed into a structure for example a louvered sunshade on the exterior of a building without presenting a visual pollutant.

6 DYE-SENSITISED SOLAR DIPOLE

Indoor-based silicon (Si) solar cells are outperformed by dye-sensitised (DS) solar cells which have wider acceptance angles and better absorption capacity for diffuse sunlight and fluorescent light [78]. While crystalline Si-cells are more efficient, DS-cells are cheaper to manufacture and can be printed onto flexible conductive plastic layers for device integration. Use indoors mitigates risk of expansion where liquid electrolytes in DS-cells might fracture the packaging in extreme temperatures. Furthermore, it has been shown that power storage capabilities of DS-cells could eliminate the additional need for a battery [79].

The use of DS-cells in antenna design has not been attempted in the literature to date however crystalline and amorphous silicon solar cells have been integrated with dipole antennas. A printed copper dipole on FR-4 substrate was suspended over a 3 W polycrystalline Si-cell ground plane which supported the feed line and acted as an antenna reflector [80]. While it had sufficient power for a wireless sensor, the dipole height above the Si-cell produced a large device volume that was less suited to indoor applications. A folded dipole antenna was constituted with emitter-wrap-through Si-cells, as the radiating elements and a solar concentrator as the reflector [81]. The concentrator contributed to a high 11.1 dBi gain and helped the Si-cell generate 73.7 mW under a 1000 W/m^2 light source. Similarly, the solar antenna had a large device volume due to the reflector and the directive radiation pattern was less suited to indoor applications. An ultra-wideband dipole made from amorphous Si (a-Si) cells covered 3 - 10 GHz [82]. The a-Si antenna had a 0.04 W capacity under a 1000 W/m^2 light source. While the significantly smaller design avoided a large ground plane reflector, a-Si-cells are less efficient than DS-cells.

A challenge while integrating solar cells and antennas is to quantify how various cell materials or metallic properties affect the antenna performance. The orientation of a patch antenna above the anode lattice of a polycrystalline Si-cell was shown to result in differing

levels of exposure to the lossy silicon and to cause a frequency shift and gain reduction [44]. Radiation coupling between a crossed-slot antenna and a panel of a-Si-cells [84] hosted on its ground plane was minimised by optimising the cell area while at the same time, it reduced the solar footprint.

This chapter discusses the first dye-sensitised solar cell antenna which was designed to assess radiating performances where small unobtrusive devices are required. Given that the solar performance does not require metallic lattices, the radiating performance is less sensitive to material proximities and orientation. The radiation pattern, of a dipole in this instance (shown in Fig. 6.1), can be configured to be a toroidal shape while receiving light from opposite sides of the antenna. While a large balun feed was chosen for the proof of concept, a balanced transceiver circuit would connect directly for good performance. The antenna balun provides a series connection between the two solar cells of the dipole.

Three stages of the solar cell were investigated, a dipole made from plain Indium Tin Oxide (ITO) slides, a dipole made from ITO slides with a layer of Titanium Dioxide (TiO_2) and a dipole made from complete solar cells. A copper dipole of identical dimensions is used for comparison.

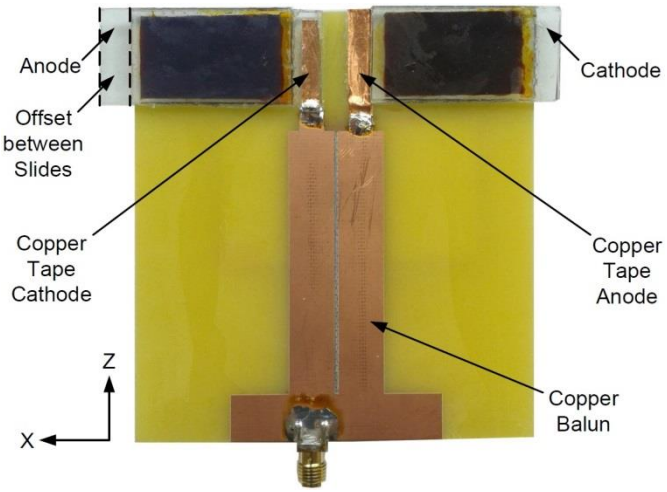

Fig. 6.1 Rear of dye-Sensitised Solar Dipole Antenna

6.1 Dye-Sensitised Solar Cell Manufacture

A dye-sensitised solar cell consists of two transparent electrodes made from glass slides with a thin conductive layer of ITO, shown in Fig. 6.2.

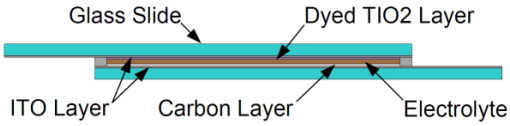

Fig. 6.2 Dye-Sensitised Solar Cell Structure

The manufacturer sintered the Titanium Dioxide to the glass slide by spreading TiO2 paste on one slide and heating it to 450°C for 20 minutes to make an anode, shown in Fig. 6.3.

Fig. 6.3 TiO2 Layer Preparation [85]

TiO2 is not sensitive to visible light so dye molecules were added using Hybiscus dye to allow the TiO2 to absorb energy from visible light, shown in Fig. 6.4.

Fig. 6.4 Sensitising of TiO2 Layer [85]

Pencil lead was used to coat the opposite slide with carbon to make the cathode, shown in Fig. 6.5.

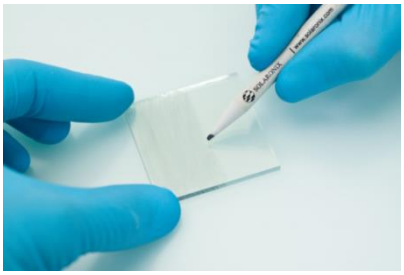

Fig. 6.5 Adding the Carbon Layer [85]

Silicon glue was used to seal three sides between two glass slides while spacing was controlled with temporary shims of 0.4 mm thick acrylic. With the shims removed, an electrolyte for charge transport was poured between the slides and the cell was sealed. Four dye-sensitised solar cells were prototyped.

6.2 Antenna Configuration

The unbalanced feed to balanced dipole was transformed with a microstrip via-hole balun. Provisionally, the balun was λ/4, as were the dye-sensitised solar cells. The final length was optimised using CST Microwave Studio to take account of the electrically-wide DS-cell dipole elements. Balun dimensions are shown in Fig. 6.6, where $W1$ = 5.0 mm, $W2$ = 10.6 mm, $W3$ = 22.5 mm, $W4$ = 1.0 mm, $W5$ = 10.6 mm, $H1$ = 10.0 mm, $H2$ = 56.6 mm and $H3$ = 6.0 mm. Copper tape connected the printed copper balun with the ITO-doped glass. DS-cell material properties are shown in Table 6.1.

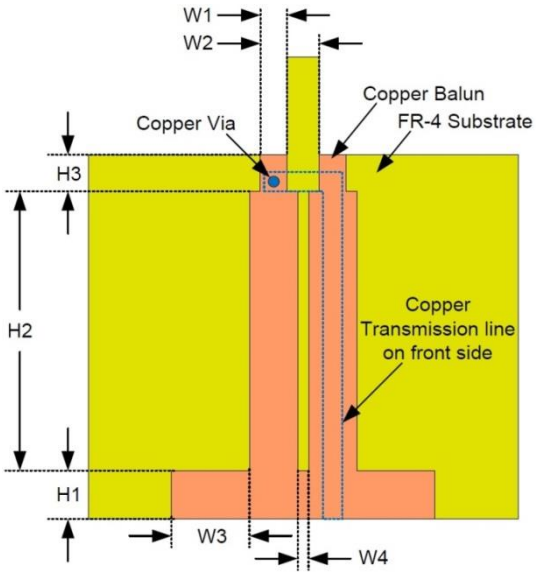

Fig. 6.6 Copper Balun Structure

Table 6.1 Solar Cell Material Properties

Material	Dielectric Constant	Conductivity	Reference
Glass Slide	6.7	N/A	[86]
ITO	N/A	10^{-6} S/m	[87]
TiO_2	85	N/A	[88]
Electrolyte	N/A	3×10^{-4} S/m	[89]
Silicon Sealant	2.8	2.5×10^{-14} S/m	[90]

6.3 Solar Performance

A 1450 Lux tungsten halogen directed light source located 960 mm from the solar cell was used to evaluate output power performance. Table 6.2 shows short-circuit current (I_{sc}) and open circuit voltages (V_{oc}) for various sample DS-cells and the solar-antenna. Each side of the DS-cells were measured facing the light source, when cold and at the 5 minute exposure time. The considerable variance in V_{oc} and I_{sc} between cells was attributed to wider manufacturing tolerances due to limited laboratory equipment. The DS-cells produced the highest power when the TiO_2 face was exposed to the light source. The average carbon face V_{oc} was 18% lower for a cold DS-cell and 32% lower for a cell at the 5 minute exposure. The DS-cells in the antenna were in series so that one TiO_2 face and one carbon face was exposed to the light source simultaneously. Maximum performances for dye-sensitised solar cells are V_{oc} = 0.744 V and I_{sc} = 22.47 mA per cm^2 of photovoltaic material with a 71.2% fill factor [14]. With maximum values the DS-cell dipole would produce ~119 mW, which is adequate power for a Tyndall Mote wireless sensor with an average power consumption of 133 µW [91].

Table 6.2 Measured Solar Cell Results

Solar Cell Under Test	Exposed Face	Cold Cell		After 5 mins exposure	
		V_{oc} (V)	I_{sc} (mA)	V_{oc} (V)	I_{sc} (mA)
Solar Cell 1	TiO_2	0.328	0.055	0.245	0.049
Solar Cell 1	Carbon	0.270	0.015	0.165	0.012
Solar Cell 2	TiO_2	0.351	0.101	0.258	0.091
Solar Cell 2	Carbon	0.285	0.028	0.177	0.020
Solar Cell 3	TiO_2	0.342	0.100	0.251	0.083
Solar Cell 3	Carbon	0.281	0.025	0.166	0.017
Solar Cell 4	TiO_2	0.326	0.050	0.240	0.046
Solar Cell 4	Carbon	0.270	0.014	0.166	0.011
Solar Antenna	Both	0.565	0.034	0.410	0.034
Solar Antenna	Both	0.502	0.035	0.405	0.028

6.4 Antenna Performance

Measured and simulated antenna performance results are summarised in Table 6.3. S_{11} plots are shown in Fig. 6.7. The measured copper dipole was resonant at 1.32 GHz. In order to understand how the various components impact the antenna radiation, various stages were assessed. The plain ITO antenna was resonant at 1.24 GHz due to the high dielectric constant of the glass slide. The addition of high dielectric TiO_2 had minimal impact on the antenna performance since current flow was primarily on the periphery of the glass slide. Introduction of the rear glass slide further lowered the frequency to 1.11 GHz due to *x*-axis offsets of the paired glass slides that were necessary to expose the electrical contacts of the antenna. Additional bandwidth widening was attributed to losses in the rear glass slide.

Table 6.3 Measured and Simulated Antenna Performance

Antenna	Frequency (GHz)	Bandwidth (%)	Efficiency (%)	Boresight Gain (dBi)
Meas Copper	1.32	21.2		1.0
Sim Copper	1.31	23.9	89	1.2
Meas ITO Slide	1.24	26.3		-1.9
Sim ITO Slide	1.21	25.7	41	-1.9
Meas ITO + TiO_2	1.19	24.3		-2.1
Sim ITO + TiO_2	1.21	26.8	42	-1.9
Meas Full Cell	1.11	29.1		-1.5
Sim Full Cell	1.08	27.8	44	-1.5

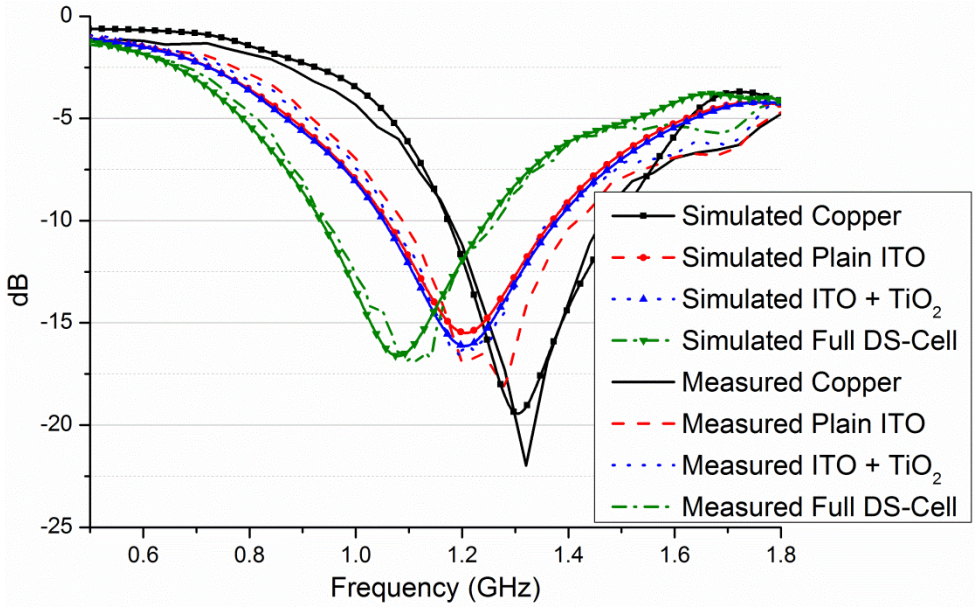

Fig. 6.7 Measured and Simulated S_{11} Results

Simulations assessed the range of material properties of the DS-cell components and are presented in Table 6.4. The plain ITO antenna was used to investigate the dielectric constant of the glass and the conductivity of the ITO layer. Fig. 6.8 (a) showed that the range of ITO conductivity was immaterial to the antenna performance. An increased dielectric constant of the glass lowered the resonant frequency by 7.5 MHz and widened the bandwidth by 6 MHz, as would be expected due increased loss in this material.

Table 6.4 Measured Solar Cell Results

	ITO σ (S/m) × 10^5	Glass ε_r	TiO2 ε_r	Si ε_r	Si σ (S/m) × 10^{-14}	Electrolyte σ (S/m) × 10^{-4}
A	10	6.7	N/A	N/A	N/A	N/A
B	5	6.7	N/A	N/A	N/A	N/A
C	20	6.7	N/A	N/A	N/A	N/A
D	10	4	N/A	N/A	N/A	N/A
E	10	10	N/A	N/A	N/A	N/A
F	10	6.7	85	N/A	N/A	N/A
G	10	6.7	10	N/A	N/A	N/A
H	10	6.7	45	N/A	N/A	N/A
I	10	6.7	85	2.8	2.5	3
J	10	6.7	85	2.3	2.5	3
K	10	6.7	85	3.3	2.5	3
L	10	6.7	85	2.8	1.0	3
M	10	6.7	85	2.8	6.1	3
N	10	6.7	85	2.8	2.5	2
O	10	6.7	85	2.8	2.5	4

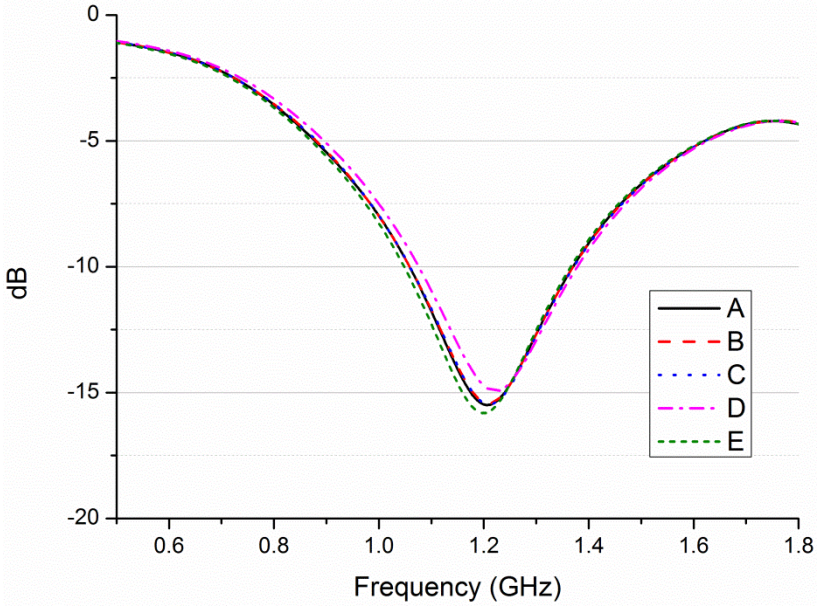

(a) – Reflection Coefficient Variation of ITO Antenna

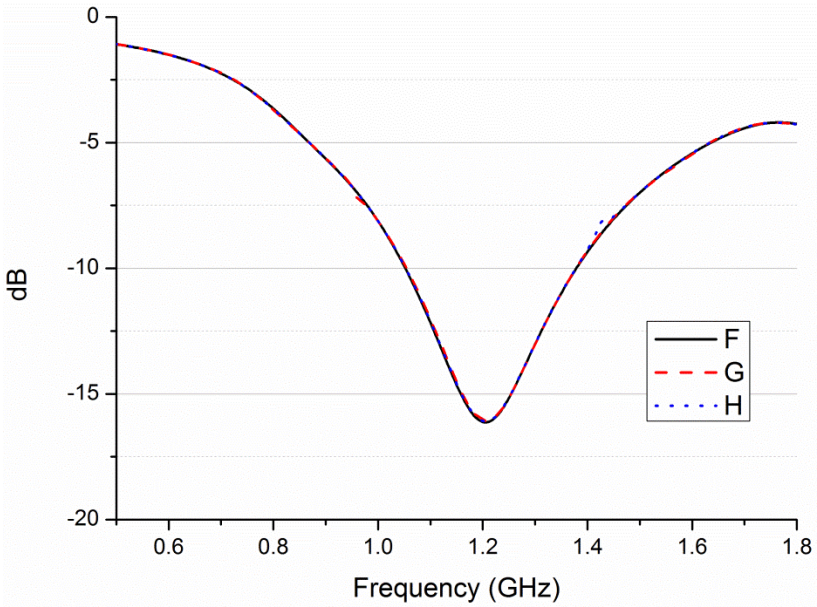

(b) – Reflection Coefficient Variation of ITO + TiO2 Antenna

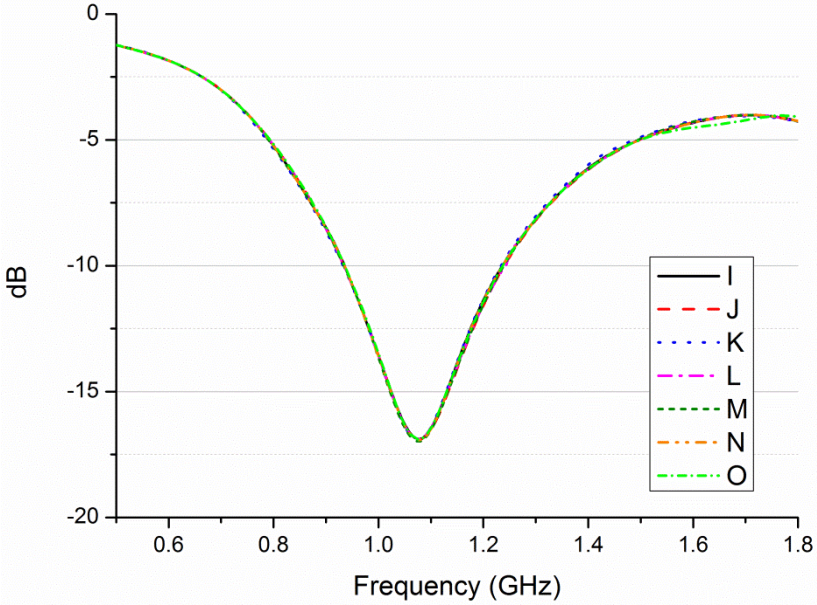

(c) – Reflection Coefficient Variation of Full Solar Antenna

Fig. 6.8 Prototype Dipole Reflection Coefficient Variation

The ITO + TiO_2 antenna assessed the effects of varying the TiO_2 dielectric constant, shown in Fig. 6.8 (b). The TiO_2 layer dielectric constant $10 \leq \varepsilon_r \leq 85$ had no significant impact on the antenna performance since it was outside the main current path.

The full DS-cell antenna assessed the dielectric constant and conductance of the silicon sealant and the conductance of the electrolyte. Fig. 6.8 (c) showed that these materials have minimal impact on the antenna performance. Closer inspection of the surface currents on these material layers revealed that there is very little current flow on the TiO_2 layers,

electrolyte and silicon sealant, shown in Fig. 6.9. This suggests that the two ITO slides couple capacitively. This was confirmed with a simulation of the full DS-cell antenna without these materials. The complete removal of these materials caused a limited downward frequency shift of 5 MHz and a bandwidth reduction of 4.6 MHz.

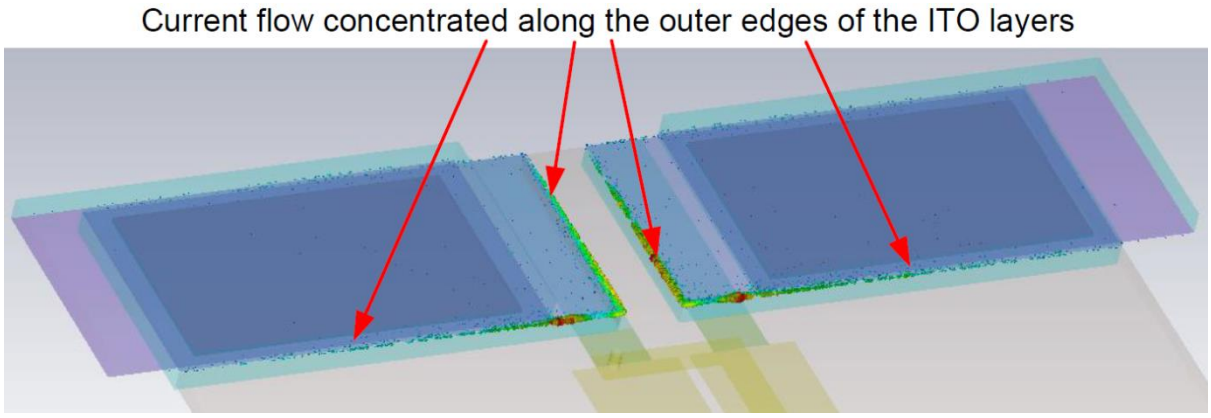

Fig. 6.9 Current Flow on Full Solar Antenna

The DS-cell dipole S_{11} was also measured under various levels of insolation. Measured light intensity was 140 Lux and cell surface temperature was 20°C with the light was off. With the light on for a few seconds, the light intensity was 26900 Lux and the surface temperature was 22°C. After 5 minutes with the light on, the light intensity was 27300 Lux and the surface temperature was 36°C. The measured S_{11} is shown in Fig. 6.10. No significant variation is observed after the light source was turned on or after five minutes exposure to the light source.

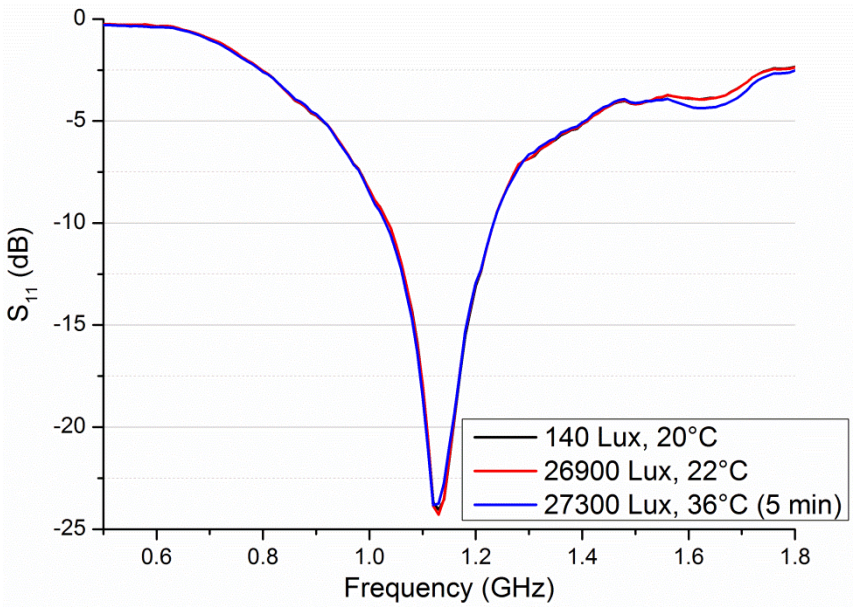

Fig. 6.10 DS-Cell Dipole S_{11} for Different Insolation Levels

There were three potential DS-cell configurations in the completed solar antenna: (a) One TiO_2 slide and one carbon slide connected to the balun; (b) both carbon slides connected to the balun, and (c) both TiO_2 slides connected to the balun. Configuration (a) was manufactured for a higher output voltage and easier power management. Configurations (b) and (c) were simulated and demonstrated insignificant impact on S_{11} and radiation pattern results.

The measured beamwidths for the antenna were 86°, 84°, 89° and 86° for the Copper, ITO, ITO + TiO_2 and complete solar antenna respectively. The measured *YZ* beamwidths for the antenna were 360°, 307°, 308° and 360° for the Copper, ITO, ITO + TiO_2 and complete solar antenna respectively. Large beamwidths are essential for a solar antenna to ensure the antenna can be setup to maximise both solar insolation and the wireless link. Radiations patterns are shown in Fig. 6.11.

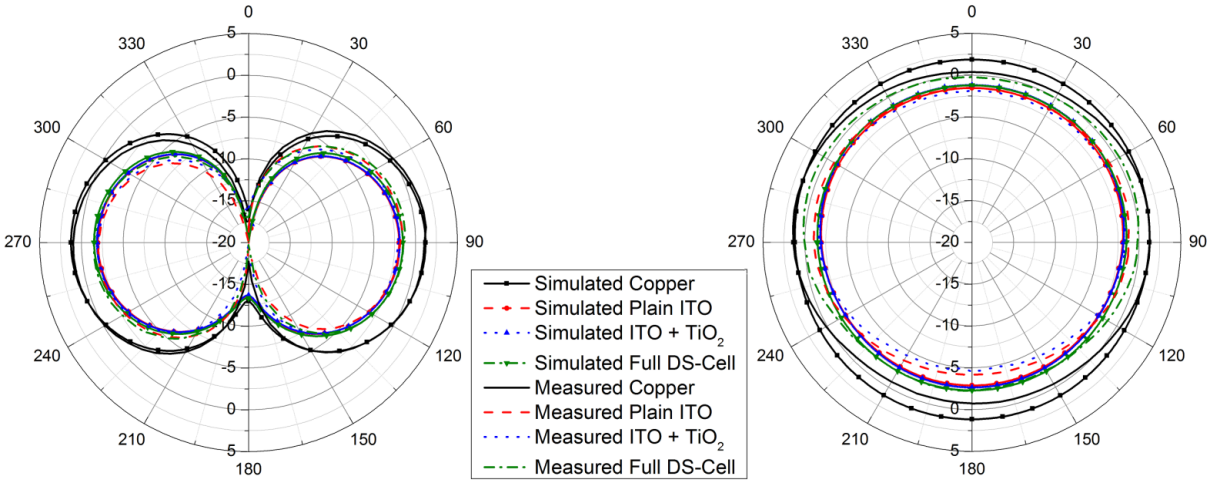

Fig. 6.11 Radiation Pattern *XY* (left) and *YZ* (right)

6.5 Application: Wireless Keyboard

Solar cells that are optimized to absorb indoor ambient light can power small wireless consumer electronic devices such as keyboards [92] or sensors to monitor buildings [93] where costs of wiring installation are avoided. Wireless keyboards can operate on lower than 1.5 V and are used intermittently with a max current of 3 mA during use [94].

Laser ablation allows the antenna structure to be scribed into the ITO layer of a transparent substrate [95]. A dye-sensitised solar bow tie dipole antenna for use in a wireless keyboard can be designed to cover all the Bluetooth channels, simulated S_{11} results are shown in Fig. 6.12.

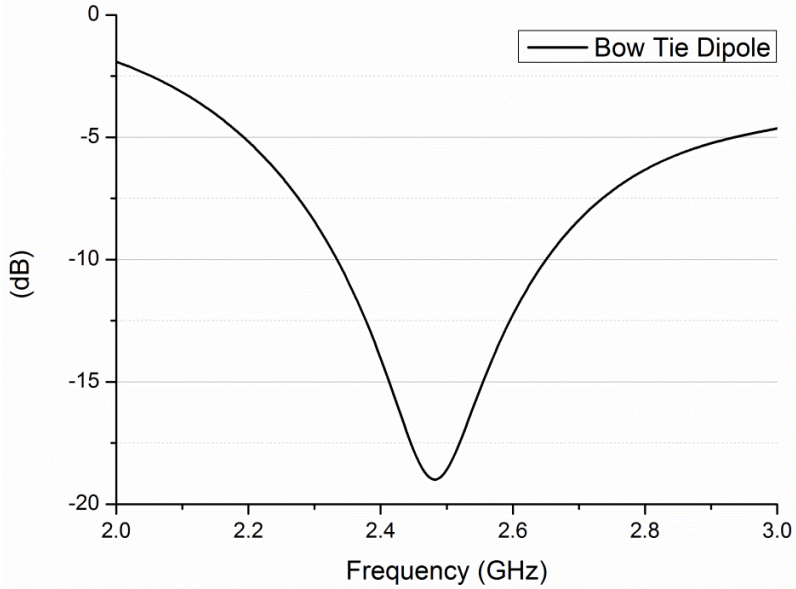

Fig. 6.12 Bow Tie Dipole in Wireless Keyboard S_{11}

Fig. 6.13 shows the unobtrusive antenna structure located above the number pad on a keyboard. A 4×4 mm black plastic square is located above the antenna to represent a QFN20 IC package giving an impression of the space required for a system using a radio transceiver with a balanced output.

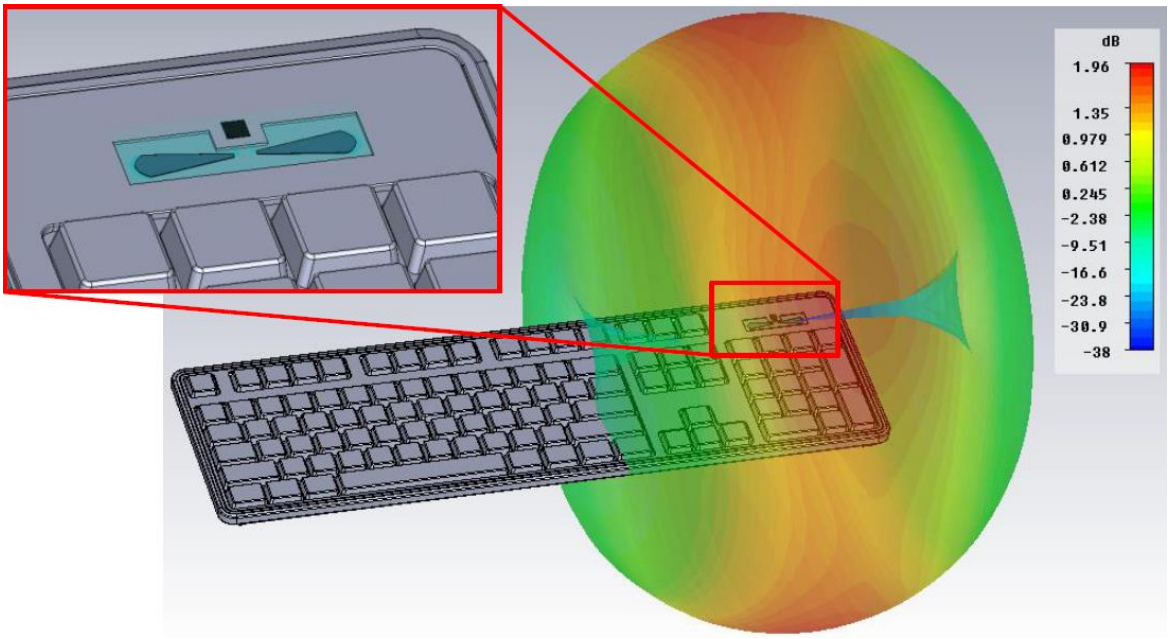

Fig. 6.13 Solar Bow Tie Dipole in Wireless Keyboard

The toroidal radiation pattern increases the chances of achieving a wireless link as the user is most likely to face the device they are controlling but the keyboard may not be on a flat surface. Radiation patterns for the solar bow tie antenna are shown in Fig. 6.14.

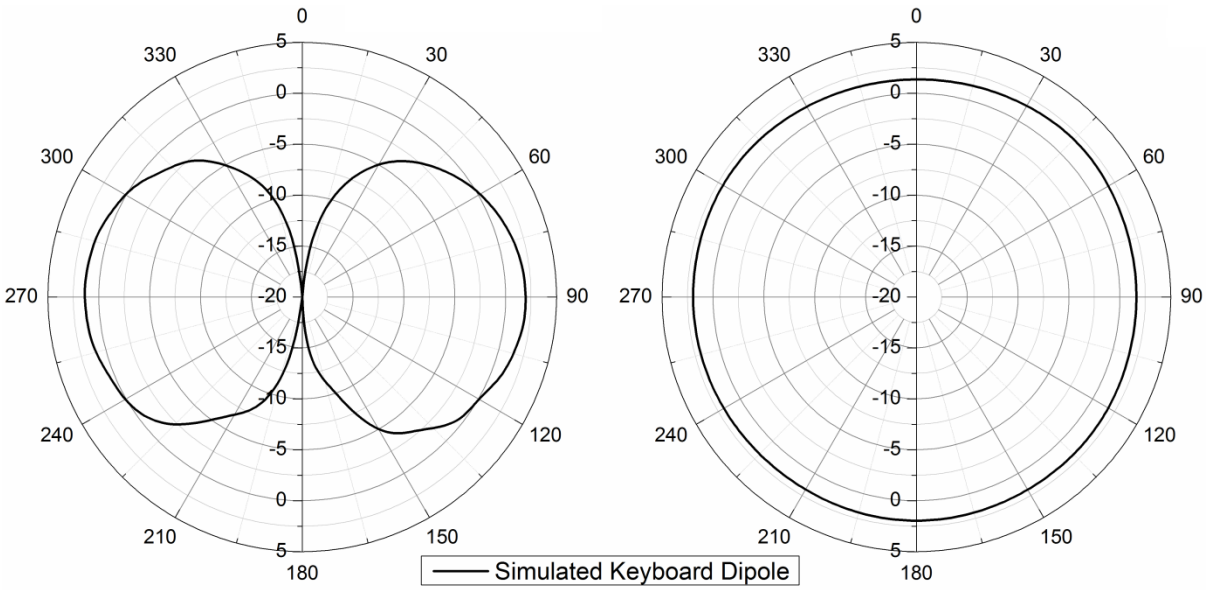

Fig. 6.14 Keyboard Dipole Radiation Pattern *XY* (left) and *YZ* (right)

The bow tie dipole has a photosensitive area 1.04 cm^2 meaning that there is potential to produce 12.37 mW using state of the art dye sensitised solar cell technology, enough to power the device and store energy for later use.

6.6 Conclusions

This chapter reports the first antenna constituted from Dye-Sensitised solar cells. The method enabled increases to solar footprints to support miniaturised wireless sensors for indoor use. The proof of concept dipole configuration examined the antenna performance in terms of the material properties of the solar cell. While the prototype DS-cell antenna had a 19 µW power output limit, Sharp photovoltaics R&D lab could improve the manufacturing process and material properties to yield around a 119 mW output from the same footprint.

The prototype dipole comprised glass packaging and silicon sealant. Simulated models showed that the glass dominated the impact on the antenna performance, while the other solar cell materials had negligible effects. Alternative transparent packing could be selected to reduce complex material losses. The toroidal radiation pattern was not subject to metallic components that are otherwise found on silicon solar cells.

In addition, the ITO and TiO_2 conductive layers and the electrolyte layers could be sintered and packaged into proprietary shapes to facilitate antenna resonance. This would also take account of various feed options and allow for more compact designs. Simulated results have shown that a curved bow tie dipole structure formed from DS-cell materials and sealed between two rectangular glass slides can cover the Bluetooth channels.

7 CONCLUSIONS AND FUTURE WORK

Analysis of potential sustainable energy sources and future finite resource reserves has identified a need for increased energy recovery and scavenging from the environment in future product design with solar energy highlighted as an attractive power source for wireless sensors. Implementing solar cells or panels of solar cells alongside antennas on a device has been identified as a potential area for miniaturisation, where the integration of solar and antenna technologies can reduce weight and the combined surface area. Investigation of prior approaches has highlighted the need for improvements to the reduction of shadowing and the integration with various solar cell types suited to different environments. This work sets out to integrate antennas and solar cells in one compact device to improve their combined performance and reduce overall device size and weight which is crucial for use in aerial vehicles.

The second chapter demonstrated that the introduction of the lattice beneath a transmission line results in a 23% impedance change with a further 10% variation between orthogonal orientations on an asymmetric solar lattice. Simulated results revealed the electric fields to be two orders of magnitude greater between the transmission line and lattice than between the lattice and transmission line in areas where the transmission line crosses the metallisation of the lattice. Similarly it was shown how antenna input impedance is found to vary by 8% with orientation above the lattice which is reduced compared to the transmission line. This chapter laid the ground work for efforts to minimise sensitivity to various orientations.

The third chapter showed the successful implementation of a grounding strip beneath a microstrip transmission line to isolate the transmission line from the electrode lattice of a polycrystalline silicon solar cell. Simulated results indicated reduced orientation sensitivity to 3% variation while avoiding damage to the solar cell or expensive custom cell fabrication.

While the antenna remained slightly sensitive to orientation above the lattice a marked improvement on previous patch antenna designs was proven with measured results. In addition the low profile antenna exposed 9.11% more of the silicon to sunlight and achieved 3.2 dB more gain than previous patch integrations as well as demonstrating the ability to implement beam switching with a dual antenna array.

The fourth chapter minimised solar shadowing on a solar panel with the implementation of four low cost printed IFA antennas located between cells. Measured results demonstrate that the low profile antennas were capable of achieving circular-polarization over a 13.8% axial ratio bandwidth while offering 30% less shadowing than previous meshed patch integrations. In addition, simulated results indicate the ability to implement polarization and pattern reconfiguration which with the high output power would allow this antenna to maintain communication between aerial vehicles which need to rotate during flight.

Measured results for an ultra-wideband Vivaldi antenna prototyped from a flexible a-Si solar panel determined that narrow spacing between cells allowed for a successful radiator over a wide frequency range from 0.938 GHz to 4.21 GHz in the fifth chapter. Simulated results demonstrated that low-cost manufacturing techniques allow the antenna to be designed into an a-Si panel resulting in ~3% higher efficiency, 0.14 dB more gain and a solar output only 15% lower than a complete a-Si panel. Production using sputtering and laser etching allow a-Si solar antennas to be integrated into large panels for installation on a building façade.

The sixth chapter demonstrated a prototype dipole antenna utilising dye sensitised solar cells to form a successful radiator despite the limitations of the glass shape and the manufacturing process. Measured and simulated results established that current flow was predominantly along the outer edge of the ITO layer, minimising the interaction with the

solar cell photosensitive material. Simulated results indicate that designing the antenna shape into the solar cells would improve the RF performance making a suitable antenna for indoor applications.

Each solar integrated antenna has its own potential application both terrestrial and extra-terrestrial depending on its properties which have been identified throughout this thesis. High power outputs of c-Si solar cells make the IFA integrations useful in areas exposed to intermittent light sources meaning the maximum amount of energy can be stored in short periods of time. Alternatively c-Si cells benefit from colder temperatures at high altitudes making them more efficient thus allowing greater power generation for UAVs. The low manufacturing costs and re-configurability of an a-Si solar cell mean that it could easily be produced in large panels for building integration or in a smaller form for handheld or on-body devices. Dye-sensitised solar cells also have potential for small scale consumer electronics due to their greater ability to absorb diffuse sunlight and florescent light indoors. Additionally the colourful dyes make them more aesthetically pleasing than most cells meaning building integration of DSS-cell solar antennas may be more attractive.

It is clear that the range of application for solar antennas is diverse and with the current state of energy reserves there will be increasing demand for consideration of renewable and sustainable energy sources in product design going forward. This thesis has demonstrated the successful integration of a number of solar antenna which could potentially aid a product designer to meet these demands.

7.1 Future Work

Following on the work reported in this thesis, a number of areas for potential advancement in solar antenna research have been identified.

Building on a better understanding of interaction with the solar lattice, it may be possible to develop this knowledge by including the solar cell in the antenna circuit. For example, using the rear contact of the solar cell as ground and connecting the grounding stub of an IFA to the solar lattice. An attempt could then be made to match this system and the effect of light intensity on antenna performance could be analysed.

The integration of c-Si solar cells has been widely documented both in single cell and panelised form, however these solar cells require structural support, glass covering and encapsulation to protect the brittle cells. These features have not been taken account of in prior approaches to date as the focus has been on understanding interaction with the solar cell. It is important to understand how the packaging materials and structure would affect antennas designed into a solar panel. Maintaining current panel dimensions may constrain the antenna design however increasing the dimensions may impact solar performance and would greatly increase cost.

Antennas and transmission lines traversing solar cells cover part of the solar cell reducing solar performance. Substrates manufactured as luminescent solar concentrators may be capable of directing light to the material covered by the metallic layers further increasing solar power generation.

A prototype a-Si based solar antenna that was demonstrated here would benefit from a manufacturing process which incorporated the antenna within an a-Si solar panel. Characterisation of the antenna performance with the additional structural elements required to achieve a manufacturable antenna would be useful. In particular, how the removal of the encapsulating layer from the slot might impact the antenna performance and whether the

additional expense of this extra production step is justifiable. In addition investigating the possibility of integrating a transmission line into the solar cell design could also be investigated.

A prototype dye sensitised solar cell antenna was demonstrated. This antenna was dependant on the shape and metallisation of the glass slides used to make the antenna. Further research into designing the antenna structure into the solar cell would improve understanding of dye-sensitised solar antennas. Additionally the use of platinum instead of carbon, plastic instead of glass, different dyes and different transparent conductors could be investigated to assess the potential degradation or improvement of antenna performance with the introduction of these materials.

8 REFERENCES

[1] Stockholm Environment Institute, "The SEI Initiative on Fossil Fuels and Climate Change," 2015. [Online]. Available: http://www.sei-international.org/mediamanager/documents/Publications/Climate/SEI-FS-2015-Fossil-fuels-climate-mitigation-initiative.pdf. [Accessed 21 Sept. 2015].

[2] Solar Impulse, "Exploraton to change the world," [Online]. Available: http://www.solarimpulse.com/. [Accessed 12 Aug. 2015].

[3] B. Sarlioglu, C. T. Morris, "More Electric Aircraft: Review, Challenges and Opportunities for Commercial Transport Aircraft," *IEEE Transactions on Transportation Electriffication,* vol. 1, no. 1, pp. 54-64, 2015.

[4] B. Lee, S. Kwon, P. Park, K. Kim, "Active Power Management System for an Unmanned Aerial Vehicle Powered by Solar Cells, a Fuel Cell and Batteries," *IEEE Transactions on Aerospace and Electronic Systems,* vol. 50, no. 4, pp. 3167-3177, 2014.

[5] H. Inoue, "Introduction of PC200-8 Hybrid Hydraulic Excavators," Komatsu, 2008. [Online]. Available: http://www.komatsu.com/CompanyInfo/profile/report/pdf/161-E-05.pdf. [Accessed 21 Sept. 2015].

[6] J.A. Paradiso, T. Starner, "Energy Scavenging for Mobile and Wireless Electronics," *IEEE Pervasive Computing,* vol. 4, no. 1, pp. 18-27, 2005.

[7] F. Cain, "What Kind of Star is the Sun?," Universe Today, 1 Aug. 2008. [Online]. Available: http://www.universetoday.com/16350/what-kind-of-star-is-the-sun/. [Accessed 12 Aug. 2015].

[8] U. Eicker, Solar Technologies for Buildings, West Sussex, England: John Wiley & Sons Ltd, 2003.

[9] D. M. Chapin, C. S. Fuller, G. L. Pearson, "A New Silicon p-n Junction Photocell for Converting Solar Radiation into Electrical Power," *Journal of Applied Physics,* vol. 25, no. 5,

p. 676–677, 1954.

[10] Helmholtz-Zentrum Berlin, "The silicon baseline," [Online]. Available: https://www.helmholtz-berlin.de/projects/pvcomb/forschen/silizium/index_en.html. [Accessed 12 Aug. 2015].

[11] J. L. Pankove, Hydrogenated Amorphous Silicon: Device applications, Orlando, Florida: Academic Press Inc., 1984.

[12] R. D. Rocha et al, "EPFL Quartier Nord, SwissTech Convention Center, Ecublens," March 2014. [Online]. Available: http://divisare.com/projects/260236-Richter-Dahl-Rocha-Associe-s-architectes-EPFL-Quartier-Nord-SwissTech-Convention-Center-Ecublens/print. [Accessed 12 Aug. 2015].

[13] D. Wei, "Dye Sensitized Solar Cells," *International Journal of Molecular Sciences,* vol. 11, no. 3, pp. 1103-1113, 2010.

[14] M.A. Green, K. Emery, Y. Hishikawa, W. Warta, E.D. Dunlop, "Solar cell efficiency tables (version 46)," *Progress in Photovoltaics: Research and Applications,* vol. 23, no. 7, pp. 805-812, 2014.

[15] National Renewable Energy Laboratory, "Best-Research Cell Efficiencies," [Online]. Available: http://www.nrel.gov/ncpv/images/efficiency_chart.jpg. [Accessed 12 Aug. 2015].

[16] S. Honda, T. Minemoto, M. Aritake, T. Haruta, H. Takakura, Y. Hamakawa, "Tilt angle and monthly dependence of the output power in an 80 kWp hybrid PV system installed at Shiga in Japan," *Proceedings of 3rd World Conference on Photovoltaic Energy Conversion,* vol. 3, pp. 2247-2250, 2003.

[17] "IEEE Standard Definitions of Terms for Antennas," *IEEE Std 145-1983,* pp. 1-31, 1983.

[18] H. Yongtai, L. Lihui, L. Yanqiu, "Design of solar photovoltaic micro-power supply for application of wireless sensor nodes in complex illumination environments," *IET Wireless*

Sensor Systems, vol. 2, pp. 16-21, 2012.

[19] H. C. Chu, W. T. Siao, W. T. Wu, S. C. Huang, "Design and Implementation an Energy-aware Routing Mechanism for Solar Wireless Sensor Networks," *IEEE High Performance Computing and Communications Conference*, pp. 881-886, 2011.

[20] B. Fountain, "Battery Maintenance and Monitoring - What's Real and What's Not? (More Reliability for the Dollar)," Verizon Wireless, [Online]. Available: http://www.battcon.com/PapersFinal2003/FountainPaperFINAL2003.pdf. [Accessed 21 Sept. 2015].

[21] A. Georgiadis, A. Collado, S. Kim, H. Lee, M.M. Tentzeris, "UHF Solar Powered Active Oscillator Antenna on Low Cost Flexible Substrate for Wireless Identification Applications," in *IEEE MTT-S International Microwave Symposium Digest (MTT)*, 2012.

[22] T. Maleszka, P. Gorski, P. Kabacik, "On Omnidirectional coverage with minimum nuber of circularly polarized patch antenna placed on minisatellites," *Antennas and Propagation Society International Symposium*, pp. 3037-3040, 2007.

[23] M. Z. J. Huang, "Antennas Integrated with Solar Arrays for Space Vehicle Applications," in *5th Intl Symp on Antennas Propag. & EM Theory*, Beijing, China, 2000.

[24] T. Wu, R. Li, M. M. Tentzeris, "A Scalable Solar Antenna for Autonomous Integrated Wireless Sensor Nodes," *IEEE Antennas and Wireless Propagation Letters*, vol. 10, pp. 510-513, 2011.

[25] S. V. Shynu, M. J. Roos Ons, G. Ruvio, M. J. Ammann, S. McCormack, B. Norton, "A Microstrip Printed Dipole Solar Antenna using Polycrystalline Silicon Solar Cells," in *IEEE AP-S International Symposium on Antenna and Propogation*, 2008.

[26] O. Yurduseven, D. Smith, N. Pearsall, I. Forbes, F. Bobor-Oyibo, "A Solar Parabolic Reflector Antenna Design for Digital Satellite Communication Systems," in *IET International Symposium on Communication Systems, Networks And Digital Signal*

Processing, Poznan, 2012.

[27] T. Yasin, R.Baktur, "Circularly Polarized Meshed Patch Antenna for Small Satellite Application," *IEEE Antenna and Wireless Propagation Letters*, vol. 12, pp. 1057-1060, 2013.

[28] O. Yurduseven, D. Smith, "A Solar Cell Stacked Multi-Slot Quad-Band PIFA for GSM, WLAN and WiMAX Networks," *IEEE Microwave & Wireless Component Letters,* vol. 23, no. 6, pp. 285 - 287, 2013.

[29] N. Henze, M. Weitz, P. Hofmann, C. Bendel, J. Kirchhof, H. Fruchting, "Investigation of Planar Antennas with Photovoltaic Solar Cells for Mobile Communications," in *IEEE International Symposium on Personal Indoor and Mobile Radio Communications*, 2004.

[30] M. Danesh, J. R. Long, "An Autonomous Wireless Sensor Node Incorporating a Solar Cell Antenna for Energy Harvesting," *IEEE Transactions on Microwave Theory and Techniques,* vol. 59, pp. 3546-3555, 2011.

[31] M. J. Roo Ons, Shynu Nair, M. J. Ammann, S. McCormack, B. Norton, "On Surface Currents in a Polycrystalline Solar Cell Acting as Ground Plane for Microstrip Patch Antennas," in *IEEE International Antennas & Propagation Symposium*, San Diego, CA, 2008.

[32] T. W. Turpin, "Meshed Patch Antennas Integrated On Solar Cell - A Feasibility Study And Optimization," Utah State University, 2008. [Online]. Available: http://www.ece.usu.edu/grad/reports_theses_disseratations/2008/turpin_timothy_w/thesis.pdf. [Accessed 21 Sept. 2015].

[33] S.V. Shynu, M.J. Ammann, S.J. McCormack, B. Norton, "Emitter-wrap-through photovoltaic dipole antenna with solar concentrator," *Electronic Letters*, vol. 45, no. 5, pp. 241-242, 2009.

[34] M. Danesh, J.R. Long, "Solar cell antenna for autonomous wireless smart sensors," in *Smart Systems Integration (SSI)*, Dresden, Germany, 2011.

[35] S. V. Shynu, M. J. Roo Ons, M. J. Ammann, S. McCormack, B. Norton, "Dual Band a-Si:H

Solar-Slot Antenna for 2.4/5.2GHz WLAN Applications," in *3rd European Conference on Antennas & Propagation*, 2009.

[36] M. Danesh, J. R. Long, "Photovoltaic Antennas for Autonomous Wireless Systems," *IEEE Transactions on Circuits and Systems,* vol. 58, pp. 807-811, 2011.

[37] S. Vaccaro, P. Torres, J. R. Mosig, A. Shah, J. F. Zurcher, A. K. Skrivervik, P. de Maagt, L. Gerlach, "Stainless steel slot antenna with integrated solar cells," *Electronic Letters,* vol. 36, no. 25, pp. 2059-2060, 2000.

[38] GOM Space, "NanoCom ANT430 70 cm band antenna Datasheet, Release 1.1," 2012. [Online]. Available: http://gomspace.com/documents/GS-DS-NANOCOM-ANT.pdf. [Accessed 21 Sept. 2015].

[39] Amazon, "Amazon Prime Air," [Online]. Available: http://www.amazon.com/b?node=8037720011. [Accessed 12 Aug. 2015].

[40] M. O. Jonassen, "The Small Unmanned Meteorological Observer (SUMO)," University of Bergen Geophysical Institute, 2008. [Online]. Available: http://www.uib.no/filearchive/master_jonassen.pdf. [Accessed 21 Sept. 2015].

[41] W. Y. Toh, Y. K. Tan, W. S. Koh, L. Siek, "Autonomous Wearable Sensor Nodes With Flexible Energy Harvesting," *IEEE Sensors Journal,* vol. 14, no. 7, pp. 2299-2306, 2014.

[42] Z. Fan, Z. Jiang, S. Shen, D. Ding and R. Chen, "Meshed Ground Microstrip Antennas with Low Radar Cross Section," in *Electrical Design of Advanced Packaging and Systems Symposium (EDAPS)*, 2011.

[43] Y. Lin, T. Wu, "Investigation of Signal Quality and Radiated Emission of Microstrip Line on Imperfect Ground Plane: FDTD Analysis and Measurement," in *IEEE International Symposium on Electromagnetic Compatibility*, 2001.

[44] S.V. Shynu, M.J. Roo Ons, P. McEvoy, M.J. Ammann, S.J. McCormack, B. Norton,

"Integration of Microstrip Patch Antenna with Polycrystalline Silicon Solar Cell," *IEEE Trans Antennas and Propagation,* vol. 57, no. 12, pp. 3969-3972, 2009.

[45] M. J. R. Ons, "Integration of Antennas and Solar Cells for Autonomous Communication Systems," PhD Thesis, Dublin Institute of Technology, Dublin, 2010.

[46] D. Liu, B. Gaucher, "The Inverted-F Antenna Height Effects on Bandwidth," *IEEE Antenna and Propagation Society International Symposium,* vol. 2A, pp. 367-370, 2005.

[47] C. M. Su and K. L. Wong, "Narrow flat-plate antenna for 2.4GHz WLAN operation," *Electronic Letters,* vol. 39, no. 4, pp. 344-345, 2003.

[48] D. Liu and B. Gaucher, "Performance Analysis of Inverted-F and Slot Antennas for WLAN Applications," *IEEE Antenna and Propagation Society International Symposium,* vol. 2, pp. 14-17, 2003.

[49] L. Pazin, N. Telzhensky, Y. Leviatan, "Wideband flat-plate inverted-F laptop antenna for Wi-Fi/WiMAX operation," *IET Microwaves, Antennas & Propagation,* vol. 2, pp. 568-573, 2008.

[50] Y. S. Yang, M. C. Lee, S. J. Chung,, "Two PIFA-Related Miniaturized Dual-Band Antennas," *IEEE Transaction on Antennas and Propagation,* vol. 55, pp. 805-811, 2007.

[51] S.V. Shynu, M.J. Roo Ons, P. McEvoy, M.J. Ammann, S.J. McCormack, B. Norton, "Integration of Microstrip Patch Antenna with Polycrystalline Silicon Solar Cell," *IEEE Transactions on Antennas and Propagation,* vol. 57, no. 12, pp. 3969-3972, 2009.

[52] "Thanet Earth Discovery Zone," Thanet Earth, [Online]. Available: http://www.thanetearth.com/. [Accessed 17 July 2015].

[53] D. LaGesse, "Supercapacitors Amp Up as an Alternative to Batteries," National Geopgraphic, 23 Aug 2013. [Online]. Available: http://news.nationalgeographic.com. [Accessed 17 July 2015].

[54] Microchip, “MCP9700/9700A Low-Power Linear Active Thermistor™ ICs,” 2009.

[55] G. S. Korea, “Specification of Humidity Sensor Unit, HU1030NA,” 2010.

[56] Vernier, “Soil Moisture Sensor,” 2012.

[57] “APDS-9300 Miniature Ambient Light Photo Sensor with Digital (I2C) Output,” Avago Technologies, 2008. [Online]. Available: http://docs.avagotech.com/docs/AV02-1077EN. [Accessed 21 Sept. 2015].

[58] J. Seo, “Overcoming Ionospheric Scintillation for Worldwide Gps Aviation,” PhD Thesis, Stanford University, Stanford, Ca, 2010.

[59] R.K. Crane, “Ionospheric Scintillation,” *Proceedings of the IEEE*, vol. 65, no. 2, pp. 180-199, 1977.

[60] T. Yasin, R. Baktur, “Circularly Polarized Meshed Patch Antenna for Small Satellite Application,” *IEEE Antennas and Wireless Propagation Letters*, vol. 12, pp. 1057-1060, 2013.

[61] M. Chandak, R. Baktur, “Circularly polarized slot antenna with a simple feed design for solar cell integration,” in *IEEE Antennas and Propagation Society International Symposium (APSURSI)*, 2012.

[62] S. Vaccaro, J.R. Mosig, P. de Maagt, “Two advanced solar antenna "SOLANT" designs for satellite and terrestrial communications,” *IEEE Transactions on Antennas and Propagation*, vol. 51, no. 8, pp. 2028-2034, 2003.

[63] “Project Loon,” Google, [Online]. Available: http://www.google.com/loon/. [Accessed 12 Dec. 2014].

[64] “Prospects for Commercial Stratospheric Industrialisation at the Threshold of Space,” athenalab.com, 16 Oct. 2010. [Online]. Available: http://www.athenalab.com/Prospects_for_commercial_stratospheric_industrialization.pdf.

[Accessed 15 Dec. 2014].

[65] A. Vilhar, A. Hrovat, T. Javornik, M. Mohorčič, "Experimental Analysis of Wireless Temporary Networks Deployed by Low Altitude Platforms," in *IEEE 18th International Workshop on Computer Aided Modelling and Design of Communication Links and Networks (CAMAD)*, 2013.

[66] J.A. Paradiso, T. Starner, "Energy Scavenging for Mobile and Wireless Electronics," *IEEE Pervasive Computing*, vol. 4, no. 1, pp. 18-27, 2005.

[67] M. Danesh, J.R. Long, "An autonomous wireless sensor node using a solar cell antenna for solar energy harvesting," *IEEE MTT-S International*, 2011.

[68] J. Tavares, N. Barroca, H.M. Saraiva, L.M. Borges, F.J. Fernando, C. Loss, R. Salvado, P. Pinho, R. Goncalves, N. Borges Carvalho, "Spectrum opportunities for electromagnetic energy harvesting from 350 mhz to 3 ghz," *7th International Symposium on Medical Information and Communication Technology (ISMICT)*, pp. 126-130, 2013.

[69] H.J. Visser, AC.F. Reniers, J.AC. Theeuwes, "Ambient RF Energy Scavenging: GSM and WLAN Power Density Measurements," *38th European Microwave Conference*, pp. 721-724, 2008.

[70] Microchip Technology Inc., "Microchip Device Document, 64/80/100-Pin, General Purpose, 16-Bit Flash Microcontrollers with LCD Controller and nanoWatt XLP Technology," 2010. [Online]. Available: http://ww1.microchip.com/downloads/en/DeviceDoc/39996f.pdf. [Accessed 21 Step. 2015].

[71] PowerFilm Solar Inc., "PowerFilm Solar OEM Flysheet, OEM Components," 2008. [Online]. Available: http://www.cdiweb.com/datasheets/powerfilm/PowerFilm%20OEM%20Components.pdf. [Accessed 21 Sept. 2015].

[72] J. Kang, "Structural Integration of Silicon Solar Cells and Lithium-ion Batteries Using

Printed Electronics," University of California, 2012. [Online]. Available: http://escholarship.org/uc/item/6kp7k07f#page-1. [Accessed 21 Sept. 2015].

[73] D. Gaetano, A. Dumoulin, M.J. Ammann, P. McEvoy, "Conformal UWB impulse antenna for pipe telemetry," in *Loughborough Antennas and Propagation Conference (LAPC),* Loughborough, 2011.

[74] S. Vaccaro, J.R. Mosig, P. de Maagt, "Two Advanced Solar Antenna "SOLANT" Designs for Satellite and Terrestrial Communicaions," *IEEE Transactions on Antennas and Propagation,* vol. 51, no. 8, pp. 2028-2034, 2003.

[75] S. Nakano, T. Matsuoka, S. Kiyama, H. Kawata, N. Nakamura, Y. Nakashima, S. Tsuda, H. Nishiwaki, M. Ohnishi, I. Nagaoka, Y. Kuwano, "Laser Patterning Method for Integrated Type a-Si Solar Cell Submodules," *Japanese Journal of Applied Physics,* vol. 25, no. 12, pp. 1936-1943, 1986.

[76] solarpv.co.uk, ""Solar PV - Solar PV Louvres - Solar PV Sun Shades," [Online]. Available: http://www.solarpv.co.uk/solar-pv-louvres.html. [Accessed 6 July 2015].

[77] Dublin Airport Authority, "Securing The Future, The DAA's Strategic Plan 2010-2014," 2010. [Online]. Available: https://www.daa.ie/Libraries/Presentations_and_speeches_2011/The_DAA_s_Strategic_Plan_2010-2014.sflb.ashx. [Accessed 21 Sept. 2015].

[78] D. Wei, "Dye Sensitized Solar Cells," *International Journal of Molecular Sciences,* vol. 11, no. 3, pp. 1103-1113, 2010.

[79] T. Miyasaka, T.N. Murakami, "The photocapacitor: An efficient self-charging capacitor for direct storage of solar energy," *Applied Physics Letters,* vol. 85, no. 17, pp. 3932-3934, 2004.

[80] S.V. Shynu, M.J. Roo Ons, G. Ruvio, M.J. Ammann, S. McCormack, B. Norton, "A microstrip printed dipole solar antenna using polycrystalline silicon solar cells," in *Antennas and Propagation Society International Symposium,* 2008.

[81] S.V. Shynu, M.J. Ammann, S.J. McCormack, B. Norton, “Emitter-wrap-through photovoltaic dipole antenna with solar concentrator,” *Electronic Letters,* vol. 45, no. 5, pp. 241-242, 2009.

[82] M. Danesh, J. R. Long, “Photovoltaic Antennas for Autonomous Wireless Systems,” *IEEE Transactions on Circuits and Systems,* vol. 58, pp. 807-811, 2011.

[83] S.V. Shynu, M.J. Roo Ons, P. McEvoy, M.J. Ammann, S.J. McCormack, B. Norton, “Integration of Microstrip Patch Antenna with Polycrystalline Silicon Solar Cell,” *IEEE Transactions on Antennas and Propagation,* vol. 57, no. 12, pp. 3969-3972, 2009.

[84] S. Vaccaro, J.R. Mosig, P. de Maagt, “Two advanced solar antenna "SOLANT" designs for satellite and terrestrial communications,” *IEEE Transactions on Antennas and Propagation,* vol. 51, no. 8, pp. 2028-2034, 2003.

[85] D. Martineau, “The Assembly Guide for Making Your Own Solar Cells,” Solaronix, 2012. [Online]. Available: http://www.solaronix.com/documents/dye_solar_cells_for_real.pdf. [Accessed 21 Sept. 2015].

[86] “Microscope Slide Physical Properties,” emsdiasum.com, [Online]. Available: http://www.emsdiasum.com/microscopy/products/histology/slides.aspx. [Accessed 11 May 2015].

[87] “Material: Indium Tin Oxide (ITO),” MIT, [Online]. Available: http://www.mit.edu/~6.777/matprops/ito.htm. [Accessed 11 May 2015].

[88] “Titanium Dioxide – Titania (TiO2),” azom.com, [Online]. Available: http://www.azom.com/properties.aspx?ArticleID=1179. [Accessed 11 May 2015].

[89] V. Jovanovski, E. Stathatos, B. Orel, P. Lianos, “Dye-sensitized solar cells with electrolyte based on a trimethoxysilane-derived ionic liquid,” *Thin Solid Films,* vol. 511, pp. 634-637, 2006.

[90] GE Silicones, “GE Silicones RTV120 Series Neutral Cure Adhesive Sealant,” [Online].

Available: http://www.dcproducts.com.au/RTV_Silicone_Solutions/Tech_Data_Sheets/RTV120S-tds.pdf. [Accessed 21 Sept. 2015].

[91] W.S. Wang, T. O'Donnell, L. Ribetto, B. O'Flynn, M. Hayes, C. O'Mathuna, "Energy harvesting embedded wireless sensor system for building environment applications," *1st International Conference on Wireless Communication, Vehicular Technology, Information Theory and Aerospace & Electronic Systems Technology*, pp. 36-41, 2009.

[92] P. Broadwi, "Dyeing for a place in the sun," Education in Chemistry, Sept 2012. [Online]. Available: http://www.rsc.org/eic. [Accessed 15 May 2015].

[93] C. Doyle, "SolarPrint pioneers next wave of indoor energy harvesting," Siliconrepublic, Nov 2011. [Online]. Available: http://www.siliconrepublic.com. [Accessed 15 May 2015].

[94] Fujitsu Technology Solutions, "Fujitsu Wireless Keyboard Set LX400 Input Device," 2012. [Online]. Available: http://sp.ts.fujitsu.com/dmsp/Publications/public/ds-Wireless-Keyboard-Set-LX400.pdf. [Accessed 21 Sept. 2015].

[95] LPKF, "Laser Structuring of Conductive TCO/ITO Coatings, Application Report LPKF MicroLine UV Laser Systems," [Online]. Available: http://www.lpkf.com/_mediafiles/219-laser-structuring-of-conductive-tco-ito-coatings.pdf. [Accessed 21 Sept. 2015].

APPENDIX A. LIST OF PUBLICATIONS

Journal Publications

P1. O. O'Conchubhair, A. Narbudowicz, P. McEvoy, M. J. Ammann, "Circularly Polarized Solar Antenna for Airborne Communications Nodes" *Electronics Letters*, Vol. 51, no. 9, pp. 667 – 669, April 2015.

P2. O. O'Conchubhair, P. McEvoy, M. J. Ammann, "Integration of Antenna Array with Multicrystalline Silicon Solar Cell" *IEEE Antenna and Wireless Propagation Letters*, Vol. 14 [in press, published online (February 2015)].

P3. O. O'Conchubhair, K. Yang, P. McEvoy, M. J. Ammann, "Amorphous Silicon Solar Vivaldi Antenna" *IEEE Antenna and Wireless Propagation Letters* [Accepted].

P4. O. O'Conchubhair, P. McEvoy, M. J. Ammann, "Dye Sensitised Solar Dipole Antenna" *IEEE Transactions on Antennas and Propagation* [To be Submitted].

International Conference Publications

P5. O. O'Conchubhair, P. McEvoy, M. J. Ammann, "Integration of Inverted-F Antenna with Solar Cell Substitute" *Loughborough Antennas and Propagation Conference*, Loughborough, United Kingdom, November 2012

P6. O. O'Conchubhair, P. McEvoy, M. J. Ammann, "Integrated Antenna Currents on a Polycrystalline Silicon Solar Cell" *9th European Conference on Antennas and Propagation*, Lisbon, Portugal, April 2015

National Colloquia

P7. O. O'Conchubhair, P. McEvoy, M. J. Ammann, "Integration of Antennas and Solar Cells" *4th Annual Postgraduate Research Symposium DIT*, Dublin, Ireland, November 2013

P8. O. O'Conchubhair, P. McEvoy, M. J. Ammann, "Inverted-F Antennas Integrated on Solar Cells" *Royal Irish Academy: Colloquium on Communications and Radio Science in the 21st Century*, Dublin, Ireland, April 2014